

MAGNETIC CHARACTERIZATION OF FE/PLA 3-D PRINTED FILAMENTS
AND FE-DOPED GA₂O₃ THIN FILMS

by

Lauren Henderson, B.S.

A thesis submitted to the Graduate Council of
Texas State University in partial fulfillment
of the requirements for the degree of
Master of Science
with a Major in Physics
August 2022

Committee Members:

Ir. Wilhelmus J. Geerts, Chair

Jitendra Tate

Maggie Yihong Chen

COPYRIGHT

by

Lauren Henderson

2022

FAIR USE AND AUTHOR'S PERMISSION STATEMENT

Fair Use

This work is protected by the Copyright Laws of the United States (Public Law 94-553, section 107). Consistent with fair use as defined in the Copyright Laws, brief quotations from this material are allowed with proper acknowledgement. Use of this material for financial gain without the author's express written permission is not allowed.

Duplication Permission

As the copyright holder of this work I, Lauren Henderson, authorize duplication of this work, in whole or in part, for educational or scholarly purposes only.

ACKNOWLEDGEMENTS

First and foremost, I'd like to express my sincerest gratitude to my research advisor, Dr. Ir. Wilhelmus Geerts for his constant support, guidance, and endless knowledge. Thank you for pushing me to never stop being curious and for always believing in me, even in times when I didn't believe in myself. I'd also like to thank my thesis committee members, Dr. Tate and Dr. Chen for their knowledge and support as well as Dr. Droopad and Dr. Mia for providing the Fe-doped Ga_2O_3 thin films and providing feedback on my work. I thank my friends and family for being a constant solid support system through this journey. I also would like to thank my peers, Egla Ochoa-Madrid, James Nicholas Talbert, and Tanjina Ahmed for all their help and guidance, as well as making me feel at home at Texas State University.

I acknowledge financial support for the work on the Fe/PLA filaments from Texas State University through a research enhancement grant (Geerts, Tate, Chen) and the work on the Fe-doped Ga_2O_3 thin films through HBCI/MI grant W911NF-20-1-0298 from the DOD (Droopad, Scolfaro, Geerts). Both projects were also supported by NSF through a DMR-MRI instrumentation grant under award 1726970. Furthermore, I am grateful for Dr. Holtz, Dr. Casey Smith, Dean Koehne, and the ARSC for the plethora of knowledge and experience I gained through training and coursework, ultimately allowing this thesis to come to fruition. Lastly, I'd like to sincerely thank the entire Texas State Physics Department and Shared Research Operations group for everything I have gained during my time at Texas State University, and everything I will take with me for years to come.

Parts of this thesis were published in the following papers and conference proceedings:

Publications:

[1] Lauren Henderson, Sam Zamora, Tanjina N. Ahmed, Camila Belduque, Jitendra Tate, Maggie Yihong Chen, Wilhelmus J. Geerts, "Altering Magnetic properties of Iron Filament PLA using Magnetic Field Assisted Additive Manufacturing (MFAAM)", J. Magn. Magn. Mat. 538 (2021) 168320.

Presentations:

[1] Lauren Henderson, Tanjina N. Ahmed, Camila M. Belduque, Jitendra Tate, Maggie Chen, Wilhelmus J. Geerts, Altering Magnetic Properties of Iron Filament PLA Using Magnetic Field Assisted Additive Manufacturing, oral presentation APS March-2021 meeting, March 15-19, 2021.

[2] Lauren Henderson, Tanjina N. Ahmed, Camila M. Belduque, Jitendra Tate, Maggie Chen, Wilhelmus J. Geerts, Altering Magnetic Properties of Iron Filament PLA Using Magnetic Field Assisted Additive Manufacturing, oral presentation TSAPS Fall-2020 meeting, UT Arlington.

[3] Tanjina N. Ahmed, Lauren Henderson, Camila M. Belduque, Maggie Chen, Jitendra S. Tate, Wilhelmus J. Geerts, "Magnetic Field Assisted Additive Manufacturing (MFAAM) of magnetic polymer composite filaments", oral presentation International Polyolefins Conference, February 23-24, 2021, SPE South Texas Section.

[4] Tanjina N. Ahmed, Lauren Henderson, Camila M. Belduque, Jitendra Tate, Maggie

Chen, Wilhelmus Geerts, “Effect on the magnetic properties of MFAAM process on hard and soft magnetic 3D printed composite materials measured with a biaxial Vibrating Sample Magnetometer (VSM) and Torque Magnetometer (TM)”, International Research Conference Texas State University, San Marcos, Texas, April 6-8, 2021.

TABLE OF CONTENTS

	Page
ACKNOWLEDGEMENTS	iv
LIST OF TABLES	x
LIST OF FIGURES	xi
ABSTRACT	xv
CHAPTER	
1. INTRODUCTION	1
1.1 Motivation	1
1.2 3-D Printed Filaments	3
1.2.1 Background and Applications	3
1.2.2 Magnetic Field Assisted Additive Manufacturing	5
1.2.3 Soft Magnetic Composites and MFAAM	7
1.3 Ga ₂ O ₃ Thin Films	8
1.3.1 Background and Applications	8
1.3.2 Polymorphs of Ga ₂ O ₃	9
1.3.3 Ferromagnetic Semiconductors Using Ga ₂ O ₃	11
2. METHODS OF CHARACTERIZATION	13
2.1 MicroSense Vibrating Sample Magnetometer (VSM) & Torque Magnetometer (TM)	13
2.1.1 Theory of VSM Operation	13
2.1.2 Schematics of MicroSense VSM Head Option	15
2.1.3 Theory of TM Operation and Magnetic Anisotropy	18
2.1.4 Schematics of MicroSense Torque Magnetometer	21
2.1.5 VSM Analysis Software	24
2.2 DynaCool Physical Property Measurement System (PPMS)	27
2.2.1 Theory of PPMS VSM Operation	28
2.2.2 Schematics of PPMS	29

2.2.3	MultiVu and Writing Sequences	31
2.3	X-Ray Diffractometer (XRD)	33
2.3.1	Theory of XRD Operation	33
2.3.2	Schematics of XRD	35
2.4	Hirox Digital Microscope	37
2.4.1	Theory and Schematics of Hirox Digital Microscope	37
3.	FE-PLA 3D PRINTED FILAMENTS	39
3.1	Printing Process/Sample Preparation	39
3.1.1	Material Properties	39
3.1.2	3-D Printer Setup & Parameters	40
3.2	Experimental Procedure	42
3.3	Graphical Results & Discussion	45
3.4	Data Analysis & Discussion	56
3.5	Supporting Characterization Methods	61
3.5.1	X-Ray Diffraction	61
3.5.2	Optical Characterization	64
4.	FE-DOPED GALLIUM OXIDE THIN FILMS	68
4.1	Growth of Thin Films	68
4.1.1	Pulsed Laser Deposition (PLD)	68
4.2	Experimental Procedure	69
4.3	VSM Signal Correction	73
4.3.1	MicroSense VSM	73
4.3.2	DynaCool PPMS VSM	76
4.4	Results & Discussion	80
4.4.1	Observed Magnetic Behavior	80
4.4.2	Iron Concentration Dependence	83
4.4.3	Temperature Dependence	89
5.	CONCLUSION & SUGGESTIONS FOR FUTURE WORK	98
5.1	Fe/PLA 3-D Printed Filaments	99
5.1.1	Conclusions	99
5.1.2	Suggestions for Future Work	99
5.2	Fe-Doped Ga ₂ O ₃ Thin Films	100
5.2.1	Conclusions	100

5.2.2 Suggestions for Future Work	102
REFERENCES	103

LIST OF TABLES

Table	Page
1. List of polymorphs for Ga ₂ O ₃ and their respective structural properties	10
2. Dimensions and mass of all three samples being measured via VSM	44
3. Magnetic susceptibility and saturated magnetic moment at field angles 0° & 90°	58
4. Dimensions of zero-field and MFAAM 5 kOe samples used for XRD measurements	62
5. XRD results for 0-field and 5 kOe transverse samples measured using $\theta/2\theta$ scans	64
6. Dimensions for different concentrated Fe-doped Ga ₂ O ₃ thin films grown via PLD	71
7. Estimated RT magnetic properties for Fe-doped Ga ₂ O ₃ samples of 2%, 5%, 15%, 40% and 75%	88
8. Magnetic properties retrieved from the hysteresis curves of the 5% and 75% Fe- doped Ga ₂ O ₃ at room temperature versus low temperatures	93

LIST OF FIGURES

Figure	Page
2.1. Setup of the MicroSense EasyVSM at Texas State University	15
2.2 Diagram of the MicroSense torque magnetometer including sensors, coils, and magnets	22
2.3 Magnetization vs. field plot from MicroSense manual depicting the image effect correction employed at fields above 1.5 Tesla [54]	25
2.4 VSM hysteresis curves before background subtraction (red) and after background subtraction (black) [54]	27
2.5 Moving from top left to right bottom: Various parts required to set up the VSM option on the QuantumDesign PPMS	30
2.6 Schematic from Leng’s “Materials Characterization” displaying Bragg’s Law of Diffraction [58]	34
2.7 Setup of the goniometer inside the Rigaku SmartLab XRD at Texas State University	36
2.8 a) Specific high range MXB-2500REZ zoom lens used from Hirox-USA [60] and b) the Hirox digital microscope setup at Texas State University	38
3.1 a) Front view and b) side view images of RoVa3D 3-D printer at Texas State University	40
3.2 MFAAM sample printed on NdFeB permanent magnets on top of 3-D printer’s platform	42
3.3 Schematics of MFAAM printing method for transverse (H_{trans}) and longitudinal (H_{long}) print-fields	43

3.4 Schematic of the biaxial VSM and the placement of the sample when a) oriented horizontally and b) oriented vertically, respectively	45
3.5 Raw data hysteresis of horizontally oriented zero field sample with varying field angles	46
3.6 Raw data hysteresis of vertically oriented zero field sample with varying field angles	46
3.7 Normalized hysteresis of vertically oriented zero field sample with varying field angles	48
3.8 Normalized hysteresis of vertically oriented zero field sample at zero and 90 degrees	48
3.9 Normalized hysteresis of horizontally oriented zero field sample with varying field angles	49
3.10 Normalized hysteresis of horizontally oriented zero field sample at zero and 90 degrees	50
3.11 Hysteresis measurements for sample printed in a field perpendicular to the cylindrical axis of 5 kOe. Sample is oriented vertically	51
3.12 Comparison of hysteresis curves for the vertically oriented sample printed in a 5 kOe magnetic field at zero and 90°	51
3.13 Hysteresis measurements for sample printed in a field perpendicular to the cylindrical axis of 5 kOe. Sample is oriented horizontally	52
3.14 Comparison of hysteresis curves for the horizontally oriented sample printed in a 5 kOe magnetic field at zero and 90°	53
3.15 Hysteresis measurements for sample printed in a field parallel to the cylindrical axis of 8 kOe. Sample is oriented vertically	54

3.16 Comparison of hysteresis curves for the vertically oriented sample printed in an 8 kOe magnetic field at zero and 90°	54
3.17 Hysteresis measurements for sample printed in a field parallel to the cylindrical axis of 8 kOe. Sample is oriented horizontally	55
3.18 Comparison of hysteresis curves for the horizontally oriented sample printed in an 8 kOe magnetic field at zero and 90°	56
3.19 Schematic displaying the demagnetizing effect in different directions of a 3-D printed filament [67]	59
3.20 Images of 3-D printed Fe/PLA filaments in a) 0-field and b) 5 kOe transverse field for XRD measurements	62
3.21 XRD pattern of the zero-field Fe/PLA 3-D printed sample displaying peaks for miller indices describing BCC iron and PLA	63
3.22 XRD pattern of the 5 kOe transverse Fe/PLA 3-D printed sample displaying peaks for miller indices describing BCC iron and PLA	63
3.23 Cross sectional optical microscope image of the zero-field 3-D printed filament ...	65
3.24 Cross sectional microscope image of the 5kOe transverse field 3-D printed filament	66
3.25 Cross sectional microscope image of the 8kOe parallel field 3-D printed filament	66
4.1 Schematic displaying the setup for pulsed laser deposition from Sarangan’s “Nanofabrication” [72]	69
4.2 Dependence of magnetic signal on the vibrational frequency used for the MicroSense VSM	75

4.3 Hysteresis curves of the 75% Fe-doped Ga ₂ O ₃ sample with varying averaging times	76
4.4 Hysteresis curves of the 75% iron sample taken at RT via PPMS VSM for different rods without considering the radial position	78
4.5 Hysteresis curves of the 75% iron sample taken at RT via PPMS VSM for different rods while keeping the radial position constant	79
4.6 Magnetization vs. field curves for monoclinic β-Ga ₂ O ₃ thin films with Fe-concentrations of 2% and 75% displaying ferromagnetic behavior	81
4.7 Zoomed in magnetization vs. field curves for 2% and 75% Fe-doped Ga ₂ O ₃ displaying ferromagnetic retentivity and hysteretic behavior	83
4.8 Magnetization vs. field curves for the monoclinic Ga ₂ O ₃ structures with 2% iron and 5% iron	84
4.9 Hysteresis curves displaying the magnetic moment per unit volume vs. magnetic field for cubic spinel Ga ₂ O ₃ structures of 15%, 40%, and 75% iron	85
4.10 Saturation magnetization versus iron concentration for the Fe-doped Ga ₂ O ₃ samples measured via PPMS VSM	86
4.11 Normalized hysteresis curves of all five Fe-doped Ga ₂ O ₃ samples taken at RT via PPMS VSM	87
4.12 Magnetization vs. temperature curve for the 5% Fe-doped Ga ₂ O ₃ sample at a temperature range of 5 K to 798 K	90
4.13 Magnetization vs. temperature curve for the 75% Fe-doped Ga ₂ O ₃ sample at a temperature range of 5 K to 848 K	91
4.14 Normalized hysteresis curves of 75% Fe-doped Ga ₂ O ₃ displaying the change in magnetic behavior at room temperature compared to lower temperatures	92

ABSTRACT

The work of this thesis consisted of magnetic characterization on two different materials: soft magnetic Fe/PLA filaments 3-D printed using magnetic field assisted additive manufacturing (MFAAM) and Fe-doped Ga_2O_3 thin films grown via pulsed laser deposition (PLD) of various iron concentrations. The Fe/PLA filaments were printed on top of permanent magnets to supply different external magnetic field strengths to the filaments during the printing process, a modification referred to as magnetic field assisted additive manufacturing (MFAAM). These various filaments were then measured using a MicroSense biaxial VSM to observe magnetic field dependence as well as field angle dependence on the magnetic properties and determine any potential anisotropy. The filaments were also characterized by digital microscopy and x-ray diffraction (XRD) to further confirm the results from the VSM. These results confirmed enhanced magnetic properties through increased susceptibility and induced anisotropy of the filaments printed with MFAAM.

The magnetic properties of Fe-doped Ga_2O_3 thin films of various iron concentrations (2%, 5%, 15%, 40%, and 75%) and crystal structures (monoclinic for concentrations less than 10% and spinel cubic for samples greater than 10%) were examined. These films were measured using both the MicroSense VSM and the QuantumDesign PPMS VSM to observe their magnetic moments' dependency on magnetic field strength, temperature, and iron concentration. The samples' hysteresis curves were inspected and magnetic

properties such as saturation magnetization, coercivity, and remanence were estimated and compared. The magnetization with respect to temperature was also investigated for the 5% and 75% Fe-doped samples. The magnetization vs. temperature curves displayed different magnetic behavior for the 5% and 75% samples, suggesting a potential change in magnetic ordering as the iron concentration increased.

1: INTRODUCTION

1.1 Motivation

Magnetic materials have been incredibly prevalent in modern-day scientific research, specifically materials science research, and the list of uses and applications is growing substantially. With the ability to read and store information, generate power, and even convert energy from one form to another, magnetic materials have proven to play crucial roles in various aspects of everyday life. Recently, there has been a surge of interest in printable electronics using soft magnetic materials that are suitable for printing motors, power transformers, and actuators, all of which are made possible by additive manufacturing [1-3]. Additive manufacturing, or AM, has been around for decades and allows for a precise and personalized approach to printing an impressive variety of objects, including those with unique or complex geometries. This printing method has proven to be cost and waste efficient, as it does not require ample material or time to create the desired prototype; the use of computer-aided-design (CAD) makes it possible to only use the amount of material necessary to print the desired object rather than cutting from bulk material [4].

Additive manufacturing has been modified in recent research by exposing the printed composites to an external magnetic field during the printing process to explore the possibility of enhancing magnetic properties of such materials. Such work has been done with hard magnetic 3D printed materials, displaying an induced magnetic anisotropy as well as increasing the material's energy product and remanence, thus yielding stronger permanent magnets [5]. The inclusion of an external magnetic field during printing has been coined magnetic field assisted additive manufacturing, or MFAAM. While various

research has been conducted on hard magnetic composites printed using MFAAM, research on soft magnetic printed composites is scarce. Successful studies on soft magnetic composites using this printing method could change the game for a myriad of focuses such as 3D printable magnetic transformers suitable for energy transport and even novel generators for wind and solar power.

Another realm of materials research that is forever growing is that surrounding ultra-wide bandgap semiconductor thin films such as gallium oxide (Ga_2O_3), specifically Ga_2O_3 based alloys. Ga_2O_3 is an indirect ultrawide band gap semiconductor that is promising for applications such as power electronics, UV detectors, and potentially magnetic sensor applications. With a bandgap of almost 5eV (4.9eV), much larger than traditional wide bandgap semiconductors, this material becomes an impressive candidate for optical applications as well such as solar cell devices and UV photodetectors [6,7], and since the demand for efficient renewable energy is heavily increasing, wide bandgap semiconductors like Ga_2O_3 make advancements in research surrounding optical devices possible. Studies have shown that Ga_2O_3 is incredibly versatile, having the ability to act as both an insulator or a conductor depending on the doping conditions, and successful alterations have been done by doping Ga_2O_3 with charge carriers such as Si, Sn, Ge and even Nb to increase the carrier concentration (and therefore the conductivity) and enhance the electrical and optical properties of the material [6,8,9]. These qualities make Ga_2O_3 a viable choice for optical and environmental applications needing devices capable of withstanding high voltages and temperatures without sacrificing quality, time, or cost. While the large bandgap of Ga_2O_3 already sets it ahead of its competitors, another area of interest for this particular material could be the realization of ferromagnetic behavior

above room temperature when doped with transition metals such as Ni, Fe, and Co. Ferromagnetic semiconductors have the best of both worlds. Wide bandgap semiconductors present the benefits of functioning through large supplies of voltage/power, operating well above room temperature, and faster switching speeds. Ferromagnetic elements allow these semiconductors to become equipped with magnetic characteristics relating to high susceptibility, high permeability, and little hysteresis loss. With all these qualities working together, ferromagnetic semiconductors open the doors for future research surrounding a myriad of spintronic devices, ranging from non-volatile memory and logic devices to advances in artificial intelligence [10,11]. This combination has been studied on other magnetically doped semiconductors such as GaN and ZnO, both of which have shown ferromagnetic effects when operating at or above room temperature, but these results were difficult to reproduce with confidence [11,12,13]. This thesis intends to continue the research done by M.D. Dalim Mia [14] by further exploring the magnetic properties of Fe-doped Ga_2O_3 and conclude if this material could be effectively implemented as a ferromagnetic semiconductor in areas such as nonvolatile memory and magneto-optic devices.

1.2 3-D Printed Filaments

1.2.1 Background and Applications

3-D printing, more recently referred to as additive manufacturing (AM), has been around longer than most might assume, but has gained a lot of traction in recent years due to the price drop in equipment and materials, ease of operation and the myriad of applications it's been incorporated in to. AM is a multistep process that imports customized computer aided design (CAD) blueprints from a 3-D modeling software and prints the desired

design layer by layer at controlled parameters such as print height, speed, and temperature with ease. 3-D printing began in the 1980's in Japan with efforts first made by Hideo Kodama to find a more rapid prototyping system for manufacturing uses [15]. The assortment of printing technologies that have been developed since the first prototyping system has grown immensely, some of which include Stereolithography (SLA), Selective Laser Sintering (SLS) and Fused Deposition Modeling (FDM) [15], the latter being the method optimized in this thesis. While the advancements of the 1980's put 3-D printing on the map, the difficulty of operation and high equipment costs deterred many away from taking advantage of the possibilities these systems held. However, the next ten years would prove to be even more profound with increased public availability of CAD software and reduced equipment/material costs. By 2010, 3-D printing had made its way into the medical field with the first prosthetic leg and functional miniature kidneys being printed [15,16] and in 2011 researchers took it a step further by printing an entire aircraft which cost under \$7,000 in total [16].

Nowadays, with the improvements that have been made in 3-D printer models and printing materials (ranging from plastic to metal to even chocolate) [15,17], this futuristic process can be found in an array of fields such as construction, education, culinary and artwork [18]. More recently, materials scientists have taken advantage of this incredibly versatile process as well for functional applications to help aide in renewable energy, energy production and energy conversion. Special focus has been taken surrounding the research and development of additive manufacturing with magnetic materials, allowing for printable transformer cores, permanent magnets, and sensor applications to name a few [1,2,19,20]. Scientists have successfully relaxed the restrictions on printing complex

shapes and reducing manufacturing costs by using 3-D printing to create polymer-bonded composites involving hard magnetic NdFeB and SrFe₁₂O₁₉ filler particles to allow for electric and magnetic applications such as novel actuators and sensor devices [2, 21,22].

Furthermore, a few studies have been done on 3-D printed transformers using soft magnetic polymer composites, but the results show there is still work to be done in accomplishing a fully functional AM commercial transformer core. Bollig et al. 3-D printed and characterized different transformer core geometries and fill patterns using a magnetic thermoplastic polymer and concluded that while larger fill fractions improve the printed transformer performance, the printed transformer cores did not saturate as easily as a standard transformer core, suggesting higher concentrations of Fe particles in the PLA matrix as a solution [19]. Similar work was done by Tiismus et al. by using ferromagnetic materials to print a full E-type transformer core and they compared their findings to a traditional commercial transformer core. They reported a much lighter and thinner core for the 3-D printed prototype and achieved a high fill factor of about 89%, but the printed transformer fell short in comparison to the commercial core with a reduction in efficiency and low magnetic polarization which they attributed to lack of control in the printed material grain structure orientation [3].

1.2.2 Magnetic Field Assisted Additive Manufacturing

Additive manufacturing has proven to be an asset in printing prototypes for structural purposes like buildings and prosthetics. However, research and development surrounding functional magnetic materials via AM is still fairly new and issues regarding their competitiveness with commercial products is still widespread. However, to increase the

performance of AM products, an even more recent phenomenon is being explored which involves applying an external magnetic field during the initial stages of the printing process, referred to as magnetic field assisted additive manufacturing (MFAAM). Studies so far have shown that this field assisted method enhances the quality of printed magnetic prototypes in terms of easy magnetization and improved degree of alignment of the magnetic particles being used. Such improvements make MFAAM a contender for a printing method that yields efficient, functional products at reduced costs, labor, and waste.

Researchers at Ames Laboratory and Oak Ridge National Laboratory studied the integration of MFAAM (referred to as *in-situ* alignment in their work) by equipping an external magnetic field source to the extrusion nozzle of the 3-D printer and were able to increase the mobility of these particles by melting the polymer matrix and allow for easy rotation of the magnetic particles as the molten polymer flowed through the nozzle [24]. This process was exploited during printing composite anisotropic powders bonded in Nylon12 and recycled Sm-Co powders bonded in PLA and an increased degree of alignment of 65% and 83%, respectively, for both composites was realized [24]. Work done by de Oliveira Barros et al. also successfully demonstrated the benefit of MFAAM with hard magnetic materials by printing a mixture of $\text{SrFe}_{12}\text{O}_{19}$ particles in an uncured elastomer on top of a permanent magnet (NdFeB), removing the necessary step of magnetization of the composite after printing [25]. Instead, the magnetization was realized by applying the external magnetic field during the curing process and resulted in particle chaining and alignment to allow for a clear easy axis of magnetization and an increase in remanent magnetization of 100% to ultimately lead to the development of

small field controllable mobile robots [25]. The work done by Sarkar's and de Oliveira Barros' teams eliminate the need for post-printing magnetic alignment, thus reducing the cost and time necessary to magnetize these types of composites without sacrificing the quality of the magnetic properties they encompass.

1.2.3 Soft Magnetic Composites and MFAAM

A significant amount of research has been done on hard magnetic materials printed using MFAAM to confirm the outstanding effects this method has on not only the magnetic properties of the yielded products, but also the cost and time surrounding the production. However, these effects are scantily studied in the realm of soft magnetic materials. Kim et al. successfully incorporated MFAAM into printing 3-D structures using a viscoelastic ink to obtain programmed ferromagnetic domains and therefore allow for realization of reconfigurable soft electronic devices and soft material robots capable of crawling, rolling, and catching objects [26]. Furthermore, research involving the combination of assisted field AM and polymeric nanocomposites revealed an increase in magnetic anisotropy and allowed for the successful fabrication of complex microactuators capable of 2-D and 3-D motion [27]. Proven to pre-align the magnetic particles during printing and allow for easy magnetization, MFAAM could serve to be the missing puzzle piece in a myriad of soft magnetic devices, specifically the production of 3-D printed transformer cores, as mentioned above, to allow for easier saturated magnetization and better magnetic anisotropy within the printed filaments. This thesis intends to further investigate this possibility and determine if the benefits MFAAM has shown in the production of hard magnetic material prototypes can be transferred over to soft magnetic devices as well.

1.3 Ga₂O₃ Thin Films

1.3.1 Background and Applications

Gallium oxide (Ga₂O₃) has been studied for decades to investigate its potentiality in various areas of technology development. The rise in experimentation began with the realization of gallium oxide's ultra-wide bandgap and semiconductor properties, allowing researchers to explore the possibilities of optical and electrical applications in devices such as conductive windows for ultraviolet (UV) light [28-30]. With a bandgap of 4.9 eV, this oxide has the most commonly used semiconductors (such as SiC, GaN, and ZnO with respective bandgaps of 3.26 eV, 3.39 eV, 3.37 eV) beat by a mile [31-34]. In 1965, the United States Air Force sponsored a study surrounding the optical characteristics of Ga₂O₃ and found that the absorption edge observed at room temperature (RT) was shifted toward shorter wavelengths with an increase in photon energy when temperature was reduced to 77 K, allowing for the realization of photoconductivity [28]. With these optical properties being discovered and further confirmed, the interest in what else this material could do skyrocketed and lead to the dive into the potential for electrical applications.

Initially, Ga₂O₃ was used as an insulator for GaAs wafers due to its small intrinsic charge carriers, and with a refractive index of $n=1.84$ to 1.88 at wavelengths of 980 nm, it has also been utilized as an anti-reflective coating on GaAs as well [35,36]. These qualities allowed gallium oxide to be implemented in areas such as photodiodes and solar cells. However, researchers also discovered that this material's electrical properties could be modified through a process known as doping in order to increase the conductivity of the material and expand its usage. Doping involves the introduction of impurities (whether

they be donors or acceptors) into an intrinsic semiconductor and by varying the number of carriers in this material, allows for modification in the material's intrinsic properties [37]. These modifications can present themselves as structural, electrical, or optical changes. While p-type doping for Ga₂O₃ is scarce, numerous reports have been done showing the effectiveness and controllability of n-type doping on Ga₂O₃ such as those done with elements including Si, Sn, and Ge. These efforts displayed increased carrier concentrations ranging from 10¹⁵ cm⁻³ to 10²⁰ cm⁻³ accompanied by elevated electron mobilities of up to 120 cm²/Vs [38-40]. Wong et al. also demonstrated a breakdown voltage of over 750 V in a field-plated Ga₂O₃ MOSFET [41]. On top of this, gallium oxide has a theoretical critical electric field strength of 8MV/cm which is three times larger than that of SiC and GaN [6,30,40]. Such advancements make Ga₂O₃ instrumental in the construction of high-power electronic devices such as Schottky diodes and field effect transistors (FETs) in utilizing large bias voltages.

1.3.2 Polymorphs of Ga₂O₃

One of the biggest realizations in the practicality of gallium oxide was the recognition of the handful of structures this material can take on. Polymorphism occurs when a solid material possesses the ability to take on different crystal structures but contain the same chemical makeup. Ga₂O₃ has a reported five polymorphs: α -, β -, γ -, δ -, and ϵ -Ga₂O₃ [30] and of these five, the most heavily studied are the β - and α -phases, with most research revolving around β -Ga₂O₃. The following table gives the reported parameters for the five polymorphs being discussed:

Table 1. List of polymorphs for Ga₂O₃ and their respective structural properties

Polymorph	Crystal Structure	Space Group	Lattice Parameters (\AA , deg)	References
α -Ga ₂ O ₃	Rhombohedral	R $\bar{3}$ m	a=4.9825 \AA c=13.433 \AA	14,30,35
β -Ga ₂ O ₃	Monoclinic	C2/m	a=12.23 \AA b=3.04 \AA c=5.80 \AA β =104°	14,30,35
γ -Ga ₂ O ₃	Spinel Cubic	Fd $\bar{3}$ m	a=8.238 \AA	14,30
δ -Ga ₂ O ₃	Base Centered Cubic	Ia $\bar{3}$	a=10.0 \AA	14,30
ϵ -Ga ₂ O ₃	Orthorhombic	Pna2	a=5.120 \AA b=8.792 \AA c=9.410 \AA	30,35

While research surrounding certain phases are scarce, each phase holds unique characteristics that validate the research behind them; for example, α -Ga₂O₃ is reported to have the largest bandgap of all the polymorphs at $E_g=5.16$ eV [35]. However, the cons outweigh the pros for most of these phases as they have been found to be metastable and convert to the most stable polymorph β -Ga₂O₃ after annealing, preventing these structures from being manufactured in high bulk [30,42,43]. This thesis will be characterizing thin films involving the β - and γ -phases, so these structures will be explained in greater detail than the other polymorphs listed above.

β -Ga₂O₃ is the only stable polymorph of gallium oxide that has been studied in depth and proven to be useful in an array of applications including metal-semiconductor field-effect transistors (MESFETs), Schottky diodes, and solar blind UV detectors [40,44]. β -Ga₂O₃ is monoclinic and consists of two coordination sites for the Ga ions: tetrahedral and octahedral [14]. These crystals have a reported average electron mobility of 130 cm²/Vs

and reaches a maximum of at $500 \text{ cm}^2/\text{Vs}$ at 100 K, allowing for fast switching speeds and making it an advantageous choice for high electron mobility transistors (HEMTs) [45]. Not only does this polymorph display top of the line electrical properties, but due to its thermal stability, $\beta\text{-Ga}_2\text{O}_3$ single crystals and epitaxial films can be produced in high bulk using processes such as chemical vapor deposition (CVD) and the Czochralski method [14,45].

While the majority of research on gallium oxide involves $\beta\text{-Ga}_2\text{O}_3$, there is another phase that has been of recent interest: $\gamma\text{-Ga}_2\text{O}_3$. This polymorph takes on a defective cubic spinel crystal structure and is also equipped with tetrahedral and octahedral lattice sites [14,30]. With a large bandgap of 4.7eV, this phase has been used in optoelectronic applications including, but not limited to, solar cell improvement as well as electroluminescent devices [14,46]. However, the spinel structure that this phase has opens the door for potential magnetic applications as well, namely diluted magnetic semiconductors (DMS) and ferromagnetic semiconductors (FMS). Such advancements into the magnetic properties of $\gamma\text{-Ga}_2\text{O}_3$ could prove to be promising for furthering the development of spintronic devices such as data storage and energy harvesting.

1.3.3 Ferromagnetic Semiconductors Using Ga_2O_3

While the experimentation and construction of Ga_2O_3 -based devices are abundant in electric and optical fields, the magnetic properties of this material have not been as explicitly explored. With little research to go off of, the potential behind exploiting these magnetic properties seems far-fetched. However, with growing interest in the defective spinel polymorph, the use of gallium oxide for ferromagnetic applications is becoming

feasible. As mentioned previously, ferromagnetic semiconductors combine important properties such as wide bandgaps and high Curie temperatures (T_c) to produce devices capable of withstanding high electric fields and operating temperatures in order to take advantage of not only charge carriers, but the spin that accompanies these charges [10]. Prior research on γ - Ga_2O_3 films have shown ferromagnetic characteristics, such as that of Mn-doped γ - Ga_2O_3 films which displayed room temperature ferromagnetism [47]. Even more recently, Huang et al. showed that by doping γ - Ga_2O_3 with Fe particles, a high saturated magnetic moment was obtained at room temperature, proving to be a promising candidate in high performance DMSs [48]. This thesis intends on delving further into the magnetic properties of Fe-doped β - Ga_2O_3 and γ - Ga_2O_3 structures in hopes to confirm their stability and efficiency at various Fe concentrations and extreme temperatures to ultimately prove their functionality in novel magneto-optic device applications.

2: METHODS OF CHARACTERIZATION

2.1 MicroSense Vibrating Sample Magnetometer (VSM) and Torque Magnetometer (TM)

The first piece of equipment that will be discussed is the MicroSense EZ-9 Biaxial Vibrating Sample Magnetometer (VSM) and the Torque Magnetometer (TM) option. The VSM option was used in this research to observe the magnetic properties of the Fe/PLA 3-D printed filaments such as the saturation magnetization, hysteresis, and the magnetic anisotropy. It was also used to observe the changes in the magnetic behavior of the Fe-doped Ga₂O₃ thin films with respect to high temperatures. The MicroSense TM option was to be implemented to examine the magnetic anisotropy of the Ga₂O₃ thin films at RT with supplementing torque measurements performed using the biaxial VSM at varying temperatures.

2.1.1. Theory of VSM Operation

A vibrating sample magnetometer (VSM) is used to measure the magnetic properties of soft magnetic and hard magnetic materials at high and low magnetic fields, as well as a wide range of temperatures. This technique can uncover a lot about a sample's magnetic behavior, including magnetic anisotropy, susceptibility, remanence, and coercivity of the material. VSMs measure a sample's magnetic moment by vibrating the entire sample in a uniform applied magnetic field, therefore magnetizing the sample, and generating a time dependent magnetic "stray" field. The sample's time dependent stray field induces a voltage in the detection coils surrounding the sample, which can be described using Faraday's Law of Induction, given below [49]:

$$\varepsilon = -N \frac{d\phi}{dt} \quad 2.1$$

Where “ ε ” is the induced voltage (or emf), “ N ” is the number of turns in the coils, “ ϕ ” is the magnetic flux, and “ t ” is time. So, the amount of voltage induced in the pickup coils is proportional to the changing coupled magnetic flux through the coils over time and therefore proportional to the magnetic moment of the sample. However, even though the applied magnetic field itself is not changing, the sample’s magnetic flux through the detection coils is changing and is therefore time dependent. Keeping this in mind, the magnetic flux can be described in terms of the surface area in which the flux passes through and the magnetic flux density [49]:

$$\phi = BA \cos \theta \quad 2.2$$

where “ B ” is the magnetic flux density, “ A ” is the surface area perpendicular to the magnetic field, and “ θ ” is the angle between the direction of the sample’s magnetic stray field and the normal of the detection coils’ surface area. The sample is mounted in the VSM so that it’s normal is parallel with direction of the magnetic field, so the cosine term disappears. Substituting this definition of magnetic flux into Faraday’s law yields [49]:

$$\varepsilon = -N \frac{d(BA)}{dt} = -NA \frac{dB}{dt} \quad 2.3$$

The change in flux density changes with respect to time as well as the z-direction, so implementing the chain rule, equation 2.3 can be rewritten as:

$$\varepsilon = -NA \frac{dB}{dz} \frac{dz}{dt} \quad 2.4$$

Note that the sample’s stray field is similar to the field caused by a magnetic dipole point and therefore varies with $1/r^3$, where “ r ” is the distance from the dipole point. Therefore,

for the case of a VSM, the change in the sample's position with respect to the detection coils placed around the sample creates a changing magnetic flux over time that in turn generates an induced voltage in those pickup coils.

2.1.2 Schematics of MicroSense VSM Head Option

The components of the MicroSense EZ-9 VSM pertaining to this thesis are comprised of the VSM motor/vibrator head, electromagnet, stationary pick-up coils, the chiller and a control rack consisting of the lock-in amplifiers, gaussmeter, and the magnet power supply. For the temperature dependent measurements, the oven and temperature controller will be used in addition to the components listed above. Also included is the torque magnetometer head. The images below highlight the parts that will be utilized in this thesis:

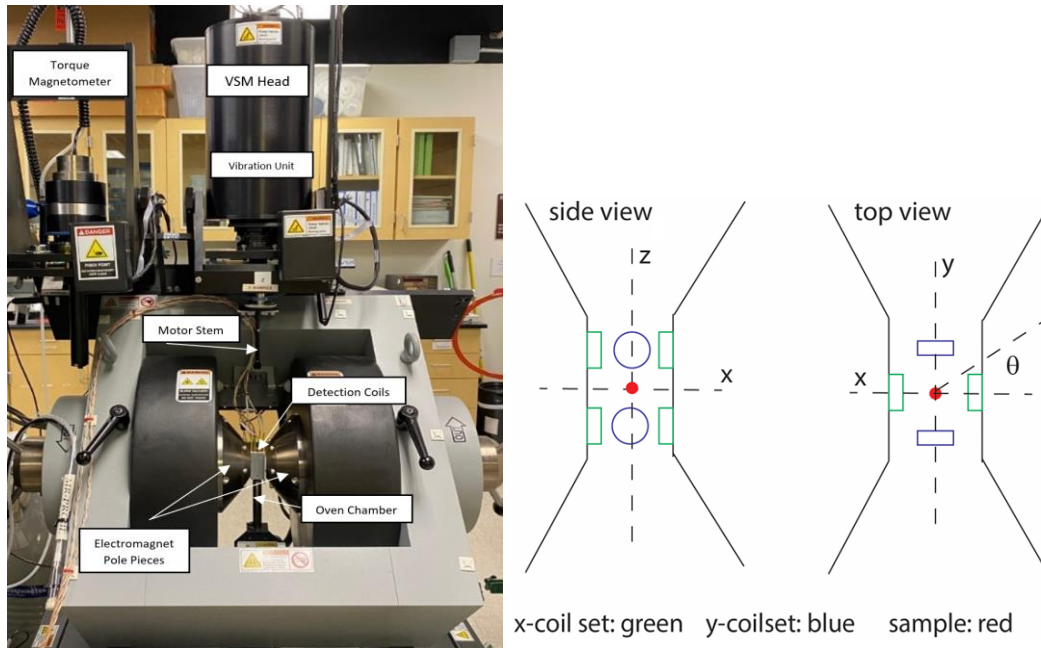


Figure 2.1. a) Setup of the MicroSense EasyVSM at Texas State University. Also shown is the torque magnetometer. b) Configuration of biaxial coil set used to measure the components of the magnetic dipole vector parallel and perpendicular to the applied field; the red dot represents the sample.

The MicroSense VSM allows for a magnetic field range of -2.4 Tesla to 2.4 Tesla, a full 360° field angle range, and a temperature range of 77K to 1,000K [50]. The samples being measured can be mounted on a variety of rod holders, such as pyrex or quartz rods, both of which have perpendicular and transverse holder options. Adhesives such as museum wax, superglue or ceramic cement can be used to attach the samples to the rod holder of choice depending on the desired temperature. For the 3-D printed filament samples, the 8mm perpendicular quartz rod holder was utilized and for the Ga₂O₃ thin films, the 5mm transverse rod holder was used. Once the samples are mounted to the desired rod holder, the sample/holder mechanism is attached to a motor/vibrator stem (seen above in figure 2.1) that is connected to the VSM head. This motor stem vibrates the sample in the z-direction at a fixed frequency and amplitude while an electromagnet applies a uniform magnetic field through two pole pieces, directly magnetizing the vibrating sample. This sample sits secured in a “chamber” consisting of eight vector coils, four measuring the magnetic moment parallel to the external magnetic field (deemed the x-direction or M_x signal) and four measuring the moment perpendicular to the external field (deemed the y-direction or M_y signal). The sample begins to experience a changing magnetic flux, inducing a voltage that is picked up by these surrounding vector coils. The coils are connected to lock-in amplifiers, which act as narrow bandpass amplifiers and allow for a high signal-to-noise ratio by enhancing the sensitivity. The amplifiers use this signal to obtain a magnetic moment value that is read by the user through a data analysis software. This process can be employed for a range of magnetic field values in either a step mode measurement option or sweep mode measurement option, both of which are explained in detail below. For this thesis, samples were

subjected to sweep mode hysteresis scans for a magnetic field range of -2.2 Tesla (-22,000 Oe) to 2.2 Tesla (22,000 Oe).

The 3-D printed filaments were measured not only as a function of magnetic field strength, but also as a function of magnetic field angle to observe any magnetic anisotropy present due to the shape and size of each sample. The VSM allows for hysteresis measurements as a function of different parameters, such as varying the angle at which the magnetic field hits the sample. This option takes an indirect approach in measuring the anisotropy by monitoring the change in the amount of signal that is induced when rotating the sample's easy axis away/toward the direction of the field lines of the electromagnet. To explore the dependence on field angle, the 3-D printed samples were rotated about the z-axis from 0 to 90° in 15° increments, running a full magnetic field sweep hysteresis scan at each angle. This method was carried out for all three 3-D printed filaments, both in "horizontal" and "vertical" orientations (seen in Chapter 3) while using the 8mm perpendicular quartz rod holder.

Extreme temperatures, hot or cold, can heavily alter a magnetic material's properties, especially at turning point temperatures such as Curie and Néel temperatures where the type of magnetic ordering changes completely. The Ga₂O₃ thin films were measured as a function of temperature to observe any possible magnetic alterations, so the temperature control option of the MicroSense VSM was implemented during the thin film hysteresis measurements. The overall method for temperature dependent hysteresis scans remains the same as a normal hysteresis measurement, but the parameters vary slightly, as now the samples are being exposed to different temperatures during measurement. The samples were to be measured using a sweeping magnetic field from -2.2 Tesla to 2.2

Tesla for temperatures ranging from 298 K to 848 K in 100 K and 50 K increments. The Ga₂O₃ samples were mounted on a quartz 5mm transverse rod holder using a ceramic adhesive; since the samples were exposed to high temperatures, the museum wax could not be used as the adhesive for these measurements. The samples were mounted in the VSM head and secured in the chamber as described above, only now with the oven chamber raised and enclosing the sample. To increase the temperature within the oven above room temperature, a supply of Argon gas was employed. This gas is continuously fed through a line leading into the oven chamber and the amount and type of gas supplied depends on the desired temperature.

2.1.3 Theory of TM Operation and Magnetic Anisotropy

When a material is subjected to an external applied magnetic field, that material experiences a force known as torque, that tries to pull the material's magnetization towards the applied field direction. A torque magnetometer (TM) directly measures the macroscopic torque exerted on a sample by an applied field. The torque per unit volume of the sample that the applied magnetic field exerts on the magnetization is described by the following equation [51]:

$$\vec{\tau}_H = \mu_0 \vec{M}_s \times \vec{H} \quad 2.5$$

Where “M_s” is the saturation magnetization of the sample and “H” is the applied magnetic field. Due to the cross product of the saturation magnetization and applied magnetic field, the only components that will be contributing to the torque will be those where M_s is perpendicular to the applied magnetic field. Therefore, the torque exerted on the magnetization can be rewritten as:

$$\vec{\tau}_H = \mu_o M_y H_x \hat{k} - \mu_o M_z H_x \hat{j} = \mu_o M_{\perp} H \quad 2.6$$

Assuming the magnetization in the z-direction $M_z=0$ and the magnetization in the y-direction $M_y=M_{\perp}$, equation 2.6 can be simplified to $\tau_H = \mu_o M_{\perp} H$. However, the applied field must work against the anisotropic force of the sample's crystal structure that tries to pull the magnetization toward the sample's preferred direction of magnetization, deemed the easy axis. Therefore, a force is also exerted on the saturation magnetization by the crystal. To start, consider a uniaxial crystal like those of hexagonal structures where the easy axis is parallel to the c-axis. The crystal anisotropy energy is then defined as [52]:

$$E = K_o + K_1 \sin^2 \theta + K_2 \sin^4 \theta \quad 2.7$$

Where “ K_o ,” “ K_1 ,” and “ K_2 ” are known as the magnetic anisotropy constants and “ θ ” is the angle between the easy axis (c-axis) and the saturation magnetization. Neglecting the first and third terms (K_o is constant and independent of the angle and assume $K_2 \ll K_1$ and is therefore negligible), the torque acting on the magnetization by the crystal can then be written as the following derivative:

$$\tau_K = -\frac{dE}{d\theta} = -K_1 \sin 2\theta \quad 2.8$$

The TM detects the anisotropic torque through an installed sensing circuit (which will be discussed in further detail in section 2.1.4) which supplies a current through a compensation coil and tries to balance out this torque. Therefore, the value that the torque magnetometer measures is the amount of torque needed from the applied magnetic field to balance the anisotropic force being exerted on the magnetization by the sample's own crystal structure, i.e. [52]:

$$\tau_{measured} = \mu_o M_{\perp} H = K_1 \sin 2\theta \quad 2.9$$

This measured torque can be utilized to determine a sample's anisotropy constants. Denoted by “ K_1 , K_2 , etc.,” these constants describe the strength of the anisotropy in a crystal and can reveal a material's preferred direction and magnitude of magnetization. The TM measures the torque at different field angles “ θ ” and fits this torque vs. field angle plot to a Fourier series from which the MicroSense software yields anisotropy constants describing the magnitude and direction of the anisotropic force.

The anisotropy constants can also be determined using the MicroSense VSM head by exploiting the perpendicular component of the magnetization via vector coils. Recalling equation 2.9:

$$\tau_{measured} = \mu_o M_{\perp} H = K_1 \sin 2\theta$$

Where “ M_{\perp} ” is the perpendicular component of the magnetization that can be obtained indirectly from the biaxial VSM pickup coils situated in the y-direction, assuming that $M_z=0$. When these forces are balanced, the system is said to be in equilibrium and therefore the total energy of the system is at a minimum, so the following holds true [51]:

$$\mu_o M_{\perp} H = K_1 \sin 2\theta = 0 \tag{2.10}$$

When “ M_{\perp} ” is at its maximum value, $\sin(2\theta) = 1$, and equation 2.9 can then be solved for “ K_1 ,” yielding an expression for the first order anisotropy constant in terms of the maximum perpendicular magnetization and the applied magnetic field [51]:

$$K_1 = \mu_o M_{\perp max} H \tag{2.11}$$

However, the samples measured in this thesis have a cubic crystal structure, therefore having biaxial crystal anisotropy rather than uniaxial since there are two easy axis

directions in the plane of measurement. Considering this, the anisotropic energy expressed in equation 2.7 can be modified for a cubic crystal [52]:

$$E = K_o + \frac{K_1}{4} \sin^2 2\theta \quad 2.12$$

Taking the derivative of this with respect to angle “ θ ” yields the following expression for the torque exerted on the magnetization of a cubic crystal with <100> easy axis directions [52]:

$$\tau_K = -\frac{K_1}{2} \sin 4\theta \quad 2.13$$

2.1.4 Schematics of MicroSense Torque Magnetometer

While the MicroSense VSM head allows for an indirect method of measuring torque using the perpendicular component of the magnetization picked up by the vector coils, MicroSense also offers the option to employ a torque magnetometer. The TM uses a direct method in measuring the torque felt on a sample to determine the anisotropic direction in magnetic materials. The following diagram displays the inner workings of the MicroSense torque magnetometer head:

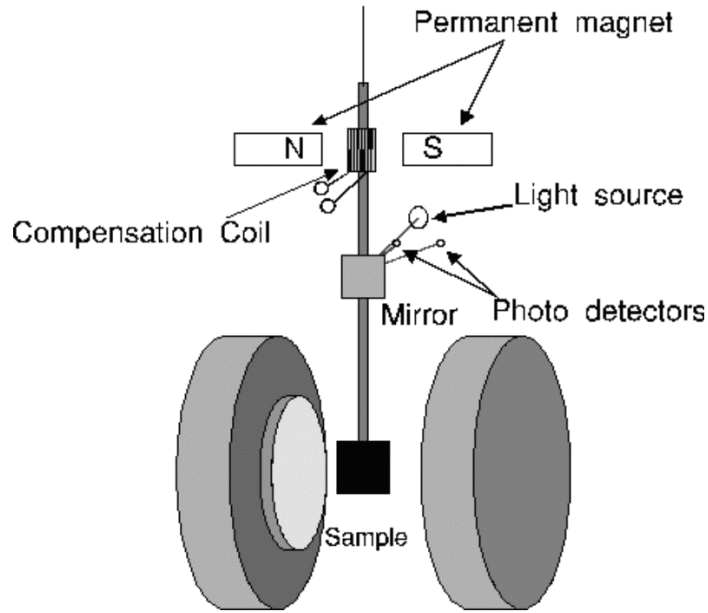


Figure 2.2. Diagram of the MicroSense torque magnetometer including sensors, coils, and magnets [50].

The MicroSense TM is equipped with automatic recording of torque curves using active sensing. Within the torque head is a near frictionless air bearing in which the sample hangs from. Also attached to this rod are the compensation coils situated between a permanent magnet and a mirror which reflects a specific amount of light picked up by the photodiodes. The sample is centered between an electromagnetic which supplies the external magnetic field. Once this field is applied, the sample is free to rotate, and as mentioned in section 2.1.3, the field works against the intrinsic force that tries to pull the sample back to its easy axis. As the sample rotates, the light source, mirror, and photodiodes within the torque head provide a feedback signal based off the amount of light that is reflected off the mirror and sensed by the photodiodes. Depending on the amount of light detected, a specific amount of current is then run through the coils within the torque head to supply a balancing torque. The amount of current running through the coils is directly proportional to the torque being exerted on the sample. This process is repeated for angles -180° to 180° to create a torque vs. field angle plot using the

MicroSense software in which the anisotropy constants and easy and hard directions can be derived from.

There are pros and cons of both methods; using the VSM option allows the torque to be measured as a function of temperature as well, which is not possible with the torque head due to the sensitivity of the measurement process. The torque head makes use of an ultra-low friction air bearing to suspend the samples, and the gas flow from the cryostat necessary for temperature-dependent measurements disturbs this process by introducing noise into the data being collected, so the biaxial VSM method is more reliable when temperature-dependent torque measurements are desired.

However, the biaxial VSM method completely relies on the signal being picked up by the vector coils which causes issues regarding calibration of the sample, as well as the quality of data taken. Since no magnetic field can be applied in the perpendicular direction, the calibration in this direction is always an indirect approach and affects the sensitivity of the signal in the pick-up coils, especially for asymmetric samples as measurements in this case are now angular-dependent [53]. As the sample approaches saturation, the signal becomes less reliable because at this point, the sample's magnetic moment is almost completely lined up with the magnetic field and the perpendicular signal from the coils in the y-direction becomes very small, making the torque difficult to measure at high fields. Therefore, the quality of the signal is dependent on the calibration of the coils and the collected data can only be as credible as calibration allows, making the TM the ideal choice for accurate torque measurements.

2.1.5 VSM Analysis Software

After the data is collected, MicroSense employs the data analysis software to enhance and correct the measured data using a myriad of data manipulation files. The voltage measured by the sensor coils can be attributed to more than just the signal coming from the sample, so the data analysis software allows for correction and elimination of these outside sources to isolate the signal coming from the sample and allow for higher accuracy in the measured data. The manipulation files that will be used on the samples for this thesis are the image effect correction, remove sweep field lag correction, and in addition to these, the background subtraction file was employed for the gallium oxide measurements. These manipulation files are explained in detail below.

Image Effect Correction

The first correction used on the VSM data compensates for the extra signal that is acquired due to what is called the “image effect.” When a sample becomes magnetized, the sensor coils pick up the magnetic flux coming from the magnetic charges on the sample. However, the magnetic stray field from the charges on the sample affects the magnetization of the electromagnet pole pieces (made of soft magnetic iron) and induces image magnetic dipole charges on these pole pieces. Therefore, the coils also pick up the flux from the image charges and results in a higher sensitivity for low magnetic field values. This is known as the “image effect.” This effect occurs when a sample is placed near a material that has a higher permeability than air, and as the sample is magnetized, it induces equal and opposite “image” charges on the surface of the highly permeable material as described above. The flux from the image charges is picked up by the sensor

coils and adds to the total signal being read. At higher field values, specifically above 1.5 Tesla, the pole pieces saturate and the flux contribution from the image charges disappears, distorting the saturation level of the sample being measured. This phenomenon can be seen in figure 2.3.

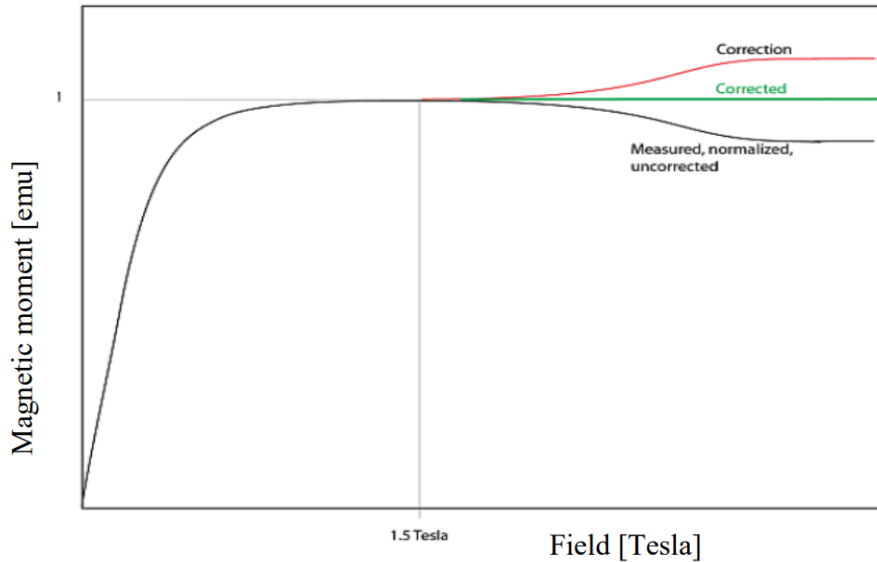


Figure 2.3. Magnetization vs. field plot from MicroSense manual depicting the image effect correction employed at fields above 1.5 Tesla [54].

To compensate for this drop in signal, the image effect correction measures a calibration sample with a known saturation magnetization as a function of the applied field above 1.5 Tesla. The signal is then normalized, and its inverse is applied to correct for the sample’s actual saturation level for fields above 1.5 Tesla [54]:

$$M_{Corrected} = \frac{1}{\frac{M(H)}{M(1.5Tesla)}} \quad 2.14$$

Sweep Field Lag Correction

When the VSM takes measurements, there are two modes applicable for data collection: step field mode and sweep field mode. Step field mode allows for a “stop and go” approach when taking data points, as it allows the system to pause at each specified

magnetic field value for some time interval to allow the electronics of the system to catch up with the changed magnetic signal, collect the measurement, and then move on to the next point by changing the field value. Sweep field mode takes a more gradual approach when running measurements by continuously running through the set of desired points and collecting data without allowing time between magnetic field changes and actual data collection. Sweep field mode is incredibly time efficient, as this mode allows hysteresis curves to be measured within minutes, whereas step mode measurements can take much longer. However, due to the electronic time constant of the lock-in amplifier, the signal being read in by the amplifier falls behind the actual signal being detected by the pickup coils during sweep field mode as the system is not allotted enough time to catch up to the true signal. Remove sweep field lag corrects for this fallback by using the sweep rate that was used during measurement and the time constant of the amplifier to shift the measured curve back over the calculated curve. Since sweep field mode was used in measuring the samples in this thesis, the “remove sweep field lag” correction was implemented on all data to accommodate for this lag in signal.

Background Subtraction

For thin film samples being measured via VSM, the signal that the coils pick up is a combination of different magnetic signals coming from the sample and the sample’s substrate. While the signal of some sample substrates need not be subtracted, those having significant diamagnetic and paramagnetic signals should be. The sample holders are made of either pyrex or quartz materials, both of which have a diamagnetic background signal and therefore also contribute to the signal being detected. Diamagnetic

signals are characterized by a straight line through the origin having a negative slope, as can be seen in the following image:

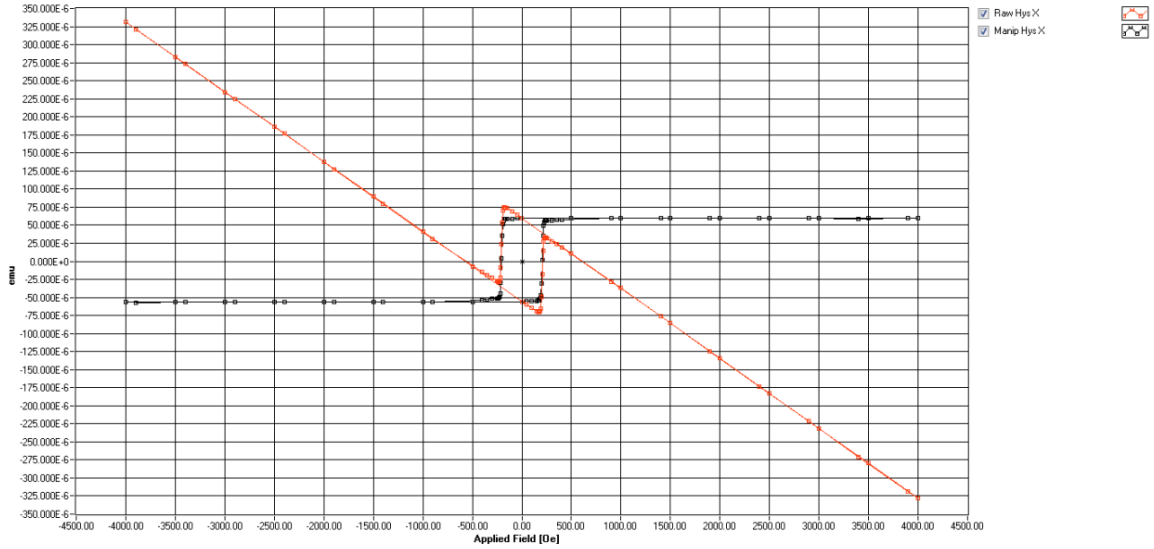


Figure 2.4. VSM hysteresis curves before background subtraction (red) and after background subtraction (black) [54].

To correct for this, the system simply subtracts a straight line as a function of the field from the measured values. Keeping in mind that for some cases the straight line might have a small offset, the expression for the corrected values can be seen below [54]:

$$M_{corrected\ x,y}(H) = M_{measured\ x,y}(H) - Offset - Slope(H) \quad 2.15$$

The gallium oxide thin films were grown on a sapphire (Al_2O_3) substrate which has a diamagnetic signal, so the background subtraction of the substrate and sample holder was employed on these hysteresis curves.

2.2 DynaCool Physical Property Measurement System (PPMS)

The next piece of equipment is the DynaCool Physical Property Measurement System (PPMS). The PPMS has a myriad of functions that can measure a sample's magnetic and electric properties by varying parameters such as temperature and applied magnetic field.

In this research, the magnetic properties of the Ga₂O₃ thin films were explored using the VSM insert of the PPMS with respect to temperature and magnetic field.

2.2.1 Theory of PPMS Operation

The DynaCool PPMS VSM insert uses a similar concept as the MicroSense VSM to acquire such measurements by Faraday's law of induction, but instead of using an electromagnet to magnetize the sample, this system uses a superconducting solenoid magnet with a current supply running through it to produce a vertical uniform magnetic field within the chamber. Ampere's Law can be implemented to describe the magnetic field being produced by the solenoid and Faraday's Law can be used again to describe the induced voltage obtained from vibrating the sample within this magnetic field. Starting with the integral form of Ampere's Law describing a magnetic field around a closed path or loop [55]:

$$\oint H \cdot dl = \mu_0 I \quad 2.16$$

Where "H" is the magnetic field, "dl" is the infinitesimal line segment of which the integral is being evaluated, "I" is the current and " μ_0 " the permeability of free space. For the situation of a solenoid, the closed loop can be evaluated the same way, but only now considering "N" number of turns within the loop. Therefore, by multiplying the total current by the number of turns per unit length, the following equation arises to describe the magnetic field strength inside a solenoid [55]:

$$HL = \mu_0 IN \quad \rightarrow \quad H = \mu_0 nI \quad 2.17$$

Where again “ I ” is the current flowing through the coils, “ μ_0 ” is the permeability of free space, and “ $n = \frac{N}{L}$ ” is the number of turns within the solenoid per unit length, referred to as the “turn density.” So, the magnitude of the magnetic field being used in this system relies on the amount of supplied current running through a set number “ N ” of turns within the solenoid, as there are no pole caps being used in this case. The PPMS acquires the magnetic moment in the same manner as the MicroSense system by vibrating the sample inside the chamber within the uniform magnetic field. So, the system is measuring the flux change brought on by the change in the sample’s position, inducing a signal in the surrounding pickup coils.

2.2.2 Schematics of PPMS

The components of the PPMS that was utilized in this research all stem from the VSM insert of the PPMS. This setup involves the installation of the VSM coilset, the sample needing to be measured mounted on the desired sample rod and rod holder, the VSM sample tube and the linear motor, which can all be seen below:

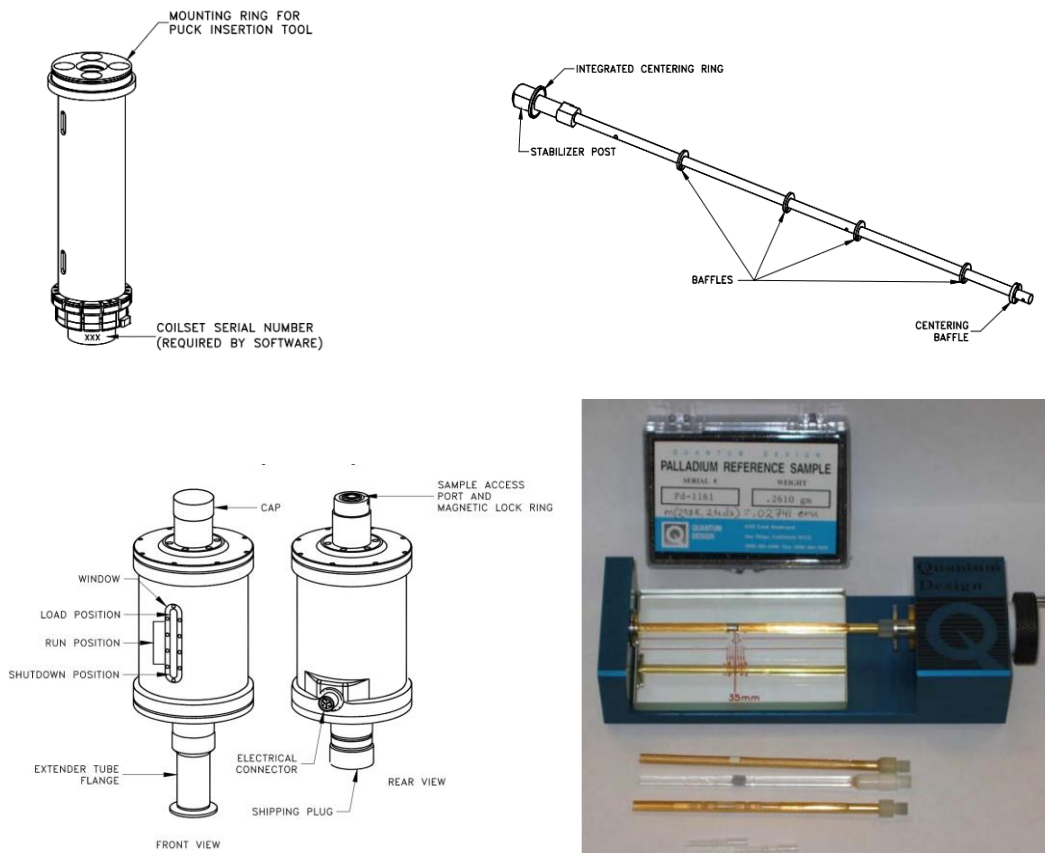


Figure 2.5. Moving from top left to right bottom: Various parts required to set up the VSM option on the QuantumDesign PPMS. Shown is the a) VSM coilset puck, b) the VSM sample tube in which the sample/rod will be placed in to center it within the chamber, c) the linear transport motor responsible for moving the sample to specified positions (load, run, shutdown), and d) the sample mounting station used to mount samples on the various rod holders; shown are the brass half tubes and quartz paddle [56].

This device implements a superconducting magnet and has a magnetic field range of -9T to 9T and a temperature range of 1.9K to 400K [57]. The setup of the VSM option begins with venting and sealing the entire chamber by running it through a helium venting cycle while the system is at room temperature and zero magnetic field. From here, the chamber is opened, the baffles are removed, and the VSM coilset (figure 2.5a) is installed into the bottom of the chamber using a puck-insertion tool. Once the coilset has been inserted, the VSM sample tube (figure 2.5b) is placed in the chamber in replacement of the chamber baffles. The linear motor (figure 2.5c) is then installed on top of the sample tube and clamped into place. Once all the equipment has been installed, the motor module and

VSM module cables are connected to allow activation of the VSM option through the MultiVu program. When the VSM option is activated and “Install/Remove sample” is selected, the system will open the chamber so a new sample may then be inserted through the top of the linear motor. The sample rod in which the sample/sample holder has been screwed on to will come to rest in the chamber and held in place by a magnetic clamp at the end of the rod that attaches to the top of the linear motor. Examples of variously mounted samples as well as the sample mounting station can be seen in figure 2.5d above.

The samples may not exceed a four-millimeter diameter to prevent rubbing and potentially damaging the coilset [56, 57]. The thin film samples measured in this thesis were mounted on a 4mm quartz paddle using rubber cement for the adhesive. The sample was manually centered using the sample mounting station seen in figure 2.5d, and then magnetically centered once inserted into the chamber. Magnetic centering requires the determination of a “sample offset,” in which the MultiVu system will attempt to find the center of the sample magnetically to determine how far away the center of the sample is from the bottom of the sample holder. Once the sample offset is determined, the chamber is closed and sealed, and the measurement building can begin.

2.2.3 MultiVu and Writing Sequences

From here begins the sequence building of the desired measurements to take place. Once the sample has been inserted into the PPMS, a data file with a description of the sample will be created using the MultiVu software program. For simple measurements, such as a single data point or continuous measuring at a specified parameter, the system allows

operation through a “VSM” measurement window, which makes it possible to change parameters such as magnetic field and temperature as the system is running the measurement.

However, in order to run a sample through various measurements and create multiple data files in one run, MultiVu has a sequence builder option that will be implemented in this research. The sequence builder mimics a simple coding language that tells the system to perform certain commands or types of measurements in a specific order to allow for multiple measurements to occur consecutively without having to manually run each individual measurement. The option to build a sequence and run multiple measurements on the same sample was applied in this thesis to measure multiple hysteresis curves of the same sample at different temperatures. The commands that were used to build the desired sequences are as follows:

- Set Temperature
- Set Field
- Wait
- New Data File
- Moment vs. Field
- Moment vs. Temperature
- Standby

Where the “moment vs. field” and “moment vs. temperature” commands allow for customization of the desired parameters for each measurement such as scan rate, value range, etc. Once the desired measurements have been taken and all data has been collected, the sample is unloaded and the process of installing the VSM option is carried out again but in reverse order to ensure proper shut down of the PPMS.

2.3 X-Ray Diffractometer (XRD)

The Rigaku SmartLab x-ray diffractometer (XRD) was used in this thesis to investigate the texture of the Fe/PLA 3-D printed filaments. X-ray diffractometry is a useful technique that can identify crystalline phases and orientation, determine sample thickness, and explore a sample's structural properties. The XRD is used to measure a wide variety of samples, from powders to thin films to polycrystalline materials such as the MFAAM filaments. The XRD employs various scan techniques, but for this thesis the $\theta/2\theta$ scan option was used to compare the relative intensity peaks of the samples 3-D printed in zero field and 5 kOe transverse field.

2.3.1 Theory of XRD Operation

X-ray diffraction measurement methods are based off constructive wave interferences of x-rays interacting with planes of atoms in crystalline materials. Given an x-ray beam incident on a crystalline solid, the x-rays scattered on consecutive planes of atoms each with a wavelength of " λ " are said to be "in phase" if their phase difference equals a multiple of " $n\lambda$," yielding constructive interference that is detected during measurement. An XRD operates by supplying incident waves that strike the surface of a material at some angle " θ ." A depiction of this is seen in the figure below:

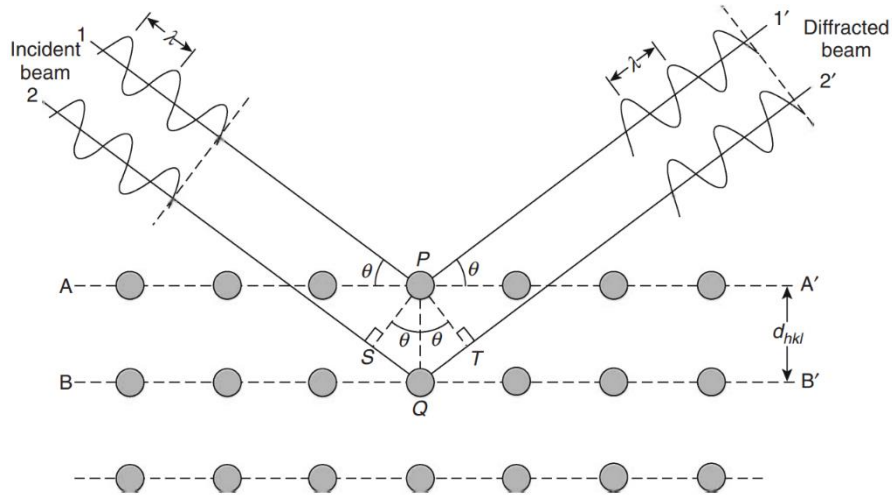


Figure 2.6. Schematic from Leng's "Materials Characterization" displaying Bragg's Law of Diffraction [58].

The wave scattered off the top atomic plane at angle θ interferes with the wave scattered off the second atomic plane a distance "d" away from the first plane, as can be seen in figure 2.6. The waves scattered from both planes are only in phase with each other if the path length difference $2SQ$ is equal to an integral multiple of the wavelength. As mentioned before, these waves must have a phase difference of " $n\lambda$ " to be in phase with each other, so the extra distance that this second wave travels before striking a crystal in another plane can be described as the sum of lengths SQ and QT which equates to the phase difference $n\lambda$. Therefore, the condition that must be satisfied for constructive interference can be described by:

$$n\lambda = 2SQ \quad 2.18$$

Using triangle "PSQ" from figure 2.6, length $PQ = d$ is the hypotenuse and since length SQ is opposite of angle " θ ," the value of length SQ can be described as:

$$SQ = d \sin \theta \quad 2.19$$

Substituting equation 2.19 into equation 2.18 yields the distance this second wavelength travels when in phase with the first angle, known as Bragg's Law of Diffraction [58]:

$$n\lambda = 2d \sin \theta$$

Bragg's law depicts the necessary conditions for constructive interference to occur for a given material and is the basis of XRD measurements. This expression is exploited through XRD by measuring a sample at various values of " θ " to determine at which angles constructive interference occurs, thus outputting correlating intensity peaks at these angles. Bragg's law can be used to determine information on a given material such as atomic spacing between crystal planes and materials' compositions.

2.3.2 Schematics of XRD

The Rigaku SmartLab XRD was used to run $\theta/2\theta$ measurements to explore the texture of samples 3-D printed with and without an applied magnetic field. The XRD goniometer is made up of five basic components: an x-ray tube, slits in which the x-ray beams pass through (two sets of slits: incident slits and receiving slits), a sample stage, a monochromator, and a detector. The various parts of the goniometer are displayed in the image below:

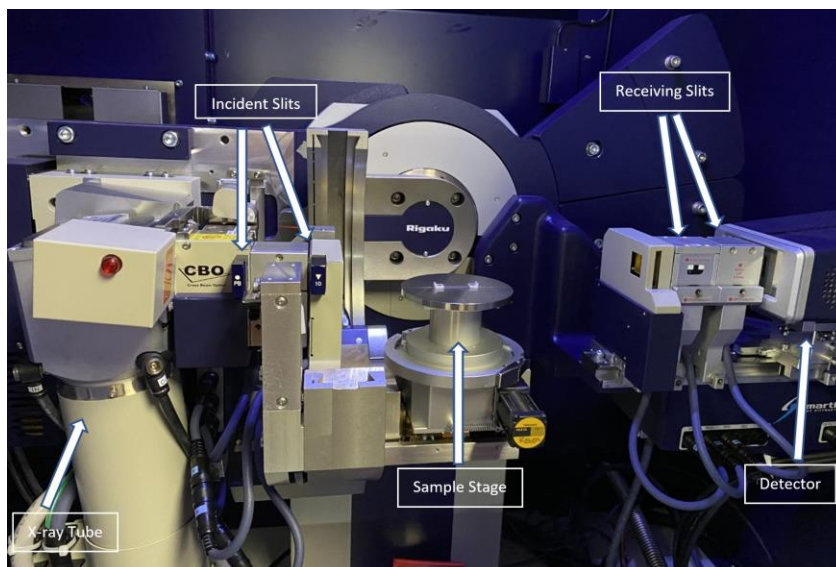


Figure 2.7. Setup of the goniometer inside the Rigaku SmartLab XRD at Texas State University.

Inside the goniometer, the x-ray beam and detector are attached to arms that allow rotation about the sample at angles θ and 2θ , respectively. Also included in figure 2.7 are soller slits located on both the incident and receiving ends of the setup. These slits help the resolution of the scans by preventing out-of-plane divergence of the incident and diffracted x-rays.

The measurements were carried out using an x-ray tube voltage and amperage of 40 kV and 44 mA, respectively. The system undergoes two processes of alignment before measurement: optics alignment and sample alignment. The system first performs an optics alignment by aligning the internal components on the incident side, moving down the x-ray beam path. Then a sample alignment is conducted in which the system attempts to align the sample parallel to the beam path through multiple iterations to ensure correct rotations through omega. Once the initial setup is complete, the type of measurement is chosen, which in this case was a $\theta/2\theta$ scan, that keeps the angle of the x-ray tube and the

detector the same throughout the scan. These measurements used parallel beam (PB) geometry to reduce signal error and lower the noise in the scans.

2.4 Hirox Digital Microscope

The Hirox digital microscope was used to further investigate the MFAAM filaments through cross sectional 3-D imaging. Digital microscopy is simply light microscopy except in lieu of an eyepiece, the system uses a camera that digitally acquires the image and displays it on a monitor. Digital microscopy extends beyond image capture, as it holds capabilities for dimension measurements, roughness measurements and 3-D modeling. Hirox microscopes also take advantage of complementary metal oxide semiconductor (CMOS) sensors to allow for high light sensitivity, low image noise and high-resolution images [59].

2.4.1 Theory and Schematics of Hirox Digital Microscope

Digital microscopy employs the standard theory of light microscopy except for the image being magnified on a monitor rather than being magnified through an eyepiece. Besides the eyepiece, the digital microscope is equipped with the basic components of an illumination system, objective lenses, the sample stage and photomicrographic system. For this thesis, the MXB-2500REZ lens was used which supplies a light source with coaxial illumination as well as dark field illumination [59]. Coaxial illumination is a reflected light source technique in which the illuminating rays are reflected by a semitransparent reflector to illuminate the sample through an objective lens [58]. Dark field imaging on the other hand is used to obtain images with higher contrast by illuminating the object being observed with oblique light rays, allowing for only scattered

light to enter the lens [58]. The setup of the Hirox microscope at Texas State University as well as the specific high range lens that was used can be seen below:

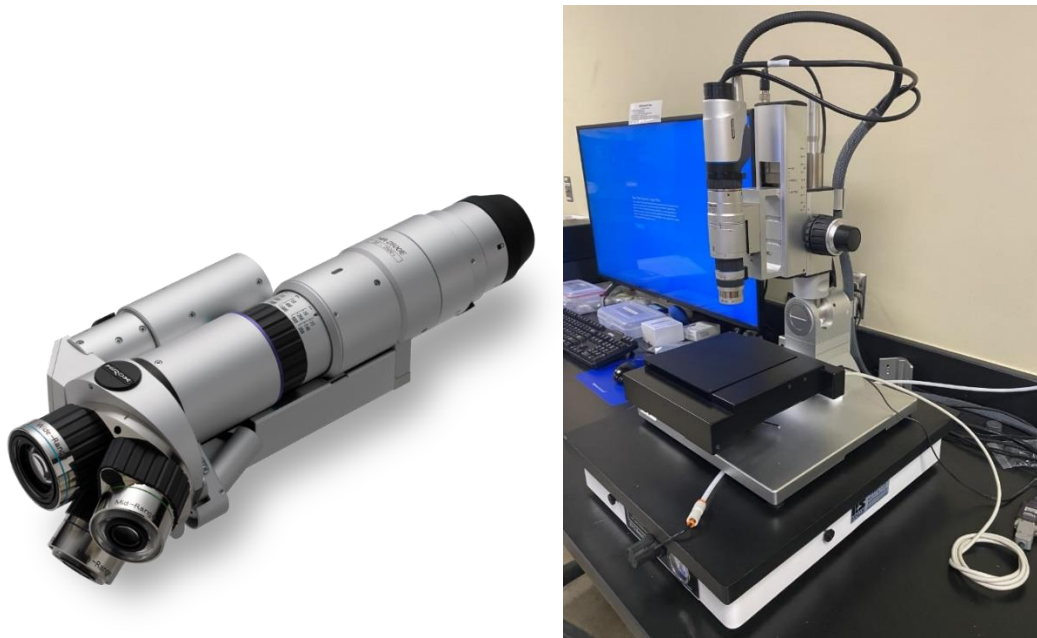


Figure 2.8. a) Specific high range MXB-2500REZ zoom lens used from Hirox-USA [60] and b) the Hirox digital microscope setup at Texas State University.

The Hirox microscope was used to take 3-D images, where the system uses “focus stacking post-processing” to extend the depth of field. The system allows for determination of the highest and lowest “z-position” of the object being observed. Once these values are determined, the system allows for the number of “captures” to be taken within this specified z-range. The system is then executed and begins capturing the number of images while moving through the range in the z-direction to compile a 3-D image.

3: FE-PLA 3D PRINTED FILAMENTS

In this chapter, the research surrounding the Fe-PLA 3-D printed filaments and the effects of magnetic field assisted additive manufacturing, or MFAAM, will be covered. Three different filaments composed of polylactic acid (PLA) and iron (Fe) particles were 3-D printed via fused filament fabrication, two of which were printed using MFAAM. These filaments were then measured using the MicroSense EZ Biaxial VSM to explore the influence that MFAAM had on the filaments' magnetic properties. Various hysteresis measurements were taken as a function of magnetic field strength and magnetic field angle to investigate potential effects on the samples' susceptibility and magnetic anisotropy. The role that the demagnetizing field played in the samples' hysteresis slope will also be covered in this chapter. To support the results found using the VSM, alternative characterization methods were employed such as x-ray diffraction and digital microscopy.

3.1 Printing Process & Sample Preparation

3.1.1 Material Properties

The material that was used to print the samples for this research was a magnetic Fe-PLA thermoplastic filament supplied by Proto-pasta. Magnetic Fe-PLA is a combination of finely ground iron powder and NatureWorks polylactic acid (PLA) [61]. The iron particles were observed via optical microscopy to be approximately 40 μm in diameter, and previous research of this material revealed a density of approximately 2 g/cm^3 , a tensile strength of 49.11 MPa, a tensile modulus of 4.723 GPa, a specific strength of

24.55 MPa cm³/g, a specific modulus of 2.361 GPA cm³/g, and a volume resistivity of 2.7e¹² Ohm-cm [62].

3.1.2 3-D Printer Setup & Parameters

The samples in this research were printed using a water-cooled RoVa3D 3-D printer from ORD Solutions. This printer was equipped with a print nozzle of 0.5 mm in diameter to print single strand filaments for magnetic characterization and larger samples with 100% infill fraction for XRD characterization. The samples were printed with an extrusion multiplier of 0.95, a retraction distance of 5 mm, and a retraction speed of 4800 mm/min. The printing temperature was 200° Celsius and a constant print bed temperature of 45° Celsius was used during deposition. To improve the adhesion of the samples to the permanent magnets and the print bed, ethylene vinyl acetate (EVA) was applied to the print surface prior to printing. A picture of the printer setup can be seen below:

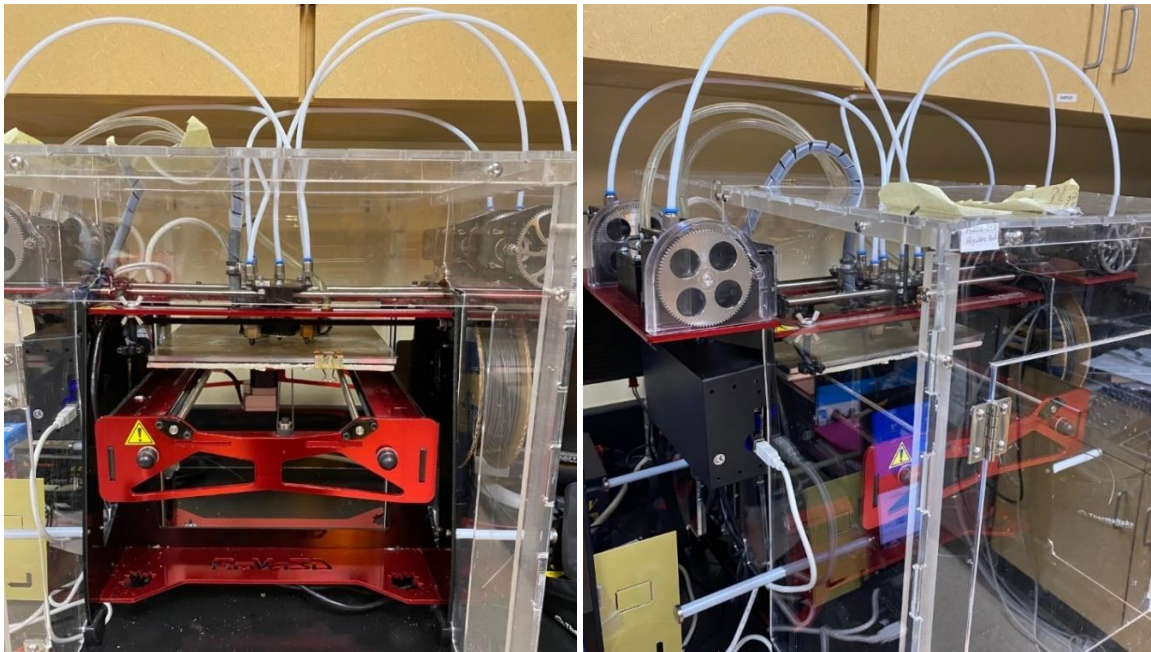


Figure 3.1 a) Front view and b) side view images of RoVa3D 3-D printer at Texas State University.

Fused filament fabrication (FFF), also known under the trademarked term fused deposition modeling (FDM), was the 3-D printing process that was used to print these filaments. FFF uses a continuous filament of thermoplastic material and melts it using a heated nozzle. Once melted, the material is then extruded through the nozzle onto a print bed in a constant direction. This printing method takes a two-dimensional approach, raising the height once one layer has completed printing to add the next layer until the desired 3-D product is finished.

The method of FFF to print these filaments was modified by introducing an applied magnetic field to the print bed during printing in order to theoretically induce preferred orientation of the magnetic particles and enhance the susceptibility of the material. This process is referred to as magnetic field assisted additive manufacturing, or MFAAM. MFAAM has been studied on hard magnetic materials and has shown appreciable effects on the magnetic properties of such 3-D printed composites [5, 21, 22]. The objective of this research was to determine whether these same effects can be applied to soft magnetic materials. This magnetic field was supplied by 25x25x25 mm³ cube Neodymium (NdFeB) magnets of grade N52 with $BH_{max}=50-53$ MGOe which were placed on the printing platform. The setup of the printed filament and permanent magnets can be seen below:



Figure 3.2 MFAAM sample printed on NdFeB permanent magnets on top of 3-D printer's platform.

These magnets were used to supply various magnetic field strengths during printing by orienting the magnetic Fe particles within the extrudate. It is important to note that while the magnetic field does attract the filaments to the magnet via magnetic force, there was no clogging of the nozzle that was observed. These filaments were printed using a constant extrusion direction to print single strand filaments, all consisting of 100% magnetic composites without voids with little observed variation of the magnetic properties among multiple samples.

3.2 Experimental Procedure

Samples of three different field strengths were printed using the method described above: a control sample that was printed in zero field, a sample that was printed with the applied field parallel to the cylindrical axis of magnitude 8kOe, and a sample printed with the applied field perpendicular to the cylindrical axis of magnitude 5kOe. So, the sample printed in a field of 8kOe had the print field oriented parallel to the length of the filament and the sample printed in the 5kOe field had the print field oriented perpendicular to the length of the filament. Schematics of the printing process for different field directions including the print bed normal, denoted “ \mathbf{n}_z ” are displayed below:

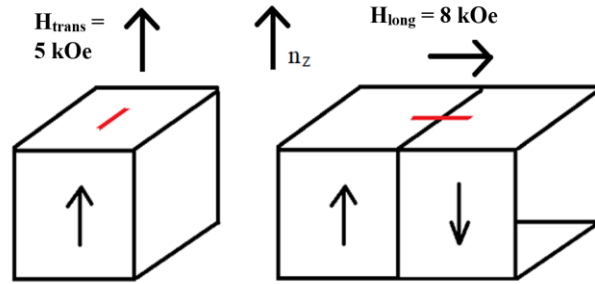


Figure 3.3 Schematics of MFAAM printing method for transverse (H_{trans}) and longitudinal (H_{long}) print-fields. Also indicated is the direction of the print normal " n_z ."

The print field values were estimated using Hall probe measurements that were taken above the permanent magnets. Hall probe measurements take advantage of the Hall effect by placing a thin film of metal in the magnetic field and measuring the transverse voltage that arises due to the separation of charges via the magnetic force [63]. These measurements revealed a fluctuation of magnetic field values along the samples' cylindrical axes; a range of 5300-5500 Oe was observed for the transverse print field sample and a range of 7000-8200 Oe for the longitudinal print field sample. These values obtained from Hall probe measurements are rough estimates since the size of the probe creates difficulty when measuring such small samples. The print field angle varied approximately from 0° in the center to 15° near the ends of the longitudinal sample. A permanent marker was used on each sample to indicate the surfaces that were perpendicular to the print-bed normal n_z .

After printing, the samples were cut, and the dimensions were measured with a caliper. Their mass was also measured using an A-160 scale from Fischer Scientific, and these parameters are all listed below:

Table 2. Dimensions and mass of all three samples being measured via VSM.

	Zero-Field	5 kOe Transverse	8 kOe Longitudinal
Width (mm ± 0.05)	0.74	1.28	1.18
Length (mm ± 0.05)	4.80	6.65	6.80
Height (mm ± 0.05)	0.46	0.78	0.67
Mass (mg ± 0.2)	3.50	12.1	8.50

The samples' magnetic moments were all measured using the MicroSense EZ-9 biaxial VSM at room temperature. Each sample was mounted on an 8mm quartz perpendicular sample holder using museum wax for the adhesive which was applied at room temperature. The 8mm perpendicular rod holder was used to observe the field angle dependence for each sample. The magnetic moment of each sample was measured with respect to the applied magnetic field and the field angle. Field angle measurements were taken using two different mounting configurations for each sample: one configuration had the samples mounted with the longitudinal axis parallel to the applied field and the other with the longitudinal axis perpendicular to the applied field. In both configurations, it is important to note that the print bed normal \mathbf{n}_z was parallel to the normal vector of the sample holder, pointing out of the page. The geometries for these configurations mounted in the VSM at a field angle of zero degrees are shown in the figure below:

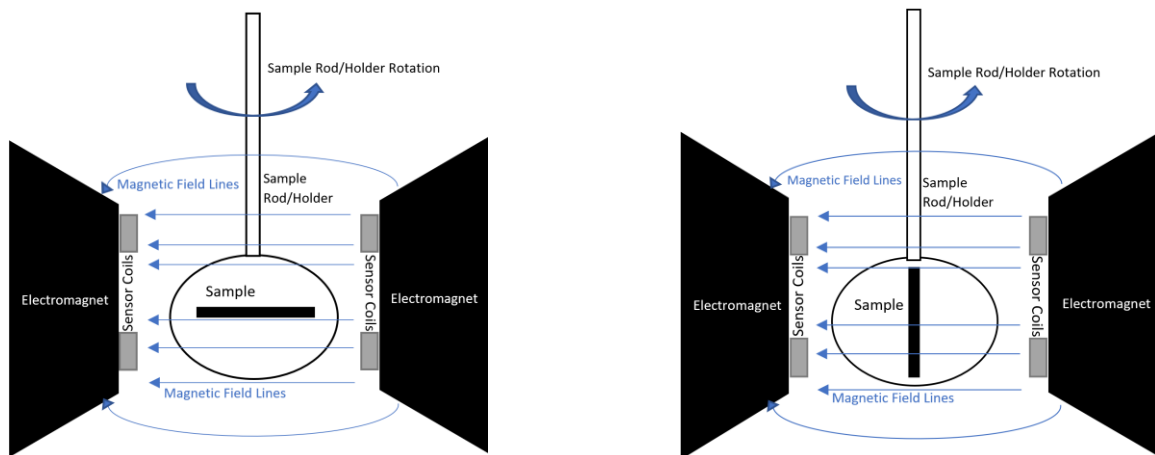


Figure 3.4. Schematic of the biaxial VSM and the placement of the sample when a) oriented horizontally and b) oriented vertically, respectively.

Each samples' hysteresis curves were measured (mounted vertically and horizontally) using sweep field mode, sweeping an applied magnetic field from -22,000 Oe to 22,000 Oe with a sweep rate of 250 Oe/s. The field angle was also varied for each measurement from 0° to 90° in 15° increments. From here, the hysteresis curves of each sample were inspected to observe any changes that MFAAM had on the filament's magnetic properties.

3.3 Graphical Results & Discussion

The first set of curves that were inspected were those of the zero-field printed filament which was used as a reference for the other samples printed using MFAAM. This filament was measured twice via VSM with varying applied field angles. These raw hysteresis curves can be seen below:

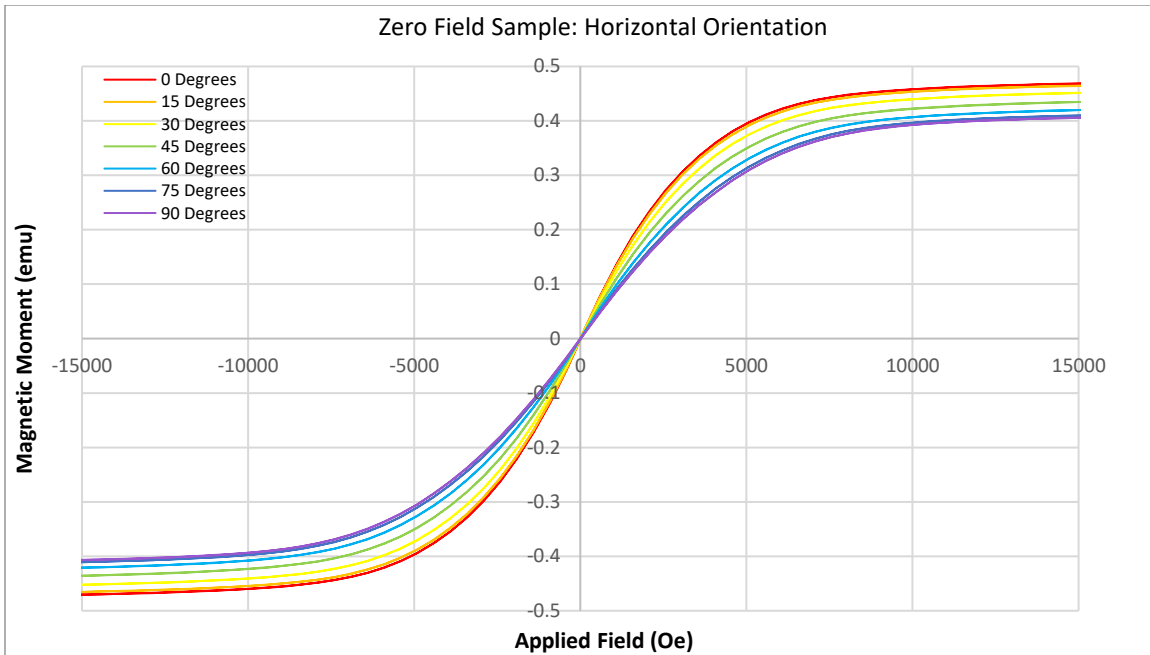


Figure 3.5 Raw data hysteresis of horizontally oriented zero field sample with varying field angles.

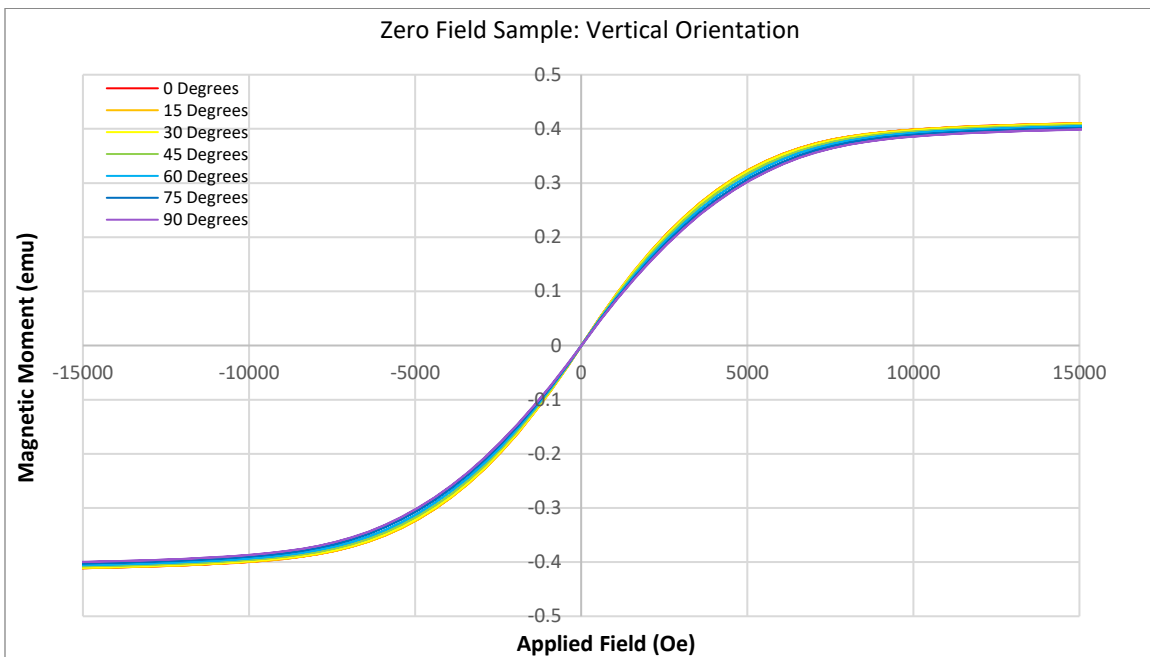


Figure 3.6 Raw data hysteresis of vertically oriented zero field sample with varying field angles.

As seen above, both configurations showed a dependence of the measured saturation magnetic moment on the applied field angle, however figure 3.5 shows that the horizontal orientation displayed a larger dependence. This dependence can be partially attributed to the angular sensitivity of the VSM sensor coils. As the field angle is increased from 0° to

90°, the right and left ends of the sample move away from the sensor coils in the x-direction, which affects the sensitivity of these coils and lowers the M_x signal.

This effect can be corrected for by determining the calibration factor as a function of the field angle for a sample that has the same shape as the sample being measured. Looking to figure 3.6, the vertically oriented sample shows a dependence of the saturated magnetic moment on the field angle as well, albeit much smaller. This dependence is caused by small misalignments of the sample's cylindrical axis with respect to the rotation axis of the sample holder itself. Recent studies have shown that by changing the field angle, the position of the sample in between the pickup coils will change and affect the signal being read in [64]. This error can be compensated for by recentering the sample after each field angle change. Since these samples saturate at high magnetic fields, this thesis will correct for both effects described above by normalizing the hysteresis curves using the measured magnetic moments at high fields.

The following plots show the normalized hysteresis curves for the zero-field sample in both the horizontal and vertical configurations. Figures 3.7 and 3.8 display the normalized curves of the vertically oriented measurements and reveal a slight change in the hysteresis as well as the zero-field susceptibility with respect to the field angle. This suggests that the 3-D printed filament has magnetic anisotropy, which can originate from the crystallographic texture of the material, preferred orientation of the magnetic particles or even the distribution of the particles within the composite [65, 66]. It is important to note that these samples were not printed as perfect cylinders and are slightly thinner along the print normal (see Table 2), so the magnitude of the demagnetizing effects were dependent on the direction in respect to the cylindrical axis. This can be seen in figure 3.8

when comparing the sample measured at 0° compared to it measured at 90° , as the slope of the hysteresis at 90° is smaller due to the demagnetizing field being greater here.

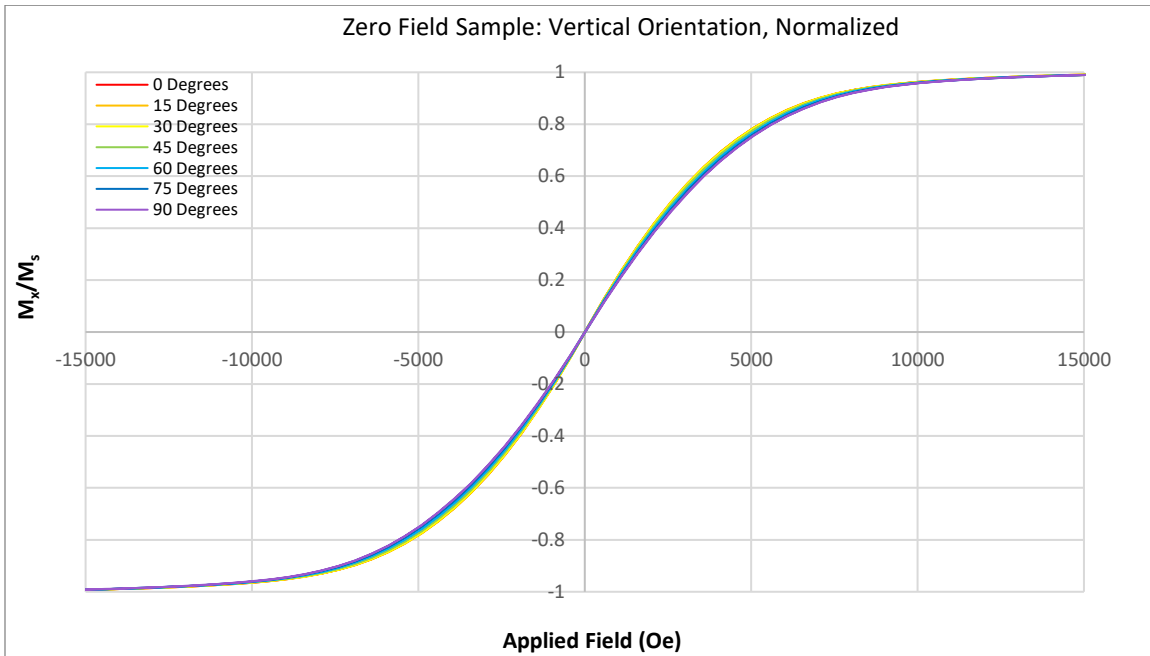


Figure 3.7 Normalized hysteresis of vertically oriented zero field sample with varying field angles.

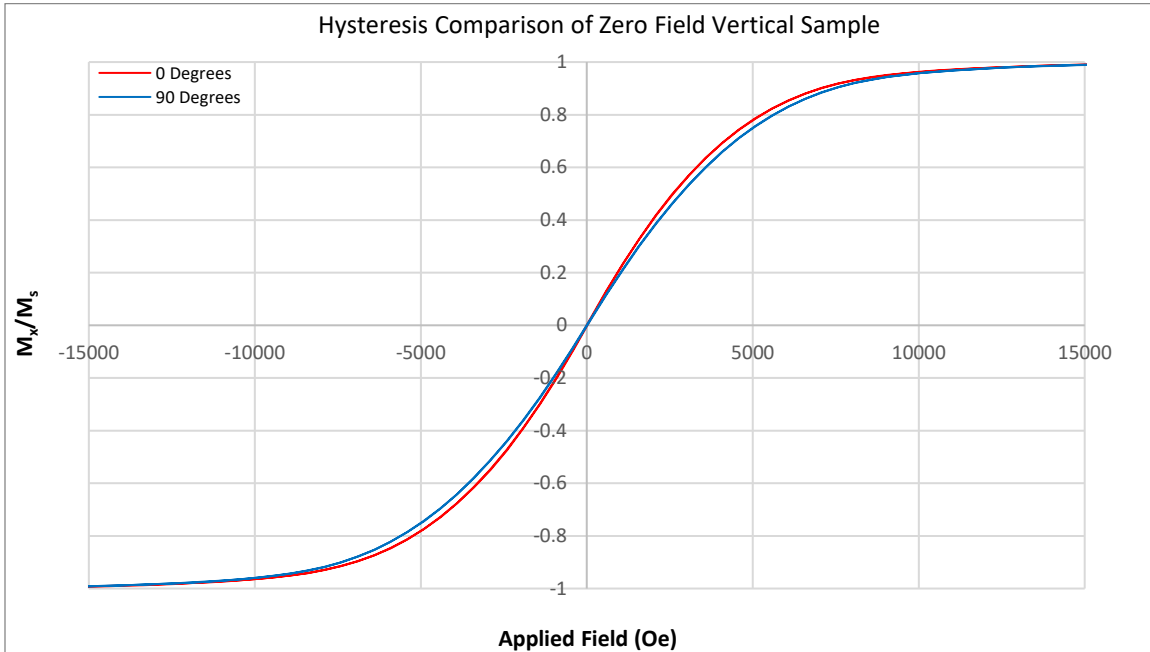


Figure 3.8 Normalized hysteresis of vertically oriented zero field sample at zero and 90 degrees.

The next set of graphs show the normalized hysteresis curves of the zero-field sample measured in the horizontal orientation, displaying a much larger dependence on the

applied field angle compared to the data set of the vertically oriented sample. Figure 3.9 reveals a higher susceptibility at 0° for the zero-field filament than figure 3.7 when measured at the same field angle. The sample saturated faster in the horizontal configuration, suggesting that the sample has an easy axis parallel to the cylindrical axis. However, as the sample is rotated from 0° to 90° , as seen in figure 3.10, the susceptibility drops drastically, and a much higher applied field is required to achieve saturation.

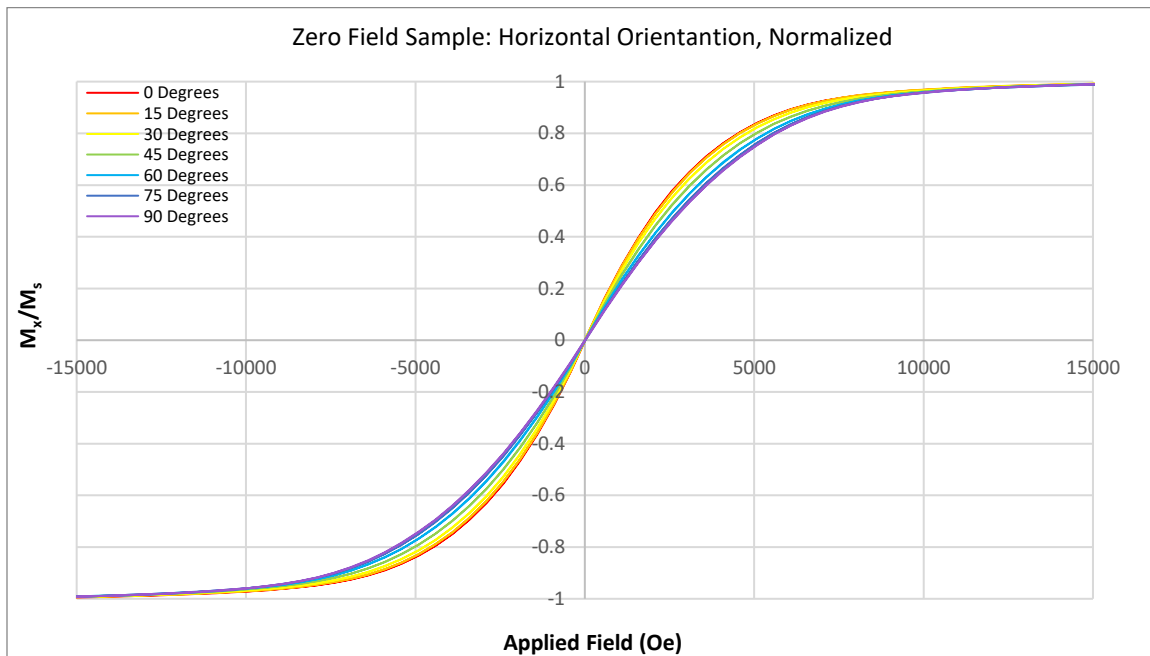


Figure 3.9 Normalized hysteresis of horizontally oriented zero field sample with varying field angles.

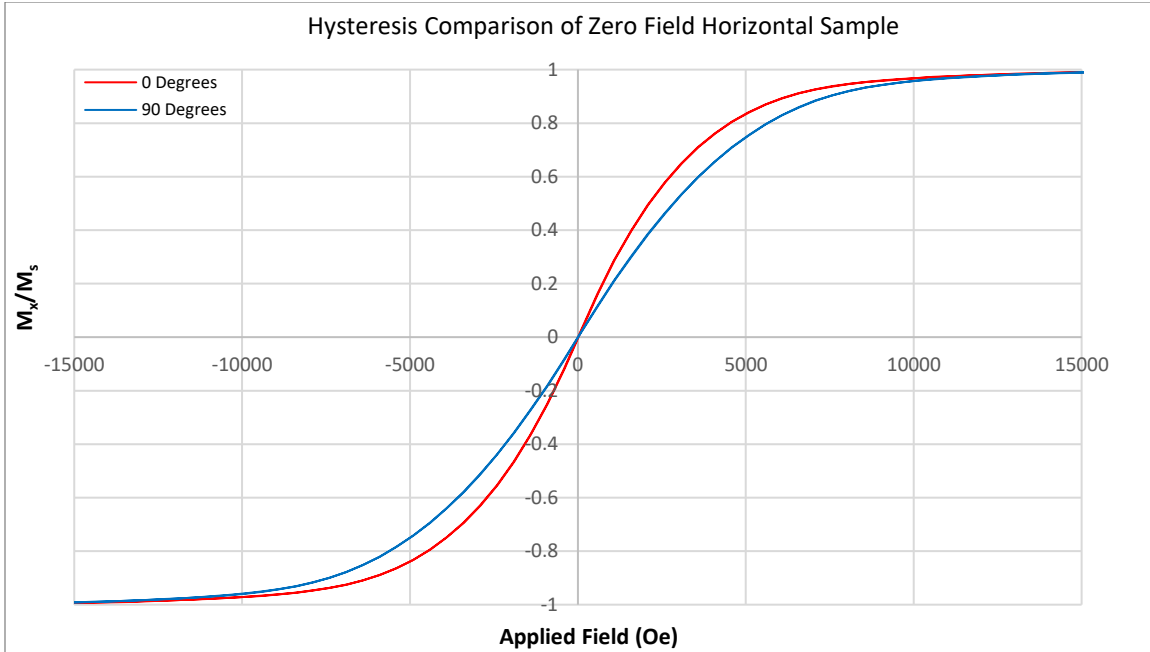


Figure 3.10 Normalized hysteresis of horizontally oriented zero field sample at zero and 90 degrees.

The hysteresis curves of the samples printed using MFAAM were explored next. The samples printed in a 5kOe field perpendicular to the cylindrical axis were examined in the same manner, with figures 3.11 and 3.12 showing the hysteresis curves of the sample measured in the vertical configuration. Referring to these figures, the susceptibility of this sample was heavily dependent on the applied field angle, showing a drastic change in the slope as the sample was rotated. Unlike the zero-print field sample, the susceptibility of the 5 kOe sample was largest when rotated to 90° and lowest at 0°. At zero degrees, the applied field is perpendicular to the print field, but when rotated to 90°, the applied magnetic field is parallel to the easy axis induced by the print magnetic field which was applied parallel to \mathbf{n}_z .

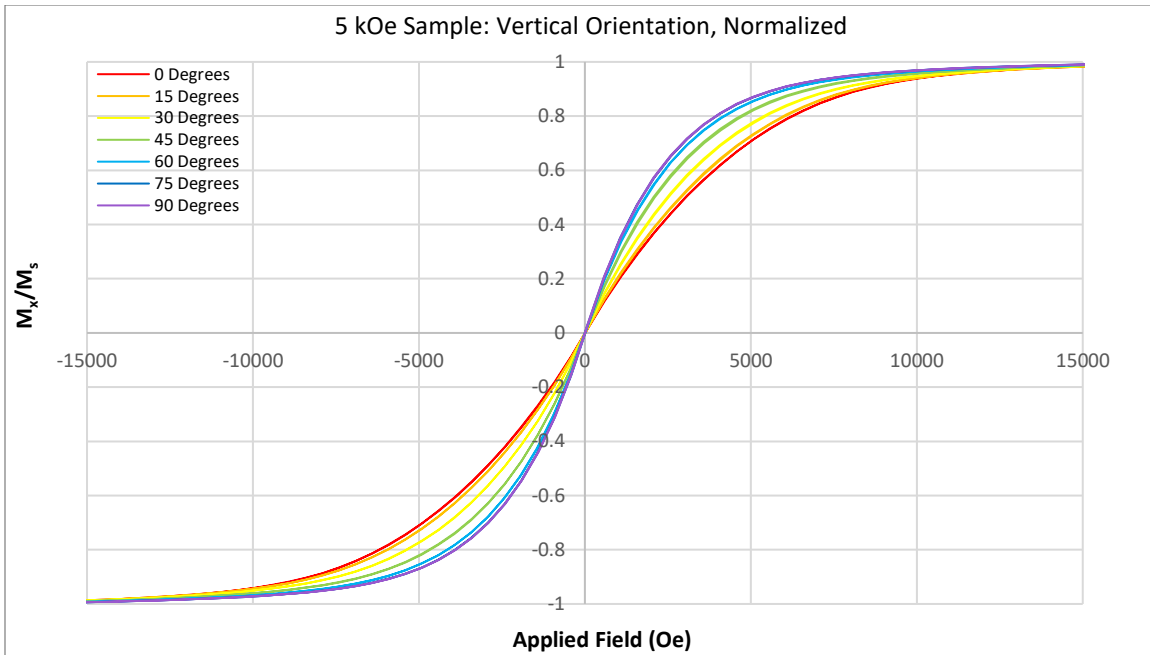


Figure 3.11 Hysteresis measurements for sample printed in a field perpendicular to the cylindrical axis of 5 kOe. Sample is oriented vertically.

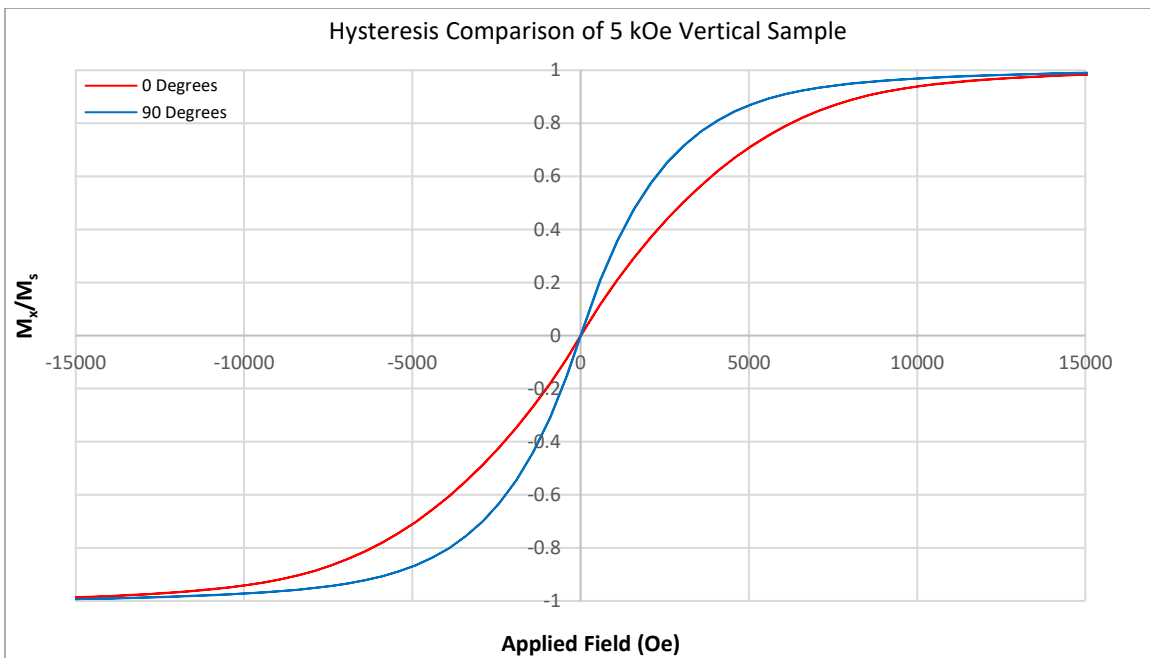


Figure 3.12 Comparison of hysteresis curves for the vertically oriented sample printed in a 5 kOe magnetic field at zero and 90°.

The horizontal measurements of the 5 kOe sample are displayed in figures 3.13 and 3.14 and reveal that saturation occurred at lower fields when the field was applied parallel to \mathbf{n}_z as was the case in figure 3.13 for fields larger than 45°. It can be noted that for the

horizontal configuration measurements, the saturation field is less dependent on the field angle than for the measurements taken in the vertical configuration. It is suspected that this was due to the negligible demagnetizing effects taking place along the cylindrical axis. However, for the measurement taken in the vertical orientation at 0° and 90° , the demagnetizing effect is greater here since these angles are both being measured along the radial axes. It is also important to note that the 90° results are the same for both the horizontal and vertical orientations, as in both instances, the applied field is parallel to \mathbf{n}_z .

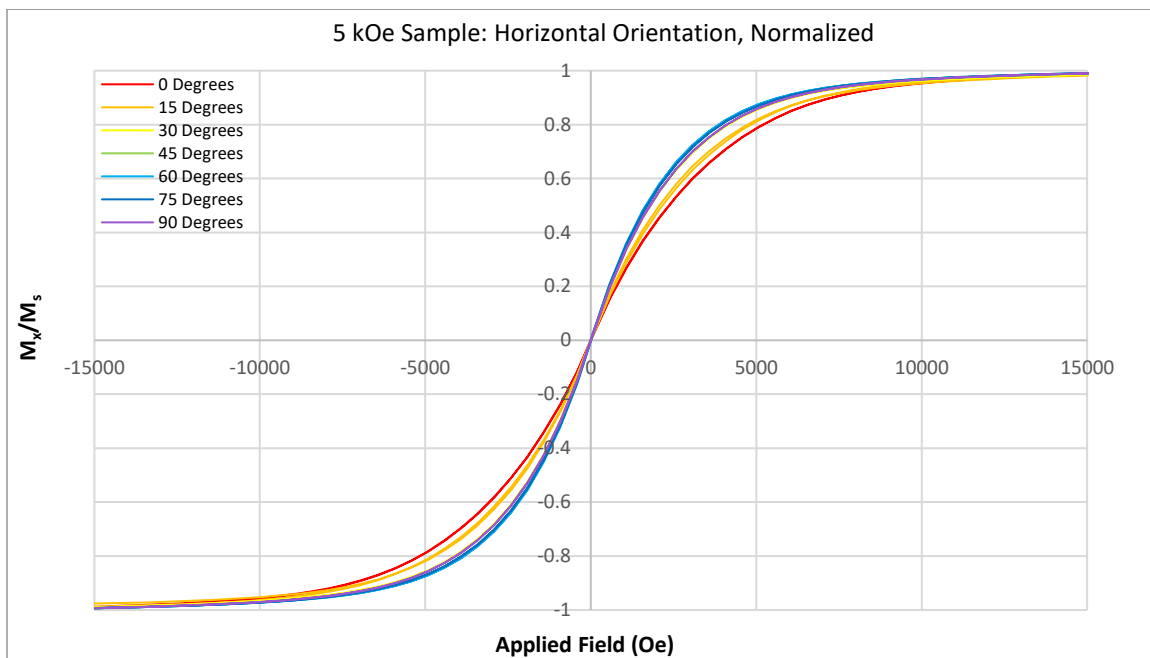


Figure 3.13 Hysteresis measurements for sample printed in a field perpendicular to the cylindrical axis of 5 kOe. Sample is oriented horizontally.

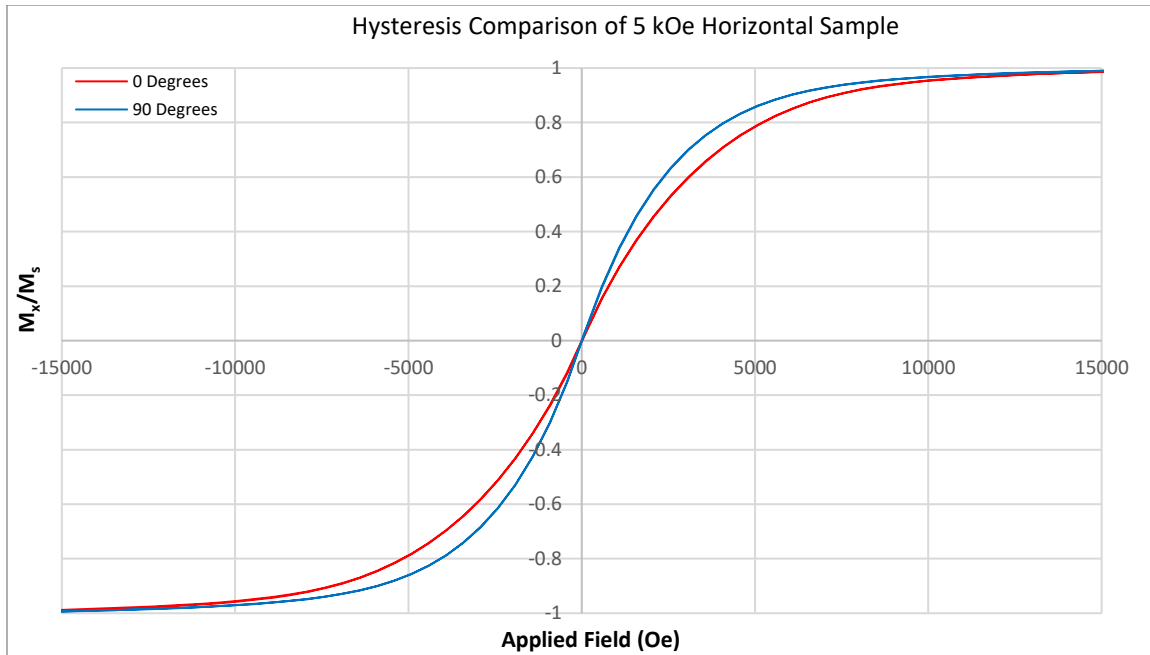


Figure 3.14 Comparison of hysteresis curves for the horizontally oriented sample printed in a 5 kOe magnetic field at zero and 90°.

Lastly, the 8 kOe sample was measured in the same configurations as the samples above. Figures 3.15 and 3.16 show the hysteresis curves measured in the vertical orientation and figures 3.17 and 3.18 show the hysteresis curves for the sample measured in the horizontal orientation, all of which can be seen below. The hysteresis curves for the vertical orientation displayed a slight variance in saturation fields, with the 90° curve showing the highest susceptibility and zero degrees showing the lowest. All curves in figures 3.15 and 3.16 displayed a lower susceptibility as compared to that in figure 3.17 due to the applied field being perpendicular to the print field for all angles in this orientation.

Comparing the hysteresis curves of the 0 Oe and 8 kOe samples when oriented vertically (see fig. 3.8 and 3.16), it was observed that there was a significantly larger field angle dependence for the 8 kOe sample. During printing, this sample acquired transverse

components near the end points and resulted in an inhomogeneous distribution of the print field, which could be the cause of the higher angle dependence seen in figure 3.16.

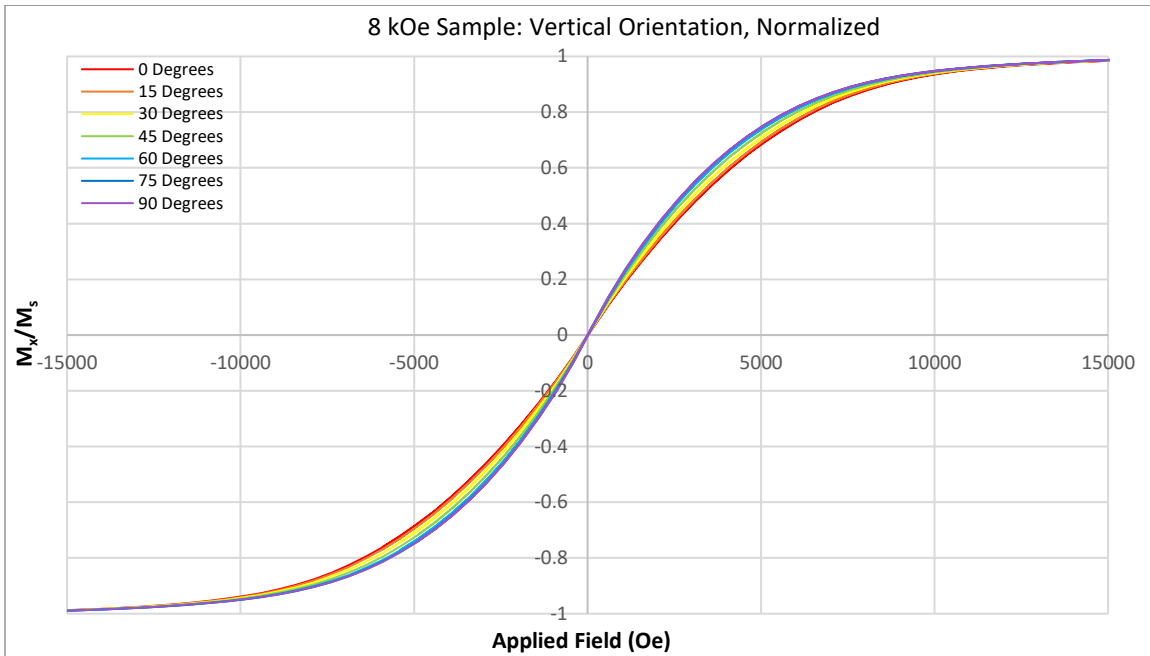


Figure 3.15 Hysteresis measurements for sample printed in a field parallel to the cylindrical axis of 8 kOe. Sample is oriented vertically.

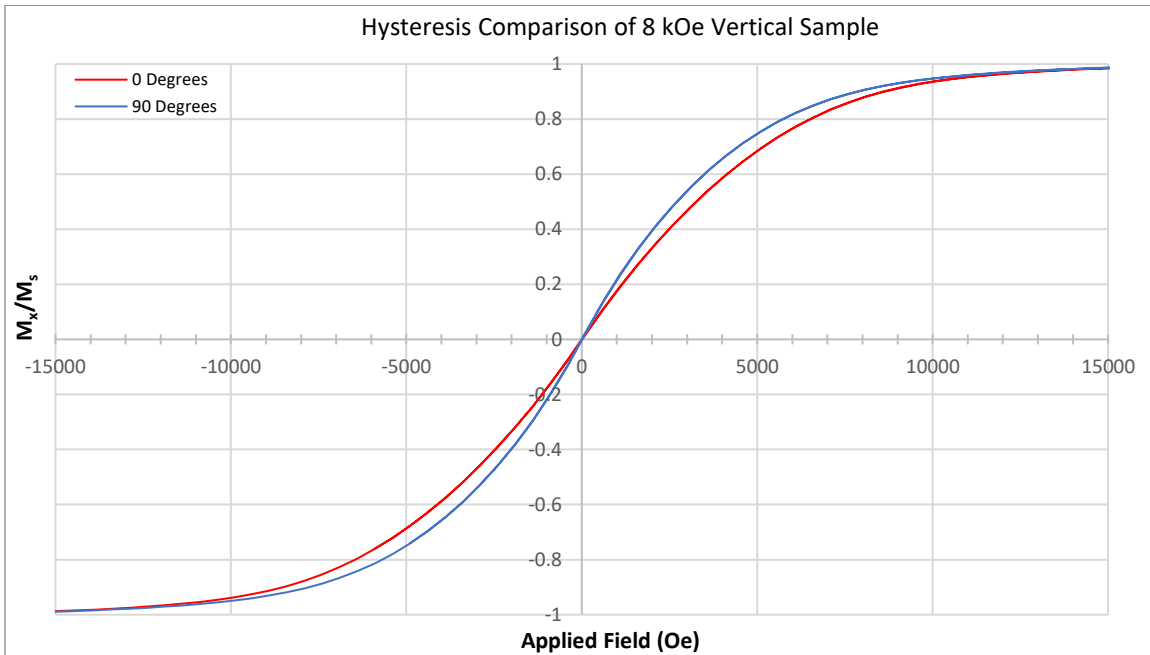


Figure 3.16 Comparison of hysteresis curves for the vertically oriented sample printed in an 8 kOe magnetic field at zero and 90°.

Moving to the hysteresis curves of the 8 kOe sample oriented horizontally, figures 3.17 and 3.18 show a much higher susceptibility compared to the sample oriented vertically, as was seen in the 0° and 15° curves. At zero degrees, the applied magnetic field is parallel to the longitudinal print field, which allowed the sample to saturate much quicker than other field angles observed. Once rotated completely to 90°, the applied field and print field are perpendicular to each other, requiring a much higher applied field for the sample to reach saturation. This angle dependence is illustrated in figure 3.18.

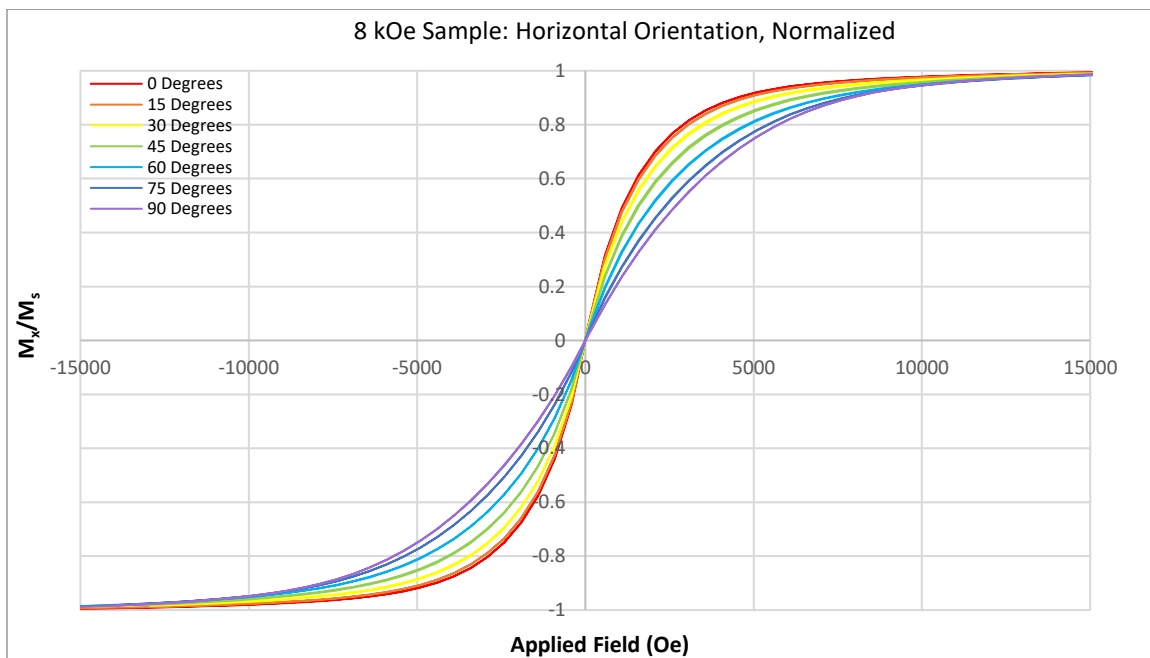


Figure 3.17 Hysteresis measurements for sample printed in a field parallel to the cylindrical axis of 8 kOe. Sample is oriented horizontally.

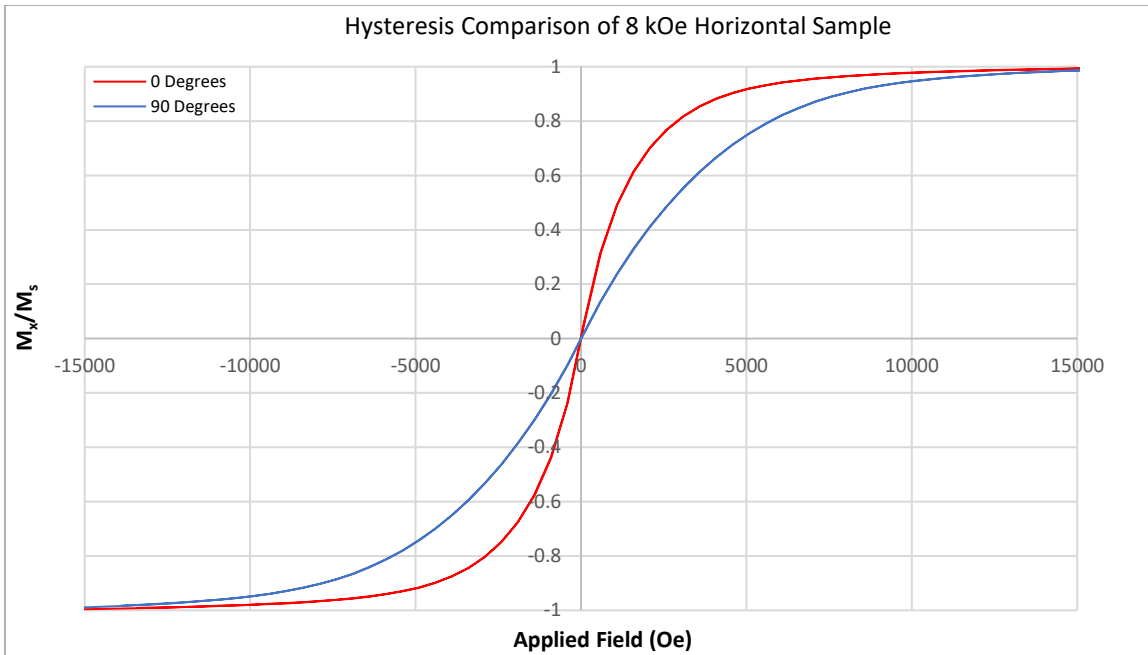


Figure 3.18 Comparison of hysteresis curves for the horizontally oriented sample printed in an 8 kOe magnetic field at zero and 90°.

It should also be noted that for the hysteresis measurements taken for all three samples, the coercivity of each was under 10 Oe and appeared to be independent of the field angle. However, since these measurements were taken in “sweep mode,” the limits of the coercivity values were due to the field lag correction that was applied. While using the sweep mode measurement option, an integration time of 0.1 seconds was employed for continuous measurement, whereas step mode allows for a pause at each desired measurement point before continuing. Thus, the lag between real time measurements and what the system is reading resulted in coercivity values lacking a confidence level high enough to report on.

3.4 Data Analysis & Discussion

The magnetic susceptibility and the magnetic moment per unit mass, or magnetization, of each sample was extracted from the hysteresis curves and was summarized in Table 3,

displayed below. The saturation magnetization, denoted “ M_s ,” should ideally be consistent with each sample. However, due to the relatively large measurement errors in the samples’ masses, the M_s values reported display slight variation with each other. Although a scale with a precision of 0.2 mg was used, the small mass of the filaments introduced a large digital error, thus affecting the values reported for the magnetic moments.

Using the measurements of the vertically oriented samples, the magnetic moment when each sample fully saturated was determined. As described above (see figure 3.5), the horizontal configuration was not calibrated correctly, so to correct for this, the following equation was used to determine the accurate susceptibility of the horizontal measurements:

$$\chi_{meas} = \frac{M_{s,vert}}{M_{s,hor}} \cdot \chi_{raw} \quad 3.1$$

Where χ_{meas} is the corrected susceptibility in the horizontal configuration, $M_{s,vert}$ is the magnitude of the magnetic dipole moment per unit mass of the vertically oriented sample at saturation, $M_{s,hor}$ is the magnitude of the magnetic dipole moment per unit mass of the horizontally oriented sample at saturation, and χ_{raw} is the susceptibility, or slope determined from the hysteresis curves measured in the horizontal configuration. Plugging in the known values for $M_{s,vert}$, $M_{s,hor}$ and χ_{raw} , the corrected measured susceptibility for the curves measured in the horizontal configuration was determined. This corrected susceptibility for the horizontal measurements was compared with the measured susceptibility of the vertical measurements. These values, along with the magnetic

moment per unit mass of each sample at field angles 0° and 90° are presented below in

Table 3:

Table 3. Magnetic susceptibility and saturated magnetic moment at field angles 0° & 90°. The magnetic susceptibility of the horizontally and vertically oriented samples was converted from $\frac{\text{emu/Oe}}{\text{g}}$ to SI units and is therefore unitless.

	χ_{measured} Horizontal Orientation	χ_{measured} Vertical Orientation	χ_{true} Horizontal Orientation	χ_{true} Vertical Orientation	Ms ($\frac{\text{emu}}{\text{g}}$)
0 Field Sample at 0°	0.52	0.41	0.53	0.48	77
0 Field Sample at 90°	0.36	0.36	0.46	0.47	75
5 kOe Sample at 0°	0.52	0.39	0.53	0.45	80
5 kOe Sample at 90°	0.69	0.68	1.23	1.22	79
8 kOe Sample at 0°	0.99	0.32	1.02	0.37	74
8 kOe Sample at 90°	0.41	0.41	0.55	0.54	73

It is important to note that the measurements taken at 90° in both the horizontal and vertical orientations of each sample yielded approximately the same results. This was to be expected since the field angle with respect to the sample was the same for both measurement configurations. However, for the measurements done at 0°, there is a significant difference in susceptibilities. This variation was contingent upon a few factors. For some measurements, such as those conducted with the 8 kOe sample, one configuration was measured with the applied field parallel to the print field, in this case the horizontal configuration, while the other configuration (vertical) was measured with the applied field perpendicular to the print field, which revealed that the susceptibility of the MFAAM samples is anisotropic.

An important factor that could have affected the outcome of the susceptibility for all samples was the demagnetizing field effect. For a material with a finite length that is exposed to a magnetic field, the poles at the ends of the sample create an opposing magnetic field, i.e., the demagnetizing field, that works against the magnetic field being applied to the sample, thus decreasing the internal field of the composite. This in turn heavily affects the susceptibility of the sample being measured. The following image illustrates how the demagnetizing field works:

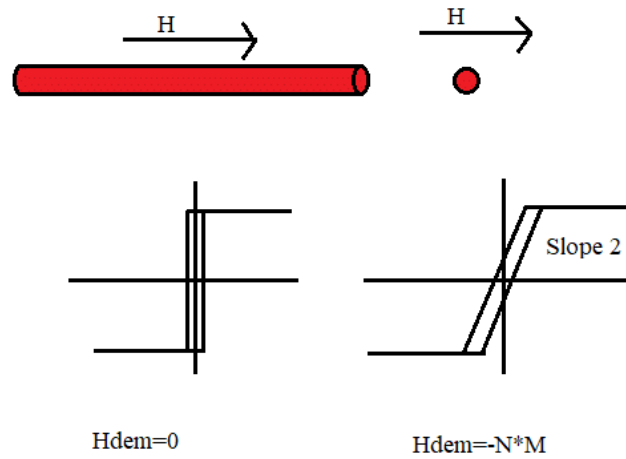


Figure 3.19 Schematic displaying the demagnetizing effect in different directions of a 3-D printed filament [67].

To correct for this, it should be recognized that this effect contributes to the net internal magnetic field that a sample will experience when an external field is applied. Keeping this in mind, the following equation was used to determine the “true” susceptibility of the samples in this research [49]:

$$H_{internal} = H_{applied} - H_{dem} \quad 3.2$$

The magnitude of the demagnetizing field, deemed H_{dem} , depends on the geometry of the samples as well as the orientation of the sample with respect to the applied external magnetic field. Assuming that the demagnetizing field was constant throughout the

sample, equation (3.2) can be rewritten in terms of the demagnetizing factor constant “ N_d ,” so the net magnetic field that the samples experience can be expressed as [49]:

$$H_{internal} = H_{applied} - N_d M \quad 3.3$$

Where N_d is the macroscopic demagnetizing factor which depends on the geometrical shape of the sample and “ M ” is the average magnetization (magnetic moment per unit volume) of the composite. For each sample in this research, the demagnetizing factor had its greatest effect along the shortest axis, which was the height of the printed filaments. The demagnetizing factors in each direction (x , y and z) should theoretically add up to 1 [55, 68]. The smaller the demagnetizing field is, the steeper the slope and the higher the susceptibility will be of the hysteresis measurements and vice versa. The samples in this research were finite in length, so the demagnetizing field was able to be corrected for using the dimensions displayed in Table 2 to calculate the demagnetizing factor and therefore find the true magnetic properties. The following expressions were used to relate the “true” and “measured” susceptibility [49]:

$$\chi_{true} = \frac{M}{H_{internal}} \quad \text{and} \quad \chi_{measured} = \frac{M}{H_{applied}} \quad 3.4$$

By setting both expressions equal to the magnetization “ M ” and substituting equation (3.3) in for “ $H_{internal}$,” the two expressions were equated. With a little rearrangement of variables, the following expression was found for the true susceptibility [49]:

$$\chi_{true} = \frac{\chi_{measured}}{1 - N_d \chi_{measured}} \quad 3.5$$

The demagnetizing factors were estimated using figure 1 from reference [69] as well as the dimensions from Table 2. The approach used here assumes the individual particles of

these samples are ellipsoids. The corrected susceptibilities, denoted by χ_{true} , were recorded in Table 3 and showed that the largest correction came from the measurements where the applied magnetic field was parallel to the shortest axis, which was the height of the samples in this case.

The control sample's susceptibility at 0° measured in the horizontal configuration was compared to the 8 kOe sample at 0° measured horizontally and it was revealed that the susceptibility of the 8 kOe filament increased by a factor of two, providing evidence that MFAAM was integral in enhancing these materials' magnetic properties. This effect on the susceptibility was shown to be even larger for the 5 kOe transverse sample. By comparing the susceptibility at 0° and 90° for both horizontal and vertical configurations of the 5kOe sample, it was shown that the susceptibility increased by a factor of 2.3 and 2.7, respectively. A factor of 2.7 was also observed when comparing the susceptibilities of the 8 kOe sample measured in the horizontal and vertical configurations at 0° , revealing anisotropic behavior for both samples and indicating easy axes parallel to the direction of the applied print field.

3.5 Supporting Characterization Methods

3.5.1 X-Ray Diffraction

To confirm the findings on the magnetic properties of the MFAAM samples, alternative measurements were carried out. Polycrystalline samples have a preferred crystal orientation, also known as crystallographic texture, that contributes to a sample's magnetic anisotropy. The print field was expected to align to the easy axis of the material's particles, and it is well known that iron has a smaller saturation field when the

field is applied parallel to the [100] easy axis directions than parallel to the [111] hard axis directions [52]. XRD θ - 2θ scans were taken for larger Fe/PLA samples printed under similar conditions, i.e., in zero field and a transverse field of 5 kOe printed with a 100% infill fraction. The dimensions of these XRD samples as well as images showing the fill fraction can be seen below:

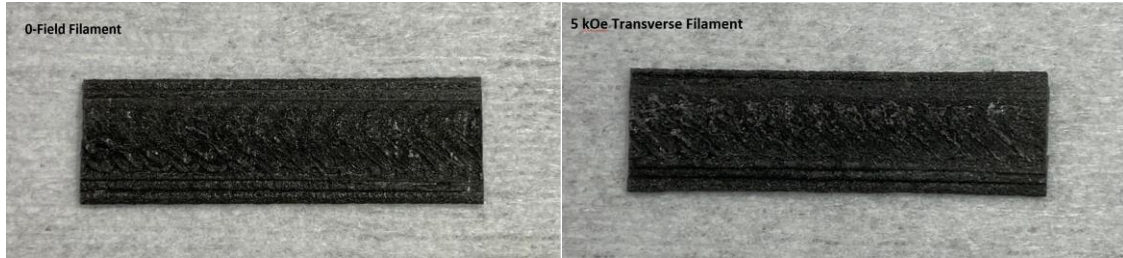


Figure 3.20 Images of 3-D printed Fe/PLA filaments in a) 0-field and b) 5 kOe transverse field for XRD measurements.

Table 4. Dimensions of zero-field and MFAAM 5 kOe samples used for XRD measurements.

	0-Field Sample	5 kOe Transverse Sample
Length (mm ± 0.05)	24.27	23.8
Width (mm ± 0.05)	7.32	6.94

These scans were carried out using the PB/PSA measurement option with a PSA 0.5° slit analyzer, scanning from 5° to 90° with a step size of 0.02° at a speed of $4^\circ/\text{minute}$. The θ - 2θ scans, when compared to literature [70, 71] revealed matching intensity peaks for base-centered cubic (BCC) iron, as well as a broad intensity peak for PLA, which are labeled in the plots below:

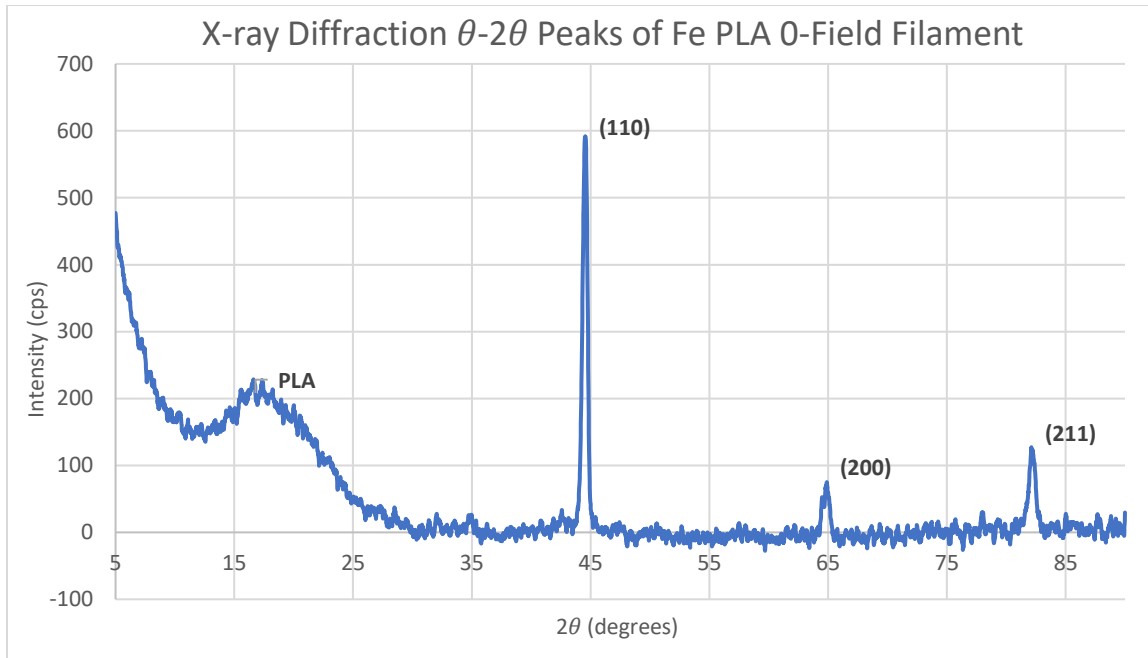


Figure 3.21 XRD pattern of the zero-field Fe/PLA 3-D printed sample displaying peaks for miller indices describing BCC iron and PLA.

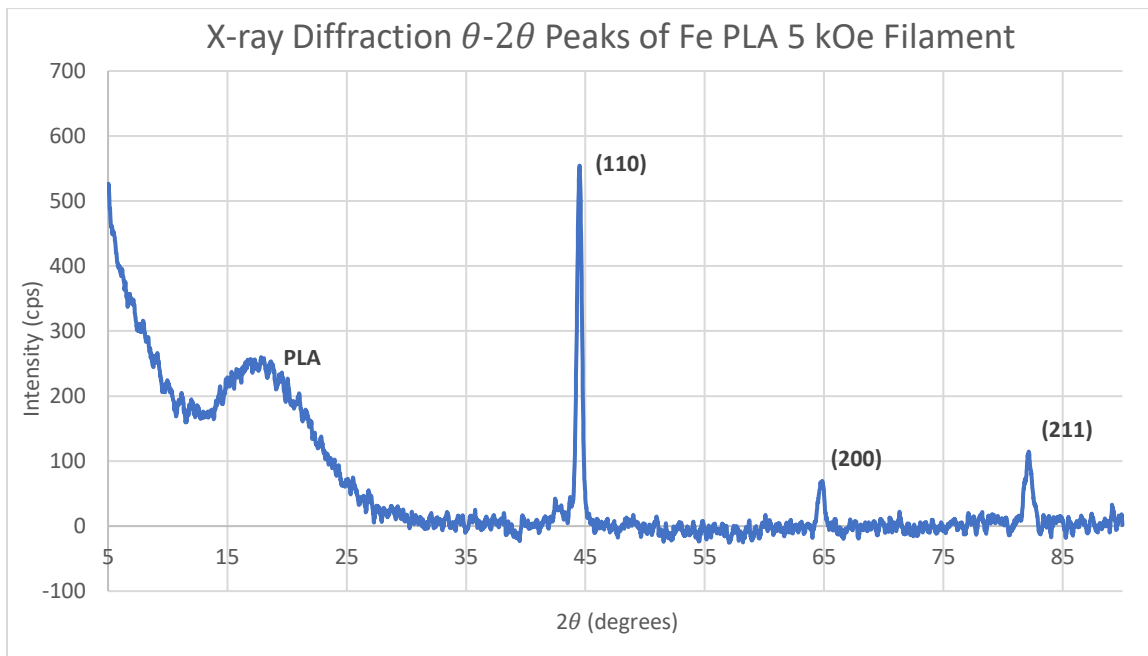


Figure 3.22 XRD pattern of the 5 kOe transverse Fe/PLA 3-D printed sample displaying peaks for miller indices describing BCC iron and PLA.

The absolute intensity values from these scans were used to find the relative intensity of the preferred [200] direction for each filament and revealed that the relative intensity of the (200) diffraction peak, denoted I_{200} , was larger for the MFAAM sample, i.e.

$$\frac{I_{200}}{[I_{200} + I_{110} + I_{211}]}$$

3.6

was larger for the MFAAM sample printed in a 5 kOe transverse field, suggesting a field induced crystallographic texture. Here, the denominator in equation (3.6) is the sum of the intensities of the diffraction peaks observed in the θ - 2θ scans for the Fe-PLA samples. A tabular summary of these peak intensities and ratios of the preferred direction for the 0-field sample and MFAAM sample is presented below:

Table 5. XRD results for 0-field and 5 kOe transverse samples measured using $\theta/2\theta$ scans. Relative intensity for each sample in the (200) direction is given by percentage.

	Miller Index	2θ (Degrees)	Absolute Peak Intensity (cps)	Relative Peak (200) Intensity (%)
0-Field Sample	(110)	44.64	556.38	8.12
	(200)	64.98	59.41	
	(211)	82.17	116.21	
5 kOe Sample	(110)	44.58	518.28	9.51
	(200)	64.88	66.54	
	(211)	82.16	114.71	

3.5.2 Optical Characterization

Other effects could have also contributed to the observed magnetic anisotropy such as shape anisotropy of the individual particles and possible chaining aggregates of the particles, which has been observed in magneto-rheological fluids [65, 66] as well as magneto-elastic composites [25]. Although chaining links are more pronounced in low viscosity inks, this effect was recently observed in MFAAM Strontium Ferrite-PA12 samples printed using FFF [5]. This possibility was explored for the MFAAM Fe-PLA 3-D printed filaments using the Hirox digital microscope. Each sample was thinly sliced and sealed between two glass slides with a soap water mixture. The control zero-field sample was cut so that the cross section of the sample was parallel to the radial plane of

the filament and the two MFAAM samples were cut so that their cross sections were parallel to their respective print field direction. Further inspection of the individual iron particles in the Fe-PLA samples of the zero-print field, 8kOe parallel field and 5kOe transverse field filaments via digital microscopy suggested chaining effects were present in the samples printed using MFAAM. Below are cross sectional images that were taken using an MXB-2500REZ lens and employing the 3-D image tool available through the RH-2000 software. This option uses focus stacking post-processing to allow for a collection of separate images to be taken at different heights in the z-direction and compiled to produce a 3-D image. These images can be seen below:

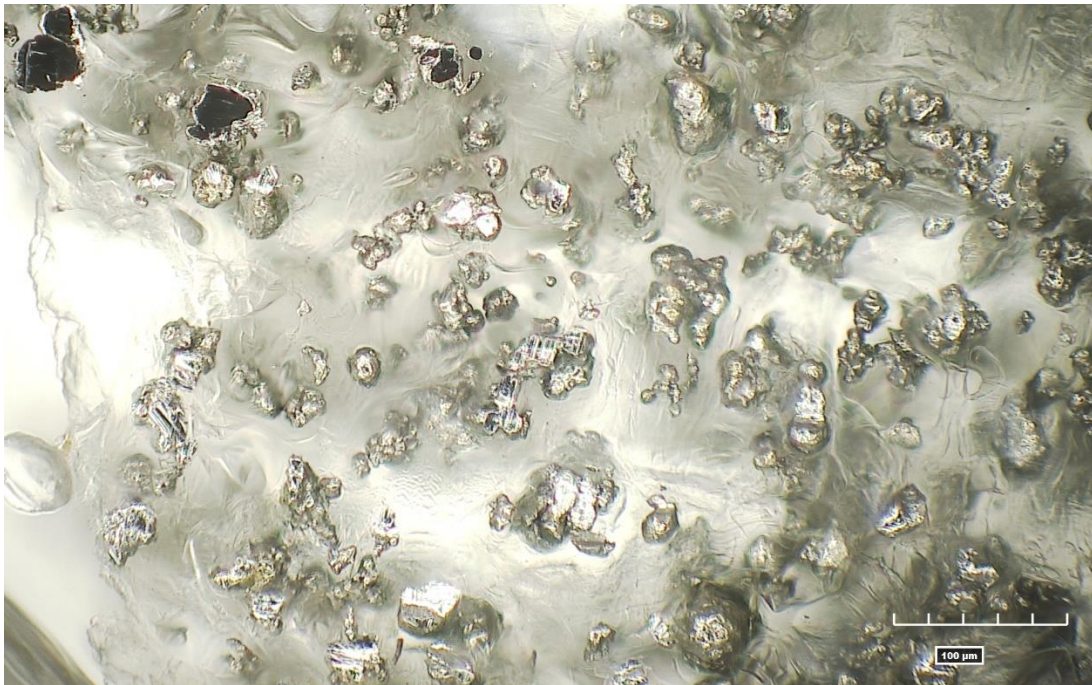


Figure 3.23 Cross sectional optical microscope image of the zero-field 3-D printed filament.



Figure 3.24 Cross sectional microscope image of the 5kOe transverse field 3-D printed filament. Chaining in the applied field direction is defined by the circled aggregates.



Figure 3.25 Cross sectional microscope image of the 8kOe parallel field 3-D printed filament. Chaining in the applied field direction is defined by the circled aggregates.

First looking to figure 3.23, it is apparent that there are magnetic clusters present within the sample printed in zero magnetic field, but not in any preferred direction. However, when looking to the MFAAM printed filaments, there is clear evidence of particle

aggregation in the direction that the external magnetic field was applied during printing. These magnetic chains contribute to the magnetic anisotropy that was observed in the MFAAM printed filaments through additional induced shape anisotropy.

4: FE-DOPED GALLIUM OXIDE THIN FILMS

The research surrounding the magnetic properties of Fe-doped Ga_2O_3 thin films will be covered in this chapter. Two different phases of epitaxial $(\text{Ga}_{1-x}\text{Fe}_x)_2\text{O}_3$ thin films, monoclinic $\beta\text{-Ga}_2\text{O}_3$ and cubic spinel $\gamma\text{-Ga}_2\text{O}_3$, were grown via pulsed laser deposition for various concentrations of Fe ($x=0.02\text{-}0.75$). These thin films were investigated using both the MicroSense Biaxial VSM and the DynaCool PPMS VSM to explore their magnetic behavior and the dependence that their magnetic properties have on magnetic field strength, iron concentration, and temperature. The magnetic hysteresis of these samples was measured using an applied magnetic field oriented parallel with the plane of the thin films. For select concentrated samples, the dependence of magnetic moment per unit volume versus temperature was explored. An in-depth explanation of the inner workings of these measurement systems beyond what was discussed in chapter 2 and the effect of sensitivity on the data collected will be discussed in this chapter as well.

4.1 Growth of Thin Films

4.1.1 Pulsed Laser Deposition (PLD)

The thin films used in this thesis were grown by Dr. Dalim Mia [14] on a (0001) sapphire Al_2O_3 substrate using a technique known as pulsed laser deposition (PLD). PLD is a subcategory of the broader category physical vapor deposition (PVD) and is beneficial for high quality thin films due to the stoichiometric removal of the target material from a fast ablation process as well as the tunability of the rate at which the atoms hit the substrate, made possible by the introduction of an inert gas atmosphere [72]. PLD employs a high-energy laser that emits pulses through a lens at a given target material

kept under vacuum. The laser radiation hits the target's surface and quickly evaporates the material, yielding an ablation plume of atoms that is then collected on the substrate (also in vacuum). The rate at which these atoms hit the substrate is controlled by introducing gases such as oxygen or argon into the atmosphere, which increase the scattering rate and slows them down [72]. A schematic showing the process of PLD is shown below:

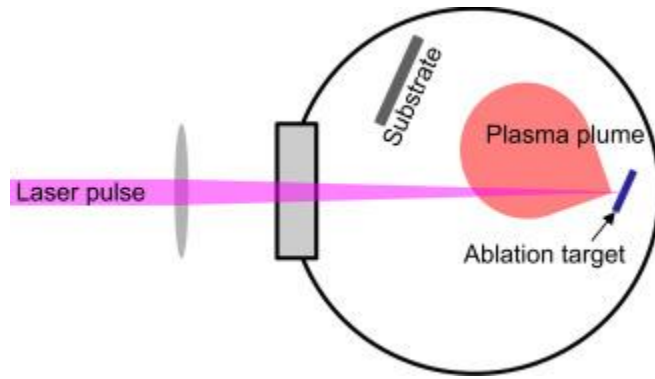


Figure 4.1. Schematic displaying the setup for pulsed laser deposition from Sarangan's "Nanofabrication" [72].

The Fe-doped Ga_2O_3 thin films measured in this thesis were grown at a partial O_2 pressure of 1.5×10^{-6} torr and a temperature of 700°C . A KrF excimer laser with a wavelength of 248 nm and a nominal pulse duration of 25 ns was used along with a frequency of 5 Hz and an energy density of 2 J/cm^2 . [14].

4.2 Experimental Procedure

Ferromagnetic behavior has been observed at room temperature in various other studies involving Fe-doped Ga_2O_3 samples, such as the work done by Hojo et. Al in which they observed room temperature ferromagnetic behavior in Fe-doped $\beta\text{-Ga}_2\text{O}_3$ thin films for iron concentrations of $x= 0.02, 0.05, 0.08,$ and 0.1 [73]. Furthermore, Huang et al. successfully doped the $\gamma\text{-Ga}_2\text{O}_3$ polymorph with iron and realized high saturation

magnetization at room temperature as well [48] The purpose of this sub-thesis project was to not only confirm these previous findings, but to investigate whether the same ferromagnetic behavior can be seen at these specific Ga_2O_3 crystal phases for higher iron concentrations and at different measuring temperatures. Such findings would be monumental for spintronics applications.

Five samples of $(\text{Ga}_{1-x}\text{Fe}_x)_2\text{O}_3$ thin films were grown for different concentrations of Fe (x) using the deposition PLD. Once grown, these thin films were characterized via XRD θ - 2θ scans and it was observed by Mia [14] that depending on the iron concentration, the films took on two separate polymorphs: monoclinic β - Ga_2O_3 and spinel cubic γ - Ga_2O_3 . For concentrations below 10% ($x < 0.1$), the samples took on the stable monoclinic phase structure, and for concentrations above 10% ($x > 0.1$), the thin films transformed into the metastable spinel cubic phase structure, so this thesis will be investigating samples inheriting both monoclinic and spinel phases.

The thin films were cleaved to smaller sizes in order to measure the magnetic properties using the MicroSense VSM and the DynaCool PPMS. The dimensions of each sample were measured using a caliper and their respective masses were measured using an A-160 scale from Fischer Scientific. These parameters are displayed below along with the respective thicknesses of each thin film according to iron percentage:

Table 6. Dimensions for different concentrated Fe-doped Ga_2O_3 thin films grown via PLD. Thickness values were retrieved from the dissertation of Dalim Mia [14].

	$\beta\text{-Ga}_2\text{O}_3$		$\gamma\text{-Ga}_2\text{O}_3$		
Iron Concentration (%)	75	40	15	5	2
Length (mm \pm 0.05)	3.73	6.37	6.1	4.13	5.1
Width (mm \pm 0.05)	3.40	4.17	3.57	2.97	3.2
Thickness (nm)	55.00	52.00	110.0	52.00	140.0
Mass (mg \pm 0.2)	23.3	43.5	35.9	19.7	25.1

The samples' hysteresis and magnetic moments were measured using both the MicroSense Biaxial VSM and the DynaCool PPMS VSM insert. The thin films were measured with the applied field oriented parallel to the plane of the thin films for both systems. For the monoclinic structures, this applied field was directed along the (-201) plane and for the cubic spinel structures, the applied field was directed along the (111) plane [14].

For the VSM insert of the PPMS, each sample was mounted on a quartz rod sample holder using rubber cement as the adhesive which was applied at room temperature. The samples were measured using sweep mode with a magnetic field range of -60,000 Oe (-6T) to 60,000 Oe (6T), a sweep rate of 165 Oe/s, and were subjected to a fixed voltage range of 250 μV . Samples were also measured at a range of temperatures, starting at 400 K down to 5 K using the same magnetic field range and sweep rate described above to observe the temperature dependence on the samples' magnetic properties. When measuring at various temperatures, the samples were measured consecutively in the PPMS, as the PPMS system allows for sequences to be written for multiple

measurements taken in one run. This feature was implemented for different temperature values and select samples were measured for the following temperatures: 400 K, 300 K, 200 K, 150 K, 100 K, 75 K, 50 K, 25 K, 10 K, and 5 K. It is important to note that for measurements occurring at lower temperatures, a “wait” time command was written into the sequences to allow the entire system to come to thermal equilibrium before beginning the measurement.

The MicroSense VSM option was employed to measure the magnetic moments of the variously doped gallium oxide thin films at high temperatures. The 75% iron sample was mounted on a 5mm transverse quartz rod using ceramic adhesive and measured at temperatures above room temperature. The ceramic adhesive was applied to the rod and the sample and rod apparatus was then subjected to a heat gun for 20 minutes to solidify the ceramic. The samples hysteresis curves were measured using sweep mode moment vs. field scans for a field range of -22,000 Oe (-2T) to 22,000 Oe (2T) using a sweep rate of 200 Oe/s. The signal being received is heavily dependent on the vibrational frequency of the system, especially for materials like these with such small signals (which will be discussed in more detail later in this chapter), so a frequency of 75 Hz with a signal range of 10 μ V was used along with an averaging time of 2 seconds to ensure the best quality signal. The thin films were measured at the following temperatures: 298 K, 398 K, 498 K, 598K, 698 K, 748 K, 798 K, 848 K, and 898 K.

The hysteresis curves were then compared against each other to observe the changes in magnetic behavior as a function of iron concentration and temperature. Magnetic properties such as the sample’s saturated magnetization (M_s), coercivity (H_c), and remanence (M_r) were extracted and analyzed to further investigate each samples’

magnetic behavior and confirm whether phase transitions as well as magnetic transitions were prevalent.

4.3 VSM Signal Correction

While VSMs are handy systems used to investigate the magnetic properties of an array of materials, there are some factors to take into consideration that can heavily affect the qualitative and quantitative results. The Fe-doped gallium oxide thin films being measured in this thesis have a relatively weak signal, along the scale of 10 μemu which is nearing the detectable threshold for these systems (signals are detectable signal down to 1 μemu for the PPMS VSM insert and noise is detected down to 1 μemu for the vector option of the MicroSense VSM), so certain factors that could normally be considered negligible for samples with higher signals must be taken into account here.

4.3.1. MicroSense VSM

First looking to the MicroSense VSM, which uses an electromagnet to supply an external magnetic field. When the sample is vibrated in this external field, a changing flux through the detection coils induces a corresponding amount of voltage in the coils. This voltage is read into the software and used to determine a corresponding magnetic moment for the material. The signal is proportional to the following parameters [54]:

- The magnetic moment of the sample
- The vibration amplitude of the sample
- The vibration frequency of the sample
- The centering of the sample within the pickup coilsets
- The shape and size of the sample

For thin films with such a small magnetic moment such as those used in this thesis, it is crucial that these parameters are tailored to the best settings to ensure good quality data.

The vibrational frequency and the centering of the samples were found to have the greatest effect on the measured data. Since the signal received from the VSM is proportional to the time derivative of the coupled flux, the measured moment increases with the vibration frequency.

The following curve shows the average magnetic signal and standard deviation of a piece of Fe-doped Ga_2O_3 as a function of the vibrational frequency, showing that the signal to noise ratio increases with increasing frequency. Since the gallium oxide samples have a fairly weak moment, the lower frequency values did not yield data credible enough to decipher, showing almost no hysteresis or saturation magnetization due to the high noise level as can be seen in figure 4.2 by the increase in noise at low frequencies. At higher frequencies, the noise remains constant at a minimum while the signal increases, so the signal to noise ratio increases as the frequency increases. However, while the increase in vibration frequency causes an increase in the magnetic signal, a frequency too high runs the risk of the sample rods snapping during measurement. The mass of the sample and spring constant of the sample rod create a system that has a specific resonance frequency, and when the vibration frequency of the VSM approaches this resonance frequency, it causes the rod to vibrate too much where it begins to bend and ultimately snap. So, to acquire a detectable signal that compares well with other measurements (such as those taken using the PPMS-VSM) but remain far enough away from the system's resonance frequency to prevent the rod from breaking, a vibrational frequency of 75 Hz was chosen for these measurements.

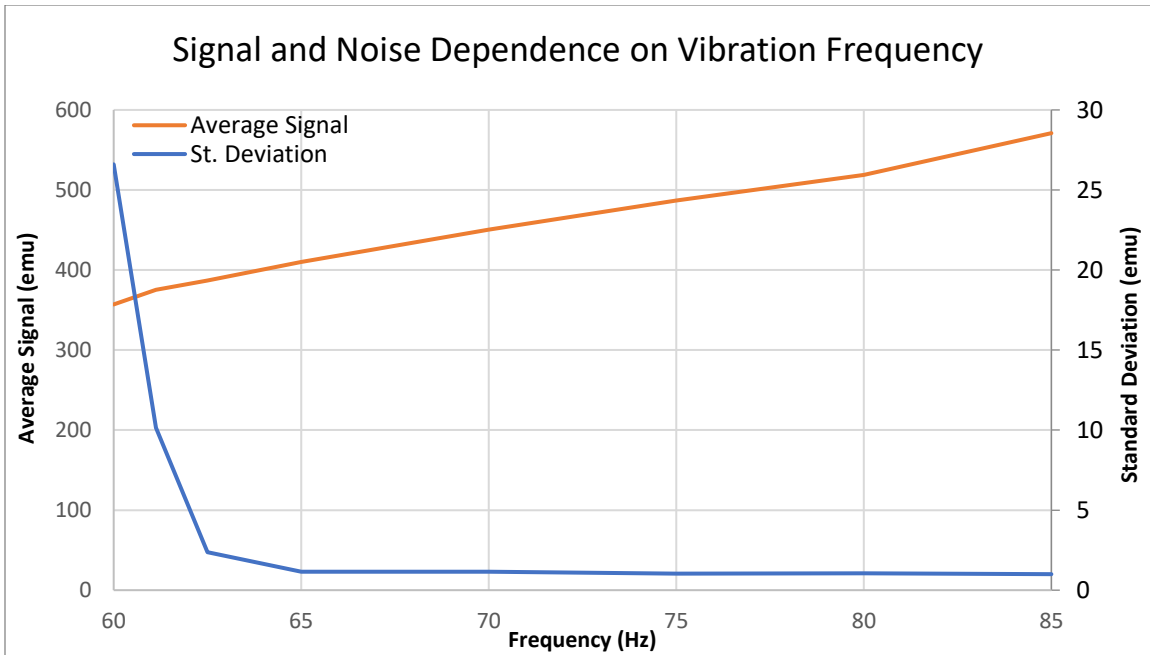


Figure 4.2. Dependence of magnetic signal on the vibrational frequency used for the MicroSense VSM.

Another important factor to consider when measuring samples with weak signals is the averaging time the system uses when measuring at each point. The following graph displays moment vs. field measurements taken using the MicroSense VSM at 75 Hz with an averaging time of 0.1 seconds as well as an averaging time of 2 seconds. These plots are also shown against a moment vs. field scan taken of the same sample using the DynaCool PPMS VSM option with an averaging time of 1 second, and reveal a drastic difference in the noise of the hysteresis curves being scanned depending on the integration time:

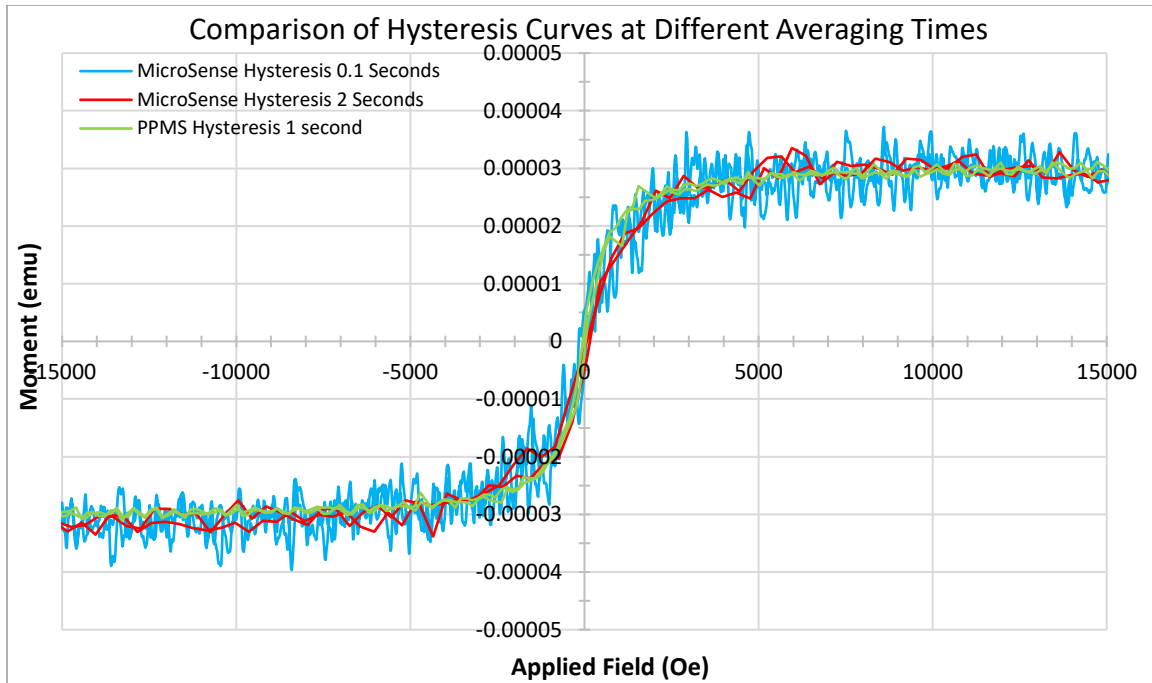


Figure 4.3 Hysteresis curves of the 75% Fe-doped Ga_2O_3 sample with varying averaging times.

The amount of noise seen in the graphs can be reduced to a certain extent by allowing the system to average the signal being detected in the coils for a longer period of time, thus allowing for a more accurate curve with less noise in the data. Increasing the averaging time by a factor 9 will decrease the standard deviation by a factor 3. For the samples measured in this thesis, an averaging time of 2 seconds was used to obtain sufficiently low noise in the hysteresis curves.

4.3.2 DynaCool PPMS VSM

The VSM insert of the PPMS uses a slightly different technique but yields the same results, using a superconducting solenoid instead to supply an external magnetic field in the z-direction in which the changing magnetic flux of the sample induces a voltage through sets of pickup coils. This voltage, proportional to the magnetic moment, can be affected by the following factors [56, 74]:

- The radial offset
- The sample offset
- The center position
- The shape and size of the sample

The factors that were observed to affect the measured moments of the gallium oxide samples the most were the shape and size of the samples, as well as the radial offset. The size and shape of the sample being measured has a direct effect on the accuracy of the moment being measured. To prevent friction between the sample holder and the coilset bore, it is necessary that samples be no wider than 4 mm, as samples wider than this can cause frictional heating, especially at low temperatures, and thus distort the true signal being detected [56]. For samples with weak signals, the sample needs to be centered first using a mounting station before being placed into the chamber and scanned to find the sample offset. The accuracy of the sample offset depends on the precision of the sample being mounted on to the holder using the mounting station, ideally within 0.5 mm from the center. Samples also having an appropriate vertical length well under the baseline of the detection coils, which is 7.1 mm for this system, is important for yielding data confident enough to report on. A sample with a length of 5mm measured at an oscillation amplitude of 2 mm will yield a measured moment that is about 96% that of the true moment with this percentage dropping to approximately 67% for a sample with a length of 10 mm [56], so it is imperative that the samples being measured are within the appropriate dimensions to obtain the most accurate data possible. Note that all sample dimensions of the gallium oxide thin films are within range of these criteria.

Another critical aspect that is the hardest to account for and often overlooked is the radial offset of the sample holder. This offset refers to the radial centering of the sample and rod

mechanism with respect to the coilset once placed inside the chamber. The sample holder is attached to a rod that is approximately 1 meter long and, unless perfectly straight, will yield a measured moment having a periodic dependence on the rotation of the rod about the vibration axis [74, 75]. The following plots show the same sample measured multiple times without taking the radial offset into account (figure 4.4), and then measured again while keeping the radial position constant (figure 4.5). The sample was mounted on a quartz rod using rubber cement only once and then transferred between two rods, deemed rod A and rod B, to investigate any potential effects the sample offset and center position had on the signal as well.

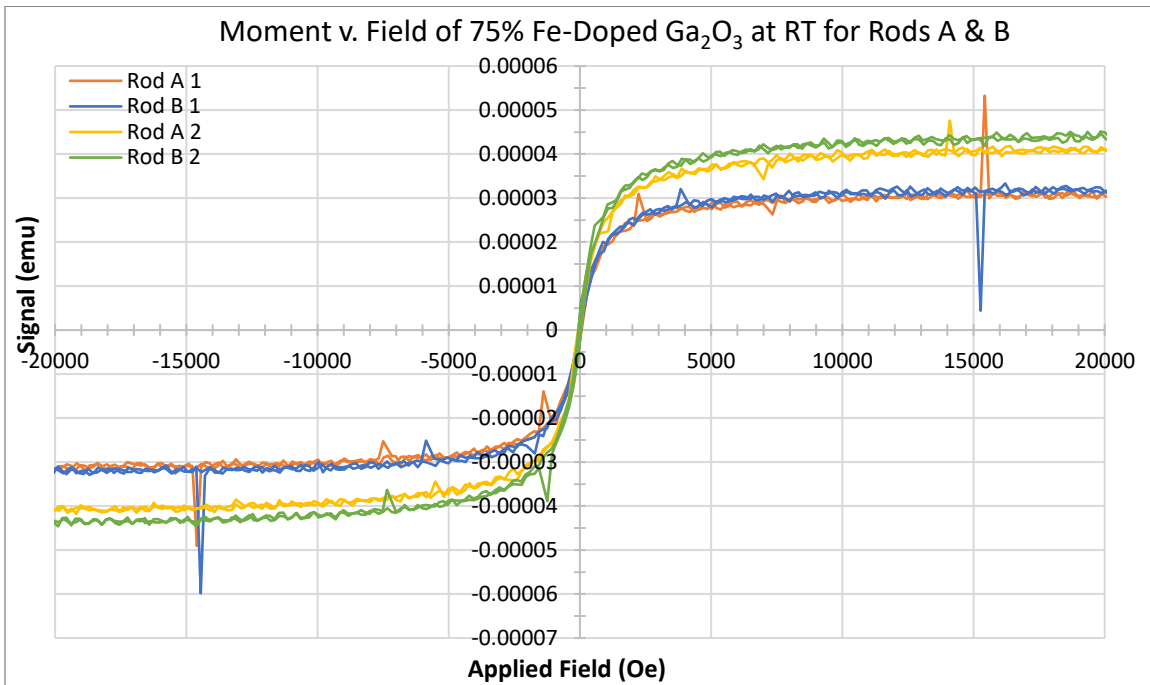


Figure 4.4. Hysteresis curves of the 75% iron sample taken at RT via PPMS VSM for different rods without considering the radial position.

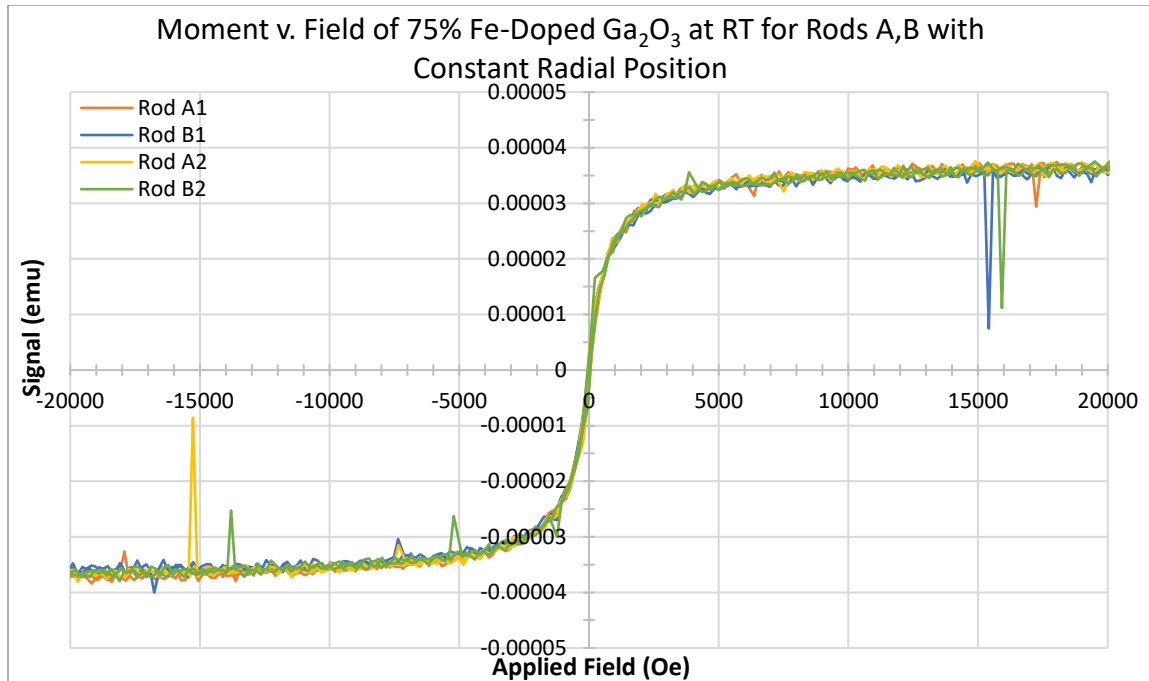


Figure 4.5. Hysteresis curves of the 75% iron sample taken at RT via PPMS VSM for different rods while keeping the radial position constant.

From these plots, it was observed that the greatest effect in the magnitude of the signal was the radial position. Figure 4.4 shows discrepancy between the measurement sets of rod A and the measurement sets of rod B which was initially believed to be originating from the different rod lengths (rod A and rod B differ in length by approximately 1 mm) and thus affecting the sample offset and center position within the coils, but this discrepancy was no longer observed in figure 4.5 when the radial offset was kept constant for all four scans.

Currently, there is no definitive method for the DynaCool PPMS system to account for this offset, so for the measurements taken in this thesis, a mark was made on the top of the rod with respect to the magnetic lock of the linear transport motor to ensure the same radial location for each measurement. Application notes for this system suggest measuring at different angular positions to observe the variations in the measured

moment [74]. The angular position at which the moment is at a minimum value corresponds to the position where the sample is the most centered within the chamber. This method was employed in this thesis to ensure the most accurate magnetic signal for analysis.

One last note regarding figure 4.4 and 4.5 refers to the spikes seen in the data which was observed for most of the PPMS data taken for the Ga_2O_3 samples. These spikes are normally seen at low temperature measurements when the system is not allotted enough time to come to thermal equilibrium. Quantum Design application notes on temperature dependent measurements recommend waiting to take measurements until the designed measuring temperature has been stable for at least two minutes [76]. However, the scans in figures 4.4 and 4.5 were taken at room temperature, so other factors that could possibly explain these spikes in the data are the samples could have been loosely mounted, causing them to not move sinusoidally with the motor and thus causing rattling during measurement, or even loose glue joints on the rod holder itself that could have caused the rod holder to slip during measurement [56]. It can be noted that the spikes appear to be strongest for all measurements near field values of about 15,000 Oe.

4.4 Results & Discussion

4.4.1 Observed Magnetic Behavior

The first set of graphs display the magnetic hysteresis curves that were taken using the DynaCool PPMS at room temperature for both phases of $(\text{Ga}_{1-x}\text{Fe}_x)_2\text{O}_3$ samples where $x=0.75$ for the spinel cubic phase and $x=0.02$ for the monoclinic phase. It should be noted that for all magnetic moment vs. magnetic field curves, the background diamagnetic

signal from the sapphire substrate and the quartz rod holder was subtracted. It has been reported that undoped $\beta\text{-Ga}_2\text{O}_3$ exhibits paramagnetic behavior [14, 48], characterized by no spontaneous magnetization and thus yielding no hysteretic shape. However, looking to figure 4.6 showing the hysteresis curves for samples with monoclinic and spinel cubic structures, it is apparent that the thin films doped with various concentrations of Fe displayed ferromagnetic behavior.

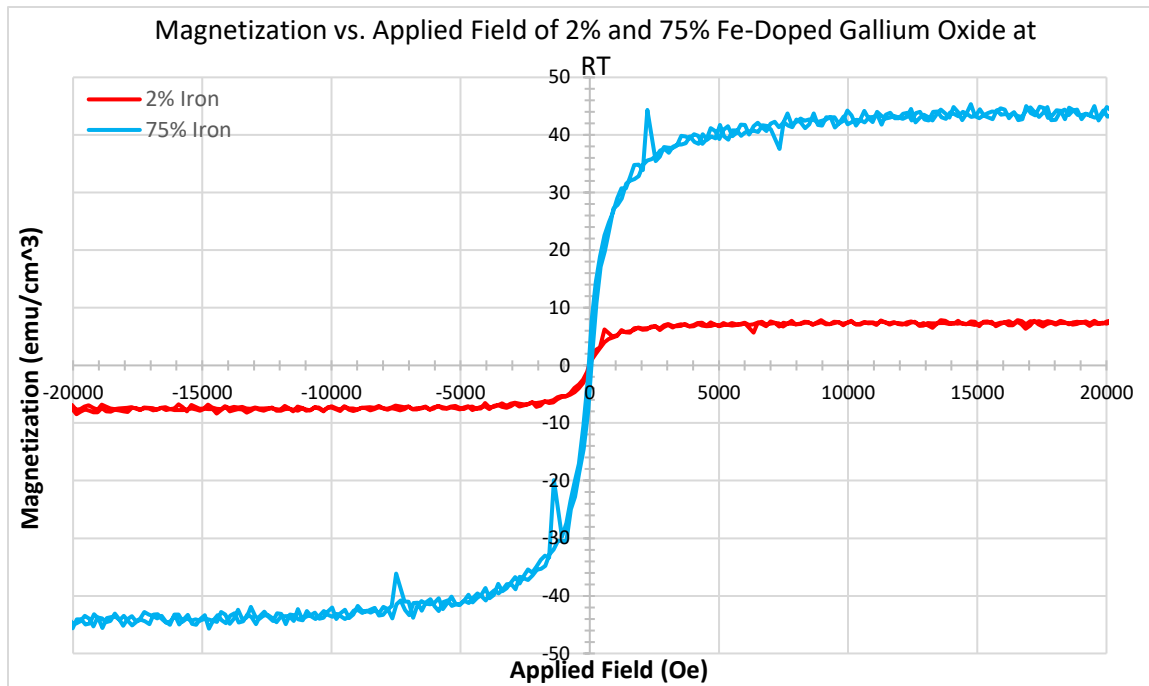


Figure 4.6. Magnetization vs. field curves for monoclinic $\beta\text{-Ga}_2\text{O}_3$ thin films with Fe-concentrations of 2% and 75% displaying ferromagnetic behavior.

Ferromagnetic behavior is characterized by a large net magnetization at low applied magnetic fields, known as the saturation field, accompanied by a large positive susceptibility due to the alignment of the spins within the magnetic domains of the material once exposed to an external magnetic force [77]. Looking to figure 4.6, there is a clear distinction between the saturation fields and the magnetization of 2% and 75% Fe-doped gallium oxide. The thin film composed of 2% Fe exhibits ferromagnetic behavior, as the sample quickly saturates at around 2,500 Oe and yielding a small magnetization

value at approximately 7 emu/cm^3 . However, the 75% Fe-doped Ga_2O_3 thin film displays a much larger net magnetization, over 6 times larger than that of the 2% Fe-doped Ga_2O_3 thin film but takes a slightly larger applied field to saturate the sample: approximately 7,000 Oe. Regardless, for both $(\text{Ga}_{1-x}\text{Fe}_x)_2\text{O}_3$ samples where $x=0.75$ and 0.02 , there is quick saturation at small, applied fields with a large magnetization observed for $x=0.75$. The largest magnetic moment per unit volume for the 75% Fe doped sample suggests that the magnetic dipole is located on the iron atoms. This is most likely due to dipolar interactions of the thin films' domain walls moving to align their magnetic spins in the direction of the applied field [77, 78].

Paramagnetic materials also do not retain any net magnetization once the material is removed from the applied magnetic field, while ferromagnetic materials will exhibit hysteretic behavior and will have some magnetic dipoles still aligned in the direction of the field once the magnetic field is set back to zero, known as retentivity or a remanence point [77]. Looking closer to the curves of the 2% and 75% Fe-doped thin films in figure 4.7, there is retentivity for both the 2% and 75% samples, creating a hysteretic "loop," but is more prominently displayed for the 75% sample when the magnetic field is completely removed. These characteristics observed in both the lightly and heavily doped Ga_2O_3 thin films provide evidence of room temperature ferromagnetic behavior.

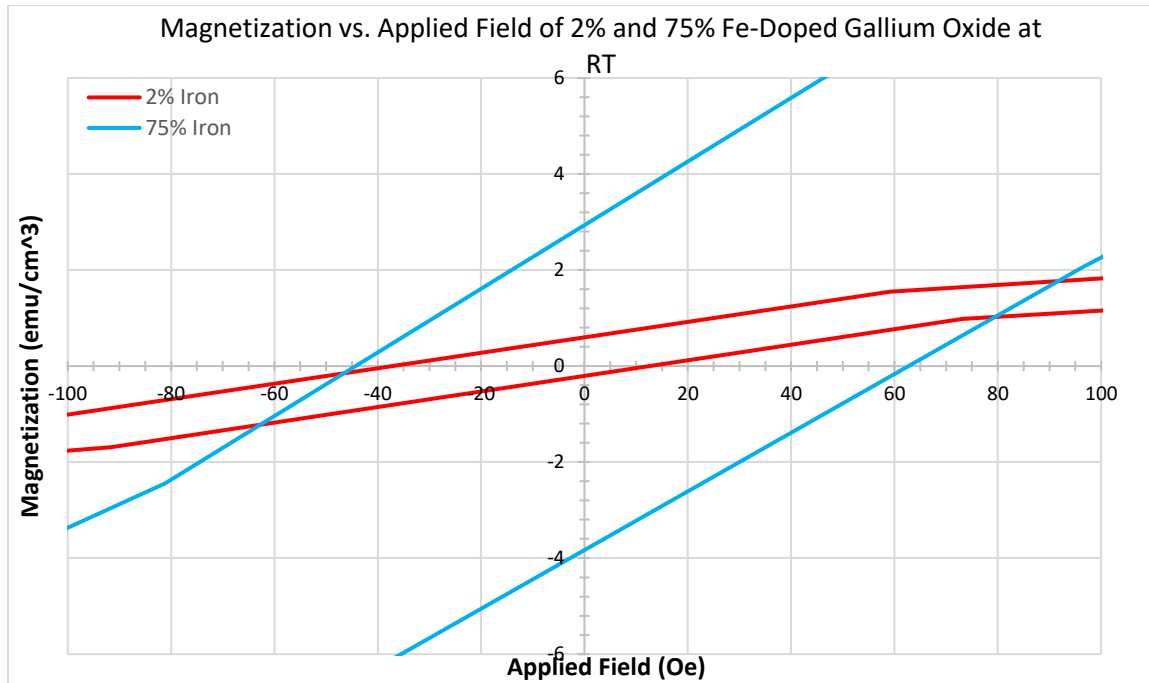


Figure 4.7. Zoomed in magnetization vs. field curves for 2% and 75% Fe-doped Ga_2O_3 displaying ferromagnetic retentivity and hysteretic behavior.

4.4.2 Iron Concentration Dependence

The next set of measurements were taken with the intent to observe the dependence of iron concentration on the magnetic properties of the Ga_2O_3 thin films. Note that the first set of hysteresis curves were not standardized to show the difference in magnetic moments per unit volume of the samples with varying Fe concentrations. The following plots show the saturation magnetization vs. magnetic field of each sample, first looking to the monoclinic and spinel cubic phases separately. The volumes of the measured samples were calculated using the dimensions listed in Table 6 above. All samples' room temperature magnetic moments were measured using the DynaCool PPMS VSM insert. A "moment vs. field" scan was taken for each sample at 300K, sweeping from -6T to 6T at a scan rate of 165 Oe/s. The samples were mounted on quartz rod holders using rubber cement.

Looking to figures 4.8 and 4.9 displaying the Fe-doped $(\text{Ga}_{1-x}\text{Fe}_x)_2\text{O}_3$ samples obtaining the monoclinic and spinel phase structures, the magnetic moment per unit volume increases with iron concentration for both phases, which is to be expected since the magnetic moment per unit volume should increase with increasing amount of Fe particles being substituted into the Ga_2O_3 lattice sites of both structures.

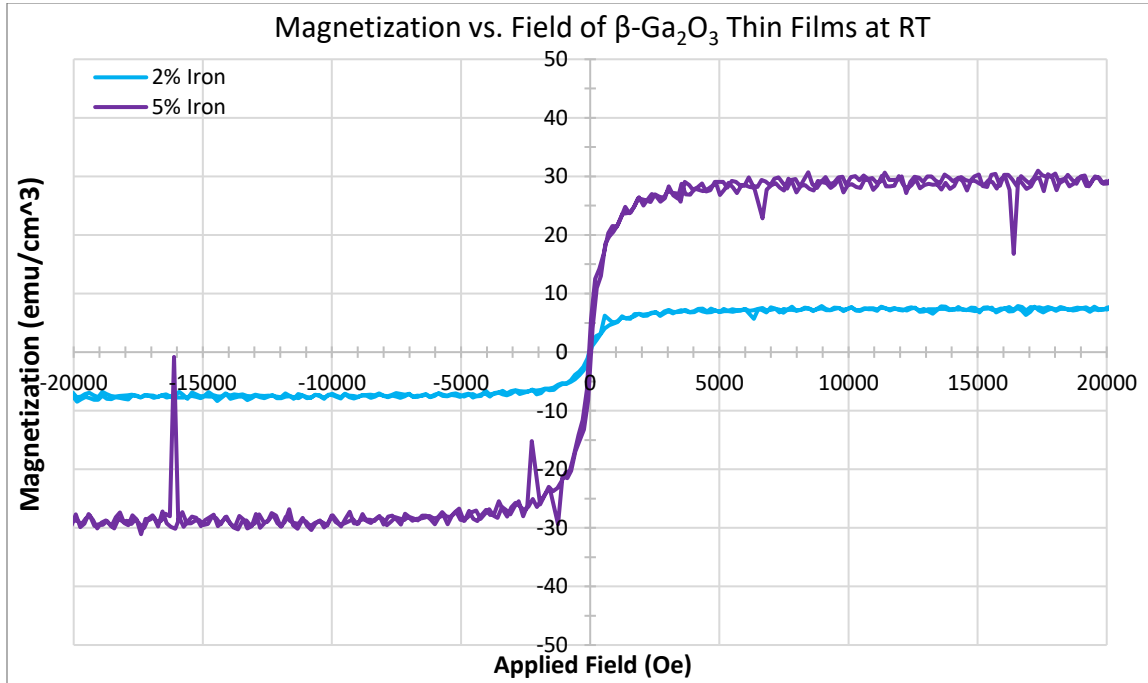


Figure 4.8. Magnetization vs. field curves for the monoclinic Ga_2O_3 structures with 2% iron and 5% iron.

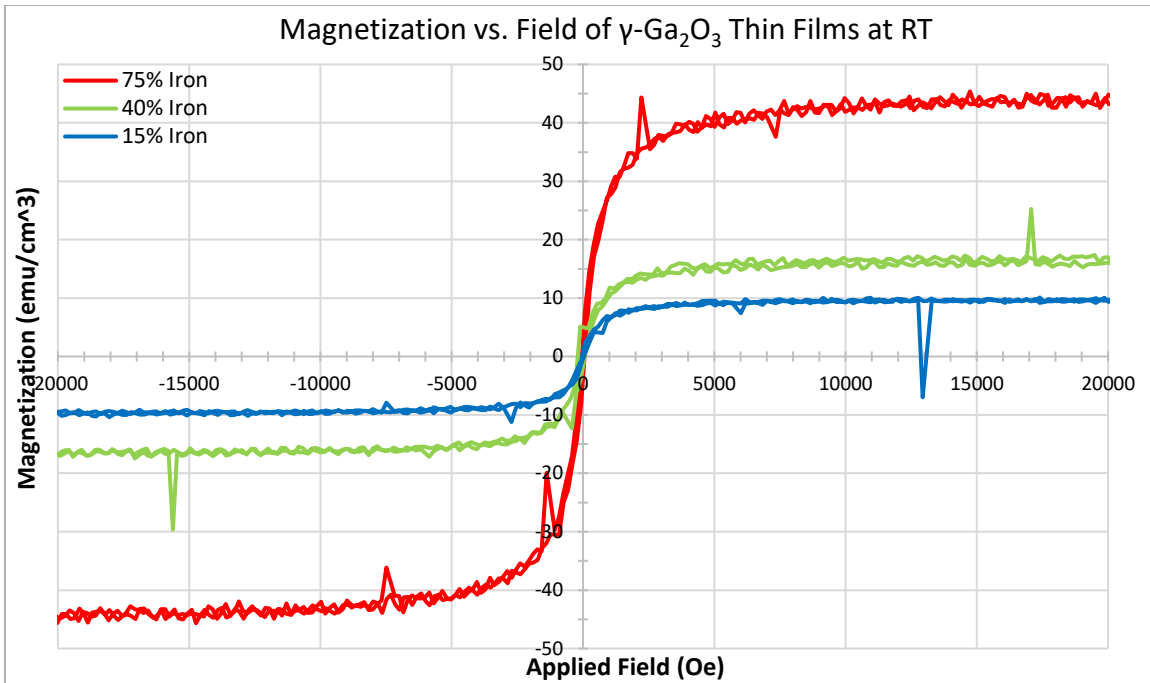


Figure 4.9. Hysteresis curves displaying the magnetic moment per unit volume vs. magnetic field for cubic spinel Ga_2O_3 structures of 15%, 40%, and 75% iron.

However, looking to the saturation magnetization “ M_s ” versus temperature curve in figure 4.10, it can be noted that the magnetization does not scale with iron concentration completely, as the 5% Fe sample is noticeably larger than that of the 40% and 15% Fe samples. This could be due to the large variation in volumes between the 5% sample and the 15% and 40% samples, but also suggests that the magnetic moment per Fe atom differs between the monoclinic and spinel cubic crystal phases. Ferromagnetic behavior was observed at room temperature for all $(\text{Ga}_{1-x}\text{Fe}_x)_2\text{O}_3$ samples of varying Fe ($x=0.02$ to 0.75) concentrations, giving confidence that the inclusion of transition metals such as iron into the gallium oxide crystal structures yields a net spontaneous magnetization for the thin films.

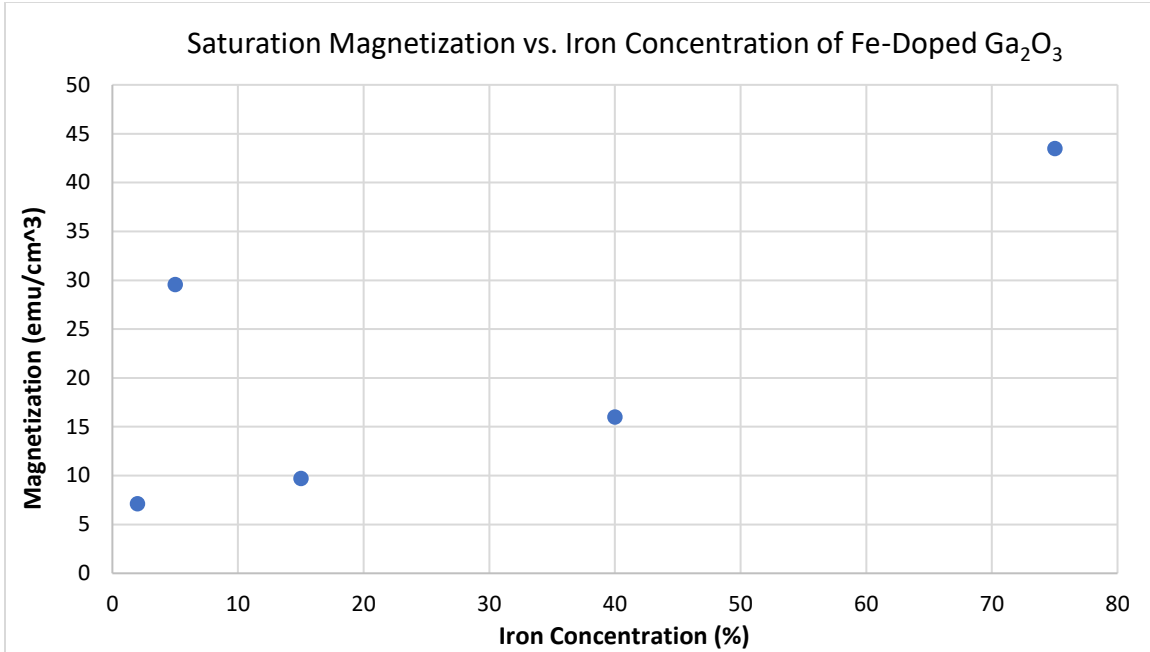


Figure 4.10. Saturation magnetization versus iron concentration for the Fe-doped Ga_2O_3 samples measured via PPMS VSM.

Looking to figure 4.11 showing the normalized hysteresis curves for each sample measured at room temperature, there is little variation in the trends for each concentration in terms of coercivity, however the saturation field seemed to have an inverse relationship with iron concentration. The inset of figure 4.11 displays a closer view of the susceptibility for the gallium oxide samples and showed a slightly higher susceptibility for the cubic spinel phases of 2% and 5% Fe, suggesting the lower concentrated samples were magnetized easier than the higher doped thin films. The higher susceptibility could be due in part to the lower number of interstitial defects present in the crystal lattice for the lighter doped samples compared to the more heavily doped samples [77, 79].

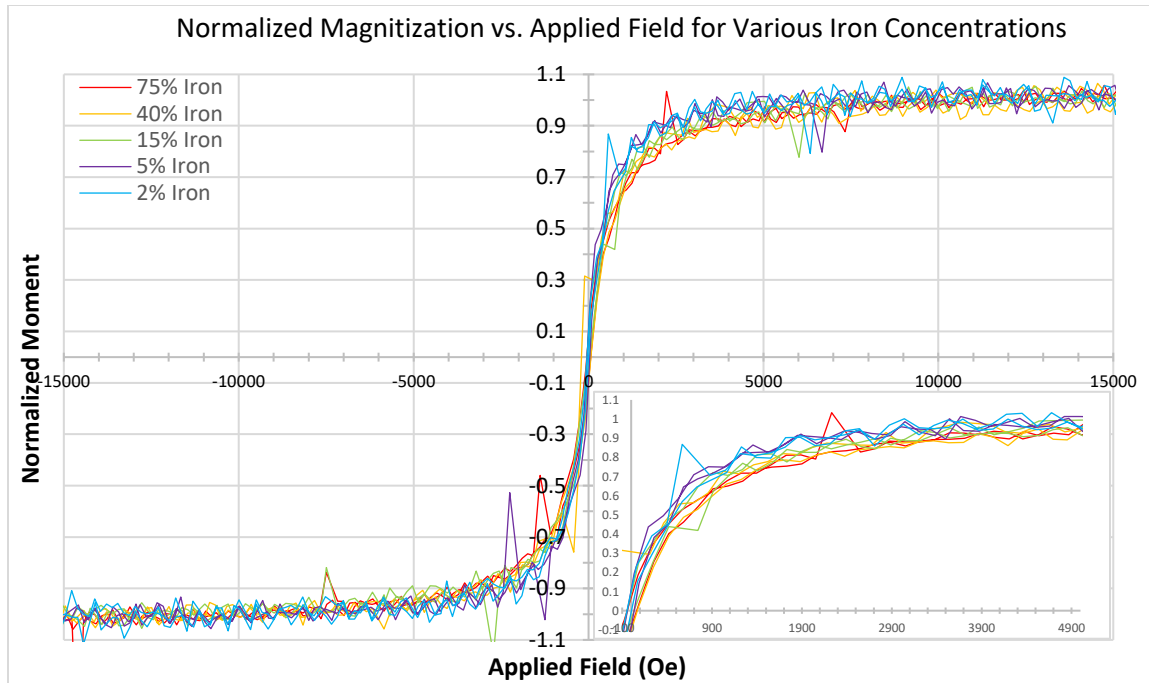


Figure 4.11. Normalized hysteresis curves of all five Fe-doped Ga_2O_3 samples taken at RT via PPMS VSM.

The magnetic characteristics for the set of gallium oxide samples were estimated from the above hysteresis plots to further examine the dependence on iron concentration. The following table displays the coercivity, remanence, and saturation magnetization, for each sample measured at room temperature. These values were extracted from the hysteresis measurements taken using the PPMS VSM. For the coercivity and remanence values, the absolute values from both sweep directions (one from 6T to -6T and one from -6T to 6T) were estimated about the x- and y-intersections and then averaged. It should be noted that the high % uncertainty for some samples was due to the asymmetric curves about the origin. In particular, the hysteresis curve for the 2% iron sample did not have a symmetric hysteresis curve, having one sweep from 6T to -6T being shifted and therefore causing a higher uncertainty in the average coercivity and remanence values.

Table 7. Estimated RT magnetic properties for Fe-doped Ga₂O₃ samples of 2%, 5%, 15%, 40% and 75%. Values were estimated from the corresponding hysteresis curves taken on the PPMS VSM.

	Spinel Cubic			Monoclinic	
Iron Concentration (%)	75	40	15	5	2
Saturation Magnetization M_s (emu/cm³)	43.48 ± 2%	15.99 ± 2%	9.71 ± 2%	29.56 ± 2%	7.14 ± 4%
Coercivity H_c (Oe)	52 ± 19%	54.5 ± 27%	38 ± 5%	37.3 ± 8%	24.88 ± 50%
Remanence M_r (emu/cm³)	3.4 ± 13%	1.25 ± 38%	0.62 ± 26%	2.77 ± 7%	0.398 ± 49%

Note that this table also indicates that the magnetic moment per unit volume for the 5% Fe sample is noticeably higher than that of the 15% and 40% samples, again suggesting an effect of the crystal structure on the magnetic dipole moment per Fe atom, as well as the degree of magnetic ordering. This could also be due to the thickness variation of the thin films as mentioned above. The saturated magnetization is defined by the following equation [77]:

$$M_s = \frac{m}{V} = \frac{m}{A \cdot t} \quad 4.1$$

Where “m” is the measured magnetic moment, “V” is the sample’s volume which can be rewritten in terms of the sample’s surface area “A” and film thickness “t.” From this equation it is apparent that as the volume, the magnetization decreases, and vice versa. Looking back at Table 2, the volume of the 5% sample is much smaller than that of the 15% sample, and the area of the 5% sample is roughly half that of the 40% sample. So, errors on the estimated sample area of the 5% sample will lead to a larger error in the magnetization value for the 5% sample.

4.4.3 Temperature Dependence

Lastly, the temperature dependent measurements were taken on the 5% monoclinic and 75% spinel cubic Fe-doped Ga_2O_3 samples to explore the potential changes in magnetic properties such as the magnetic moment and coercivity with respect to temperature. A sweeping temperature scan ranging from 848 K down to 5 K was executed for the spinel cubic $(\text{Ga}_{1-x}\text{Fe}_x)_2\text{O}_3$ sample where $x=0.75$ and 798 K to 5 K was executed for the monoclinic $(\text{Ga}_{1-x}\text{Fe}_x)_2\text{O}_3$ sample where $x=0.05$.

Figure 4.12 shows the magnetization vs. temperature curve for the 5% monoclinic Fe-doped Ga_2O_3 thin film ranging from 5 K to 798 K using both the PPMS VSM insert and the MicroSense VSM. Moment vs. field measurements were taken at 300 K and 400 K on both systems and are in agreement with each other. From figure 4.12, the magnetization of the 5% monoclinic sample appears to be temperature dependent as the magnetization decreases with increasing temperature. The curve emulates a polynomial trendline as the magnetization approaches zero at high temperatures, which is characteristic of ferromagnetic behavior. Fitting the curve in figure 4.12 to a polynomial expression and extrapolating to the x-intercept would suggest a possible Curie temperature of around 946 K for this material.

However, the magnetization vs. temperature curve for the 75% spinel cubic sample heavily differs from that of the 5% sample. Figure 4.13 displays the magnetization vs. temperature curve for spinel cubic 75% Fe-doped gallium oxide, ranging from temperatures of 5 K to 848 K using both the PPMS VSM insert and the MicroSense VSM head. Moment vs. field measurements were taken at 300 K and 400 K on both systems

and agree with each other. From this curve, the magnetic signal of this film begins to descend linearly towards zero at 700 K, obtaining only approximately 9.56 emu/cm³ at 848 K. A second set of measurements was attempted starting at 900 K but yielded a destroyed sample with distorted color and no magnetic signal, giving some evidence that suggests the Curie temperature of this material is well below 900 K. The Curie temperature is the temperature threshold in which the magnetic domains within the material align in a ferromagnetic fashion below this threshold and above, the material loses its magnetic ordering and behaves as a paramagnet [77].

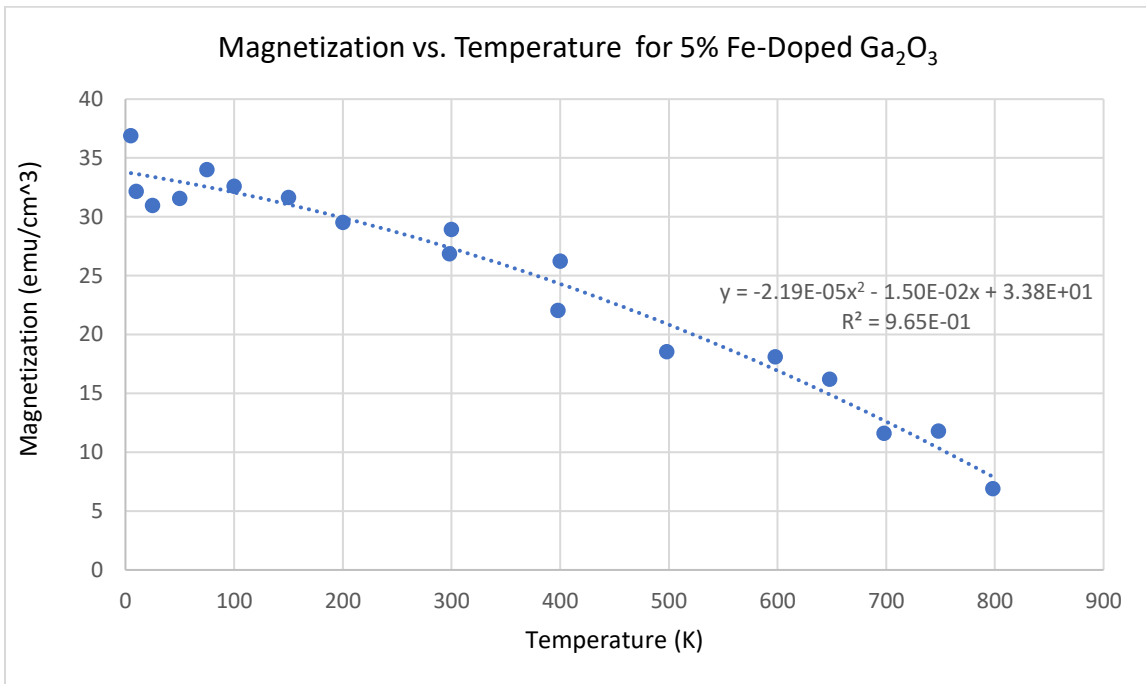


Figure 4.12. Magnetization vs. temperature curve for the 5% Fe-doped Ga₂O₃ sample at a temperature range of 5 K to 798 K.

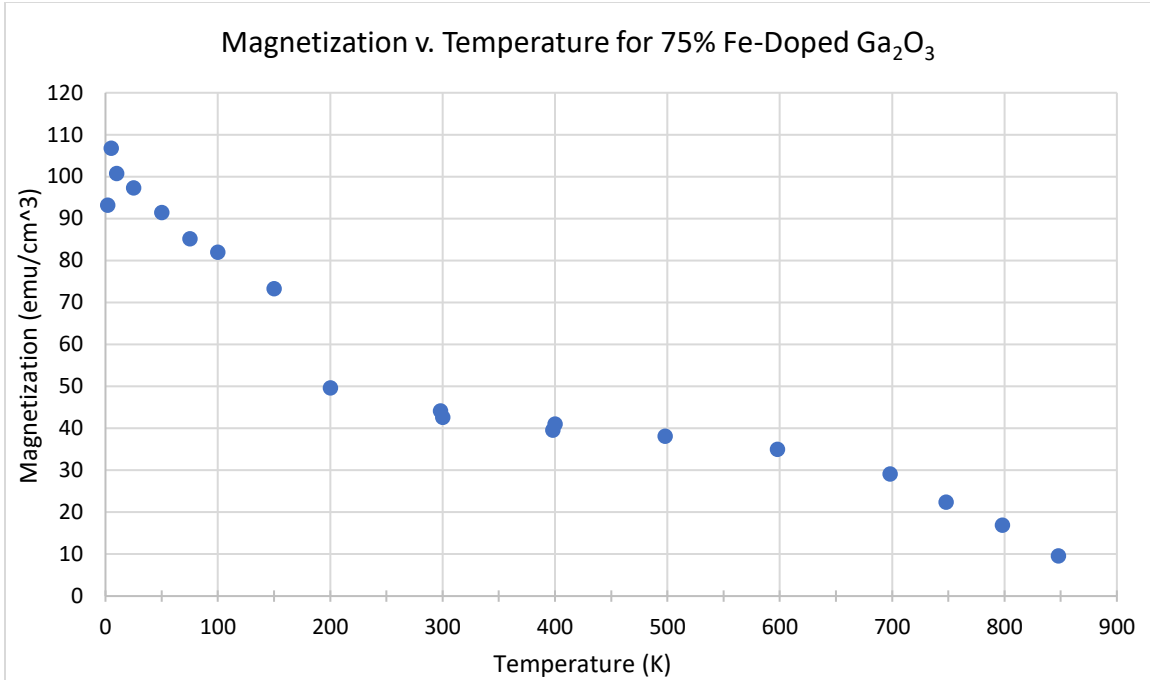


Figure 4.13. Magnetization vs. temperature curve for the 75% Fe-doped Ga₂O₃ sample at a temperature range of 5 K to 848 K.

The destruction of the sample within this temperature range was a surprising result, as various reports indicate a crystal phase transition from γ -Ga₂O₃ to the stable phase β -Ga₂O₃ anywhere from 873 K to 973 K (600° C to 700° C) [80, 81]. Furthermore, the magnetic ordering temperature for the Fe₂O₃ polymorphs having similar crystal structures, such as ferrimagnetic γ -Fe₂O₃, known as “maghemite,” theoretically occurs around 985 K, but is reported to transform to α -Fe₂O₃ at 800 K which is known to be antiferromagnetic [55, 82]. While the 75% Fe-doped Ga₂O₃ is clearly not antiferromagnetic, the ferrimagnetic γ -Fe₂O₃ holds the same defective cubic spinel crystal structure that this thin film is reported to have, suggesting that the magnetic ordering of the metal ions in this thin film could be similar to that of γ -Fe₂O₃ [14, 55].

Looking to figure 4.13 again, there is also an observed decrease in magnetization at low temperatures as well as a sharp drop after 150 K, suggesting another transition occurring

at low temperatures for this material which was not observed for the 5% monoclinic Fe-doped Ga_2O_3 sample in figure 4.12. To further inspect this, the normalized magnetization vs. moment curves at low temperatures are shown in figure 4.14. These curves show drastic changes in the susceptibility and coercivity at low temperatures of 25 K, 10 K and 5 K compared to room temperature, with the curve taken at 5 K requiring a saturation field of 30,000 Oe to magnetize the sample. Recall from figure 4.6 that the same sample only required a field of 7,000 Oe to saturate when measured at room temperature. While it is expected that a higher field is needed to saturate the sample at lower temperatures, this increase is more than 4 times larger than the saturation at room temperature, suggesting that the material changes magnetic properties at lower temperatures.

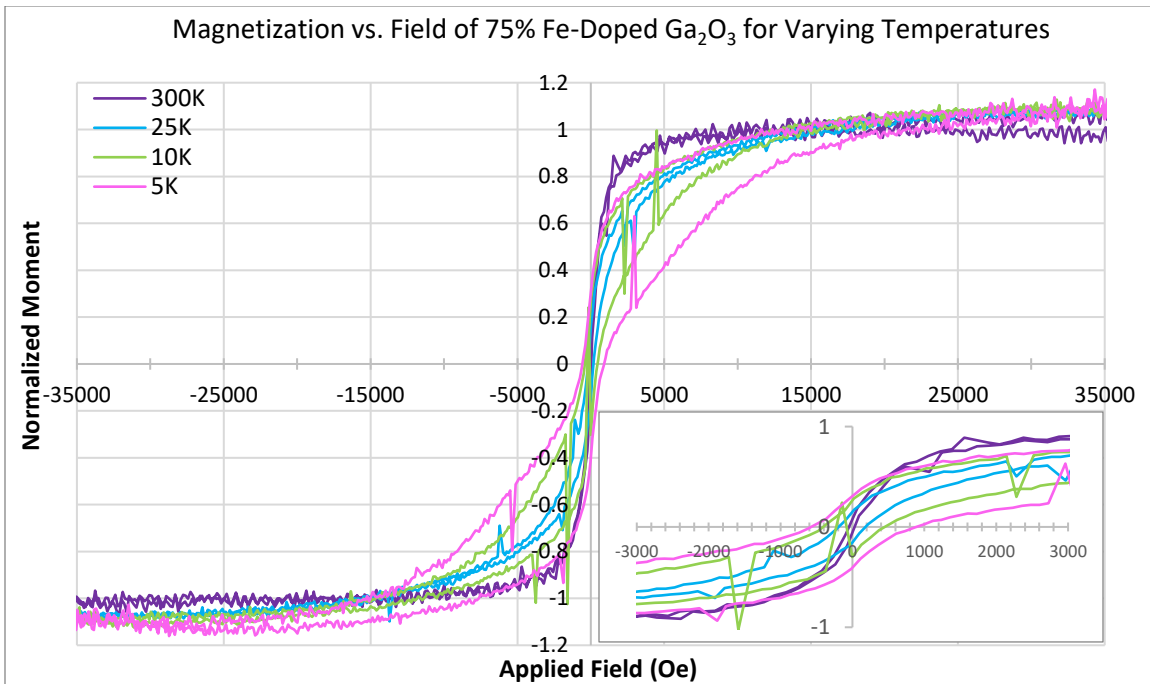


Figure 4.14. Normalized hysteresis curves of 75% Fe-doped Ga_2O_3 displaying the change in magnetic behavior at room temperature compared to lower temperatures.

Table 8 shows the estimated coercivity, remanence, and saturation magnetization values for the 5% and 75% iron samples at select temperatures taken from the hysteresis curves above. The increase in coercive fields from 400 K to 5 K for the 75% Fe-doped sample

increases by more than an order of magnitude, with the saturation magnetization following the same trend.

Table 8. Magnetic properties retrieved from the hysteresis curves of the 5% and 75% Fe-doped Ga₂O₃ at room temperature versus low temperatures. All curves were taken using the PPMS VSM.

5% Iron					
Temperature (K)	300	150	25	10	5
Saturation Magnetization M_s (emu/cm³)	29.56 ± 2%	31.89 ± 3%	31.18 ± 1%	32.14 ± 2%	36.89 ± 3%
Coercivity H_c (Oe)	37.3 ± 8%	51.5 ± 10%	68.05 ± 13%	118.25 ± 8%	122.85 ± 5%
Remanence M_r (emu/cm³)	2.77 ± 7%	3.1 ± 3%	5.2 ± 10%	4.33 ± 42%	6.82 ± 2%
75% Iron					
Temperature (K)	300	150	25	10	5
Saturation Magnetization M_s (emu/cm³)	43.48 ± 2%	67.89 ± 5%	98.42 ± 2%	100.58 ± 1%	101.92 ± 2%
Coercivity H_c (Oe)	52 ± 19%	40.15 ± 5%	187.25 ± 1%	426.5 ± 1%	697.25 ± 4%
Remanence M_r (emu/cm³)	3.4 ± 13%	3.09 ± 1%	14.08 ± 2%	25.88 ± 3%	32.68 ± 1%

With the possibility of a low temperature transition occurring at the higher doped sample, comparisons of the magnetic properties observed in this thesis were made with ferrimagnetic materials γ -Fe₂O₃, known as maghemite and Fe₃O₄, known as magnetite. Magnetite is reported to have an inverse spinel cubic crystal structure due to the inclusion of both Fe³⁺ and Fe²⁺ present in the crystal structure, the only difference from normal

spinel cubic being that instead of all the Fe^{3+} ions residing in the octahedral sublattice sites, they are now evenly split between the octahedral and tetrahedral sites, with the Fe^{2+} ions occupying the remaining octahedral sites [55, 77, 83]. Maghemite, i.e. $\gamma\text{-Fe}_2\text{O}_3$ has a crystal structure that is set up very similarly, but instead of divalent ions, there are vacancies at these octahedral sites [55, 68]. For the 75% Fe-doped Ga_2O_3 structure, Mia reported via XPS measurements the presence of Fe^{3+} and Fe^{2+} in the crystal lattice and a ratio of $\text{Fe}^{3+}:\text{Fe}^{2+}$ being 1.95 for 15% iron and 1.48 for 75% iron, suggesting an increasing presence of Fe^{2+} ions as more iron was introduced into the Ga_2O_3 structure [14]. This evidence further backs up the suspicion that the 75% Fe-doped Ga_2O_3 thin film could be mimicking magnetic behavior of magnetite or maghemite.

Magnetite also has a much lower Curie temperature compared to maghemite, losing its magnetic ordering around 858 K to 860 K [55], which is very close to the last measurement taken of 75% Fe-doped Ga_2O_3 at 848 K before the sample lost signal at 900 K. Not only this, but magnetite has the unique characteristic of a second phase transition, known as the Verwey transition, occurring around 120 K where the ferrimagnetic sample behaves as an insulator and relaxes to a monoclinic crystal phase [55]. For the 75% iron sample, there was a steep drop in magnetization from 150 K to 200 K, close in range to the low temperature transition reported for magnetite, again suggesting that this heavily doped Ga_2O_3 sample could have a unique low temperature transition similar to that of a Verwey transition. Such a transition could also possibly explain the increase in applied external field required to saturate the sample at low temperatures.

Furthermore, Mia reported in his work increasing lattice parameters as the iron concentration increased due to the increasing atomic radii of Fe^{3+} and Fe^{2+} (0.64 Å and

0.72 Å respectively) versus that of Ga³⁺ (0.62 Å) and revealed a calculated lattice parameter for the 75% iron sample of 8.3086 Å via XRD measurements [14]. Magnetite is reported to have a lattice parameter of 8.39 Å to 8.4 Å [55, 68, 83, 84], and reports on maghemite show a lattice parameter of around 8.34 Å to 8.35 Å [55, 68, 85]. The lower lattice parameter for the Ga₂O₃ sample is consistent with the fact that Ga³⁺ ions are smaller than Fe ions, and since 25% of the metal ions in the crystal structure are still Ga³⁺, it is expected that the distance between nearest neighbors will be smaller compared to the pure iron oxide structures. Nonetheless, the similarities between these two iron oxide structures and the 75% Fe-doped Ga₂O₃ thin film in terms of transition temperatures, magnetic ordering temperatures, lattice parameters, and crystal structures strongly suggest that at this high of an iron doping concentration, the Fe-doped Ga₂O₃ thin film could be mimicking ferrimagnetic behavior, rather than ferromagnetic behavior as previously reported [73, 76, 86, 87]. It should be noted that these previous reports on Fe-doped Ga₂O₃ are for room temperature measurements and doping concentrations no larger than 30% Fe.

To find the Curie temperature of this material and thus confirm the true magnetic behavior, the specific sublattice site locations of the various metal cations (Ga³⁺, Fe³⁺, Fe²⁺) need to be determined through a theoretical method such as density functional theory (DFT) calculations. DFT is an *ab initio* many-body theory that takes into account all interactions between all of the electrons present [77]. This determination would allow one to express the superexchange interactions occurring through the metal-oxide-metal bonds of this spinel structure by a Heisenberg Hamiltonian (which will be changed to ‘ ϵ ’ here so as to not confuse with applied field ‘H’) [77, 78]:

$$\varepsilon_{exchange} = -\sum_{ij} J_{ij} \bar{S}_i \bar{S}_j \quad 4.2$$

Where “ J_{ij} ” is the exchange coupling integral arising from the overlap of two electrons’ wavefunctions, and “ \bar{S}_i ” and “ \bar{S}_j ” are the respective spin momentums on arbitrary electrons “i” and “j.” Once the exchange interactions between nearest neighbors can be determined, the type of magnetism can be confirmed through the sign of the exchange integral. A positive exchange integral indicates the spins will favor parallel alignment and thus exhibit ferromagnetic behavior, whereas a negative exchange integral will exhibit antiferromagnetic behavior, as the spins will favor antiparallel alignment.

For example, in the case of this thesis, if it is determined that the Fe^{2+} ions detected in the 75% iron sample are found to reside at the octahedral sites and the Fe^{3+} ions found to be evenly distributed to tetrahedral and octahedral sites, then this material can be treated similarly to a spinel cubic ferrimagnetic material. This would mean that Fe^{3+} ions located at the octahedral sites are aligned antiparallel to the Fe^{3+} ions located at the tetrahedral sites, exhibiting a negative exchange interaction for antiferromagnetic behavior, and therefore cancelling each other out. This would then mean the exchange interaction between the octahedral sites containing Fe^{2+} ions would be aligned parallel to each other and exhibit ferromagnetic behavior, thus yielding a magnetic moment contribution coming only from the Fe^{2+} ions.

The final step would be to then calculate the Curie temperature of this material, which can be achieved by implementing the Weiss molecular field theory once the exchange integrals and type of magnetism are known [77]. The molecular field theory describes the magnetic behavior between localized moments and the corresponding molecular fields

that act on the ions at given lattice sites [77, 88]. The molecular field theory can be used to find the appropriate magnetizations “ M_A ” and “ M_B ” acting on each sublattice for either ferromagnetic or ferrimagnetic behavior, and thus used to solve for the Curie temperature “ T_c ” [55, 77]. This method was carried out by Wu et. al to calculate the exchange interactions and then the Curie temperature by means of DFT calculations, the Heisenberg model, and molecular field approximations (MFA) for doped barium hexaferrites and found that the calculated Curie temperature agreed well with experimental values [89].

5: CONCLUSION & SUGGESTIONS FOR FUTURE WORK

To summarize, the work of this thesis consisted of magnetic characterization on two different materials: soft magnetic Fe/PLA filaments 3-D printed using MFAAM and single crystalline epitaxial Fe-doped Ga₂O₃ thin films of various Fe concentrations. The Fe/PLA filaments were printed on top of permanent magnets to supply different external magnetic field strengths during the printing process, a modification from regular AM coined MFAAM. These various filaments were then measured using a MicroSense VSM to observe magnetic field dependence as well as field angle dependence on the magnetic properties and determine any potential anisotropy. The filaments were also characterized by digital microscopy and XRD to further confirm the results from the VSM. This work was done in support of a research enhancement grant of Texas State University “Materials with intelligence: Magnetic Field Assisted Additive Manufacturing” (Geerts, Tate, Chen).

The Fe-doped Ga₂O₃ thin films were grown by Dr. Dalim Mia using pulsed laser deposition (PLD). Films with different iron concentrations (2%, 5%, 15%, 40%, and 75%) and two different crystal structures were investigated. These films were then measured using both the MicroSense VSM and the QuantumDesign PPMS VSM to observe magnetic field dependence, temperature dependence, and iron concentration dependence. The samples’ hysteresis curves were inspected and magnetic properties such as saturation magnetization, coercivity, and remanence were estimated and compared. The magnetization with respect to temperature was also investigated for the 5% and 75% Fe-doped samples. This work was done in support of the DOD HBCI/MI grant W911NF-

20-1-0298 “Ultrawide Bandgap Hetero-structures: Growth Characterization and Modeling” (Droopad, Geerts, Scolfaro).

5.1 Fe/PLA 3-D Printed Filaments

5.1.1 Conclusions

MFAAM showed appreciable effects on the Fe/PLA samples that were printed in different magnetic field strengths compared to the zero-field control sample. Through VSM angle-dependent measurements, shape anisotropy of the samples was observed by angle dependency and the demagnetizing field effect was observed to be greatest along the samples' shortest radial axes. This was observed for all three samples. Furthermore, the susceptibility of the MFAAM samples compared to the control sample in identical measurement directions increased by a factor of 2 and 2.5 for the 5 kOe transverse sample and the 8 kOe parallel sample, respectively. This increase in susceptibility was found to be caused by slight induced crystallographic texture along the easy axis of magnetization, measured via XRD scans. Chaining aggregates were also observed in both samples in the direction of their respective print field through optical digital microscopy, which is also believed to have enhanced the susceptibility when measured along the print field direction.

5.1.2 Suggestions for Future Work

Suggestions for future research on MFAAM filaments with soft magnetic material could be to attempt printing magnetic devices such as transformer cores, as done previously, to observe if the efficiency increases compared to that of commercial transformer cores.

Prior studies done report successful printing of transformer cores via AM, but lack of efficiency and ease of magnetic saturation did not allow them to be viable options in replacement of commercial transformer cores. This thesis confirmed that MFAAM enhances the susceptibility when the external field is applied in the direction of the print field, so it could be beneficial to print a transformer core using the MFAAM soft magnetic filaments to observe any enhancements in these reported setbacks. In order to be able to easily print complex geometrical prototypes in a magnetic field, the 3-D printer needs to be furnished with an electromagnet or a set of nested Halbach cylinders so a magnetic field can be applied to the printed material before it solidifies.

5.2 Fe-Doped Ga₂O₃ Thin Films

5.2.1 Conclusions

All Fe-doped Ga₂O₃ thin films were observed to behave ferromagnetically when measured at room temperature. Ferromagnetic characteristics such as significant magnetization values, remanence and large susceptibility were observed at room temperature for the Fe-doped Ga₂O₃ samples of iron concentrations of 2%, 5%, 15%, 40% and 75%. These findings are consistent with previous studies done on β -Ga₂O₃ and γ -Ga₂O₃ phases of lower iron concentrations. The thin films' magnetic properties did not show drastic changes in terms of remanence or coercivity as the iron concentration increased, however the magnetic moment per unit volume seemed to scale up with iron concentration. The magnetic behavior is different for the monoclinic and gamma phases. The lower concentrated samples (2% and 5%) exhibited higher susceptibility compared

to the heavier doped samples, suspected to be from a lower number of defects within the crystal lattice making it easier to saturate.

The magnetization as a function of temperature was determined for the 5% and 75% Fe-doped Ga₂O₃ sample and suggested a Curie temperature within the range of 848 K to 900 K for the 75% sample based on experimental results. A small ferromagnetic signal was still detected at 848 K but upon attempted measurements at 900 K, the sample yielded no magnetic signal. Further observing the hysteresis curves at low temperatures, the magnetic properties such as saturation magnetization and coercivity were observed to heavily increase with decreasing temperature, as well as the saturation field increasing to 30,000 Oe at 5 K from approximately 7,000 Oe when measured at room temperature. The magnetization vs. temperature graph also suggested another phase transition occurring around 150 K to 200 K which was characterized by a steep drop in magnetization going from 150 K to 200 K. Similar experiments conducted on the monoclinic 5% Fe-doped Ga₂O₃ sample did not show this low temperature transition, therefore confirming this a characteristic for the γ -phase Ga₂O₃. This behavior could be comparable to the iron oxide magnetite's Verwey transition temperature taking place around 120 K.

Looking back at the dissertation of Mia, he reported an increasing presence of Fe²⁺ ions in addition to Fe³⁺ ions as the doping concentration increased, as well as increased lattice parameters with increased iron concentration. The ferrimagnetic iron oxides magnetite and maghemite were both researched to observe their magnetic properties and were compared to the 75% Fe-doped Ga₂O₃ sample to observe any similarities. Both iron oxides were found to have spinel cubic crystal structures such as the 75% iron sample, with magnetite obtaining the inverse spinel structure due to the presence of both Fe³⁺ and

Fe^{2+} ions in the sublattice sites. The reported Curie temperature of magnetite is very close (858 K) to the last measured signal for the 75% Fe sample (848 K) and is also reported to have a lattice parameter just a few tenths of an angstrom larger than what was reported by Mia et al. for 75% Fe. Given the vast similarities in magnetic properties between the 75% Fe-doped Ga_2O_3 and iron oxide magnetite, these findings suggest that at this high of a doping concentration, the heavier doped Ga_2O_3 thin films could be exhibiting ferrimagnetic behavior similar to magnetite, rather than ferromagnetic behavior.

5.2.2 Suggestions for Future Work

Full temperature range hysteresis curves should be conducted on the lower doped Ga_2O_3 thin films to determine the Fe concentration range for which the low temperature transition is observed. Suggestions for future work on the 75% iron doped Ga_2O_3 films include running density functional theory (DFT) calculations to determine the locations of the Fe^{3+} and Fe^{2+} ions within the sublattice sites, thus allowing confirmation of either ferromagnetic or antiferromagnetic ordering based on the type of exchange energy occurring between nearest neighbors and therefore determining whether ferrimagnetism or ferromagnetism is prevalent. Torque measurements should also be conducted to determine the magnetic anisotropy for each crystal phase and further characterize the Fe-doped thin films.

REFERENCES

- [1] Khatri, B., Lappe, K., Noetzel, D., Pursche, K., & Hanemann, T. (2018). A 3D-Printable Polymer-Metal Soft-Magnetic Functional Composite—Development and Characterization. *Materials*, *11*(2), 189. <https://doi.org/10.3390/ma11020189>
- [2] Huber, C., Abert, C., Bruckner, F., Groenefeld, M., Muthsam, O., Schuschnigg, S., Sirak, K., Thanhoffer, R., Teliban, I., Vogler, C., Windl, R., & Suess, D. (2016). 3D print of polymer bonded rare-earth magnets, and 3D magnetic field scanning with an end-user 3D printer. *Applied Physics Letters*, *109*(16). <https://doi.org/10.1063/1.4964856>
- [3] Tiismus, H., Kallaste, A., Belahcen, A., Rassolkin, A., Vaimann, T., & Shams Ghahfarokhi, P. (2021). Additive Manufacturing and Performance of E-Type Transformer Core. *Energies* *14*(11). <https://doi.org/10.3390/en14113278>
- [4] GE Additive. (n.d.). *What is Additive Manufacturing*. Retrieved February 28, 2022, from <https://www.ge.com/additive/additive-manufacturing>
- [5] Belduque, M. C. (2021). *DEVELOPMENT OF STRONTIUM FERRITE/POLYAMIDE 12 COMPOSITES FOR MAGNETIC DEVICES USING ADDITIVE MANUFACTURING* (Master's Dissertation).
- [6] Jessen, G. (2021, March 24). *Gallium Oxide: The Supercharged Semiconductor*. IEEE Spectrum. Retrieved March 10, 2022, from <https://spectrum.ieee.org/gallium-oxide-the-supercharged-semiconductor>
- [7] Pearton, S. J., Yang, J., Cary, P. H., Ren, F., Kim, J., Tadjer, M. J., & Mastro, M. A. (2018). A review of Ga₂O₃ materials, processing, and devices. *Applied Physics Reviews*, *5*(1). <https://doi.org/10.1063/1.5006941>
- [8] Vllora, E. G., Shimamura, K., Yoshikawa, Y., Ujiie, T., & Aoki, K. (2008). Electrical conductivity and carrier concentration control in β -Ga₂O₃ by Si doping. *Applied Physics Letters*, *92*(20). <https://doi.org/10.1063/1.2919728>
- [9] Zhou, W., Xia, C., Sai, Q., & Zhang, H. (2017). Controlling n-type conductivity of β -Ga₂O₃ by Nb doping. *Applied Physics Letters*, *111*(24). <https://doi.org/10.1063/1.4994263>
- [10] Tanaka, M. (2020). Recent progress in ferromagnetic semiconductors and spintronics devices. *Japanese Journal of Applied Physics*, *60*(1). <https://doi.org/10.35848/1347-4065/abcadc>
- [11] Ando, K. (2006). Seeking Room-Temperature Ferromagnetic Semiconductors. *Science*, *312*(5782), 1883–1885. <https://doi.org/10.1126/science.1125461>
- [12] Kammermeier, T. (2010). Structural and magnetic investigation of dilute magnetic semiconductors based on GaN and ZnO.
- [13] Ueda, K., Tabata, H., & Kawai, T. (2001). Magnetic and electric properties of transition metal-doped ZnO films. *Applied Physics Letters*, *79*(7), 988–990. <https://doi.org/10.1063/1.1384478>

- [14] Mia, M. D. (2020). *Growth and characterization of Ga₂O₃, (Ga_{1-x}Gdx)₂O₃ & (Ga_{1-x}Fex)₂O₃ thin films by pulsed laser deposition (Dissertation).*
- [15] *When Was 3D Printing Invented? The History of 3D Printing.* (2021, December 10). BCN3D Technologies. Retrieved March 23, 2022, from <https://www.bcn3d.com/the-history-of-3d-printing-when-was-3d-printing-invented/>
- [16] MakerBot 3D Printing. (2020, June 24). *The History of 3D Printing.* MakerBot. Retrieved March 23, 2022, from <https://www.makerbot.com/stories/engineering/history-of-3d-printing/>
- [17] *What Materials Are Used for 3D Printing?* (2018, April 17). Sharretts Plating Company. Retrieved March 23, 2022, from <https://www.sharrettsplating.com/blog/materials-used-3d-printing/>
- [18] Marr, B. (2021, December 10). *What Can 3D Printing Be Used For? Here Are 10 Amazing Examples.* Forbes. Retrieved March 23, 2022, from <https://www.forbes.com/sites/bernardmarr/2020/07/24/what-can-3d-printing-be-used-for-here-are-10-amazing-examples/?sh=322c105c4d69>
- [19] Bollig, L. M., Hilpisch, P. J., Mowry, G. S., & Nelson-Cheeseman, B. B. (2017). 3D printed magnetic polymer composite transformers. *Journal of Magnetism and Magnetic Materials*, 442, 97–101. <https://doi.org/10.1016/j.jmmm.2017.06.070>
- [20] Vázquez, M., & Hernando, A. (1996). A soft magnetic wire for sensor applications. *Journal of Physics D: Applied Physics*, 29(4), 939–949. <https://doi.org/10.1088/00223727/29/4/001>
- [21] Palmero, E. M., Casaleiz, D., Jimenez, N. A., Rial, J., de Vicente, J., Nieto, A., Altimira, R., & Bollero, A. (2019). Magnetic-Polymer Composites for Bonding and 3D Printing of Permanent Magnets. *IEEE Transactions on Magnetics*, 55(2), 1–4. <https://doi.org/10.1109/tmag.2018.2863560>
- [22] Huber, C., Cano, S., Teliban, I., Schuschnigg, S., Groenefeld, M., & Suess, D. (2020). Polymer-bonded anisotropic SrFe₁₂O₁₉ filaments for fused filament fabrication. *Journal of Applied Physics*, 127(6). <https://doi.org/10.1063/1.5139493>
- [24] Sarkar, A., Somashekara, M., Paranthaman, M. P., Kramer, M., Haase, C., & Nlebedim, I. C. (2020). Functionalizing magnet additive manufacturing with in-situ magnetic field source. *Additive Manufacturing*, 34. <https://doi.org/10.1016/j.addma.2020.101289>
- [25] de Oliveira Barros, A., Hasan Kashem, M. N., Luna, D., Geerts, W. J., Li, W., & Yang, J. (2022). Magnetic properties of PDMS embedded with strontium ferrite particles cured under different magnetic field configurations. *AIP Advances*, 12(3). <https://doi.org/10.1063/9.0000338>
- [26] Kim, Y., Yuk, H., Zhao, R., Chester, S. A., & Zhao, X. (2018). Printing ferromagnetic domains for untethered fast-transforming soft materials. *Nature*, 558(7709), 274–279. <https://doi.org/10.1038/s41586-018-0185-0>
- [27] Kim, J., Chung, S. E., Choi, S. E., Lee, H., Kim, J., & Kwon, S. (2011). Programming magnetic anisotropy in polymeric microactuators. *Nature Materials*, 10(10), 747–752. <https://doi.org/10.1038/nmat3090>

- [28] Tippins, H. H. (1965). Optical Absorption and Photoconductivity in the Band Edge of β -Ga₂O₃. *Physical Review*, 140(1A), A316–A319. <https://doi.org/10.1103/physrev.140.a316>
- [29] Rebien, M., Henrion, W., Hong, M., Mannaerts, J. P., & Fleischer, M. (2002). Optical properties of gallium oxide thin films. *Applied Physics Letters*, 81(2), 250–252. <https://doi.org/10.1063/1.1491613>
- [30] Stepanov, S.I., Nikolaev, V.I., Bougrov, V.E., & Romanov, A.E. (2016). GALLIUM OXIDE: PROPERTIES AND APPLICATIONS A REVIEW
- [31] *The Importance of SiC's Wide Bandgap* | *Wolfspeed*. (2019, November 23). Wolfspeed. Retrieved March 16, 2022, from <https://www.wolfspeed.com/knowledge-center/article/importance-of-silicon-carbide-wide-bandgap/>
- [32] *What is a wide-band-gap semiconductor?* | *Toshiba Electronic Devices & Storage Corporation | Americas – United States*. (n.d.). Toshiba. Retrieved March 16, 2022, from https://toshiba.semicon-storage.com/us/semiconductor/knowledge/faq/diode_sic-sbd/sic_sbd001.html
- [33] Pearton, S. J., Abernathy, C. R., Thaler, G. T., Frazier, R. M., Norton, D. P., Ren, F., Park, Y. D., Zavada, J. M., Buyanova, I. A., Chen, W. M., & Hebard, A. F. (2004). Wide bandgap GaN-based semiconductors for spintronics. *Journal of Physics: Condensed Matter*, 16(7), R209–R245. <https://doi.org/10.1088/0953-8984/16/7/r03>
- [34] Kamarulzaman, N., Kasim, M. F., & Rusdi, R. (2015). Band Gap Narrowing and Widening of ZnO Nanostructures and Doped Materials. *Nanoscale Research Letters*, 10(1). <https://doi.org/10.1186/s11671-015-1034-9>
- [35] Bayraktaroglu, B. & Air Force Research Laboratory, Sensors Directorate WPAFB United States. (2017b, August 1). *ASSESSMENT OF GALLIUM OXIDE TECHNOLOGY*. DTIC. <https://apps.dtic.mil/sti/citations/AD1038137>
- [36] Passlack, M., Schubert, E.F., Hobson, W.S., Hong, M., Moriya, N., Chu, S.N.G., *GA2O3 FILMS FOR ELECTRONIC AND OPTOELECTRONIC APPLICATIONS*.
- [37] Muller, R. S., Kamins, T., I., & Chan, M. (2002). *Device Electronics for Integrated Circuits* (3rd ed.). Wiley.
- [38] Ahmadi, E., Koksaldi, O. S., Kaun, S. W., Oshima, Y., Short, D. B., Mishra, U. K., & Speck, J. S. (2017). Ge doping of β -Ga₂O₃ films grown by plasma-assisted molecular beam epitaxy. *Applied Physics Express*, 10(4). <https://doi.org/10.7567/apex.10.041102>
- [39] Krishnamoorthy, S., Xia, Z., Bajaj, S., Brenner, M., & Rajan, S. (2017). Delta-doped β gallium oxide field-effect transistor. *Applied Physics Express*, 10(5). <https://doi.org/10.7567/apex.10.051102>
- [40] Zhang, J., Shi, J., Qi, D. C., Chen, L., & Zhang, K. H. L. (2020). Recent progress on the electronic structure, defect, and doping properties of Ga₂O₃. *APL Materials*, 8(2). <https://doi.org/10.1063/1.5142999>

- [41] Wong, M.H., Sasaki, K., Kuramata, A., Yamakoshi, S., and Higashiwaki, M., *Field-Plated Ga2O3 MOSFETs With a Breakdown Voltage of Over 750 V*, IEEE Electron Device Letters, vol. 37, no. 2, pp. 212-215, Feb. 2016, doi: 10.1109/LED.2015.2512279.
- [42] Lee, S. D., Akaiwa, K., & Fujita, S. (2013). Thermal stability of single crystalline alpha gallium oxide films on sapphire substrates. *Physica Status Solidi (c)*, 10(11), 1592–1595. <https://doi.org/10.1002/pssc.201300259>
- [43] Roy, R., Hill, V. G., & Osborn, E. F. (1952). Polymorphism of Ga2O3 and the System Ga2O3—H2O. *Journal of the American Chemical Society*, 74(3), 719–722. <https://doi.org/10.1021/ja01123a039>
- [44] Higashiwaki, M., Sasaki, K., Kuramata, A., Masui, T., & Yamakoshi, S. (2012). Gallium oxide (Ga2O3) metal-semiconductor field-effect transistors on single-crystal β -Ga2O3 (010) substrates. *Applied Physics Letters*, 100(1). <https://doi.org/10.1063/1.3674287>
- [45] Irmscher, K., Galazka, Z., Pietsch, M., Uecker, R., & Fornari, R. (2011). Electrical properties of β -Ga2O3 single crystals grown by the Czochralski method. *Journal of Applied Physics*, 110(6). <https://doi.org/10.1063/1.3642962>
- [46] García-Carrión, M., Ramírez-Castellanos, J., Nogales, E., Méndez, B., You, C. C., Karazhanov, S., & Marstein, E. S. (2020). Hybrid solar cells with β - and γ - gallium oxide nanoparticles. *Materials Letters*, 261. <https://doi.org/10.1016/j.matlet.2019.127088>
- [47] Huang, R., Hayashi, H., Oba, F., & Tanaka, I. (2007). Microstructure of Mn-doped γ Ga2O3 epitaxial film on sapphire (0001) with room temperature ferromagnetism. *Journal of Applied Physics*, 101(6). <https://doi.org/10.1063/1.2713349>
- [48] Huang, Y., Gao, A., Guo, D., Lu, X., Zhang, X., Huang, Y., Yu, J., Li, S., Li, P., & Tang, W. (2020). Fe doping-stabilized γ -Ga2O3 thin films with a high room temperature saturation magnetic moment. *Journal of Materials Chemistry C*, 8(2), 536–542. <https://doi.org/10.1039/c9tc05823k>
- [49] Jiles, D. C. (1990). *Introduction to Magnetism and Magnetic Materials* (1st ed). Springer.
- [50] MicroSense LLC. (n.d.). *VSM Options and Accessories*. MicroSense. Retrieved January 26, 2022, from <http://www.microsense.net/products-vsm-accessories.htm>
- [51] Dodrill, B.C., Lindemuth, J.R., & Krause, J.K. (2004). Magnetic Anisotropy: Measurements with a Vector Vibrating Sample Magnetometer.
- [52] Cullity, B. D., & Graham, C. D. (2008). Magnetic anisotropy. In *Introduction to Magnetic Materials* (2nd ed., pp. 197–238). Wiley-IEEE Press.
- [53] MicroSense LLC. (n.d.). *Torque Magnetometer*. MicroSense. Retrieved January 26, 2022, from <http://www.microsense.net/products-vsm-torque-magnetometer.htm>
- [54] MicroSense. *EasyVSM: Operating software for the microsense vibrating sample magnetometer*.

- [55] Coey, J. M. D. (2010). *Magnetism and magnetic materials* (1st ed.). Cambridge University Press.
- [56] QuantumDesign. *Vibrating sample magnetometer (VSM) option user's manual. Part number 1096-100. B0*.
- [57] Quantum Design North America. (2019, September 23). *VSM Option by Quantum Design* [Video]. YouTube. <https://www.qdusa.com/products/dynacool.html#productVideos>
- [58] Leng, Y. (2013). *Materials characterization: Introduction to microscopic and spectroscopic methods* (2nd ed.) [E-book]. Wiley-VCH.
- [59] RH-2000 – Hirox USA Inc. (n.d.). Hirox. Retrieved May 11, 2022, from <https://www.hiroxusa.com/products/3d-digital-microscope/rh-2000/>
- [60] Hirox-USA. (n.d.). *High-Range motorized triple zoom lens* [Photograph]. https://www.hiroxusa.com/products/3d-digital-microscope/lenses/hr-2500e_hr-5000e/
- [61] ProtoPlant, makers of Proto-pasta. (n.d.). *Magnetic Iron PLA*. Protopasta. Retrieved November 11, 2020, from <https://www.proto-pasta.com/products/magnetic-iron-pla>.
- [62] Nayle, S. V., Tate, J. S., & Slupsky, J. M. (2017, June 13–16). *Electrical and mechanical properties of metal filled conductive material using fused deposition modeling* [Conference Presentation]. POWDERMET 2017: International Conference on Powder Metallurgy & Particulate Materials, Las Vegas, Nevada, USA.
- [63] Hummel, R. E. (2011). *Electronic properties of materials* (4th ed. 2011, Corr. 3rd printing 2013 ed.). Springer.
- [64] Dieckow, K. J. (2021). *Automatic alignment methods for VSM using magnetic low anisotropic samples with reduced time and higher precision* (Master's).
- [65] Gandha, K., Li, L., Nlebedim, I., Post, B. K., Kunc, V., Sales, B. C., Bell, J., & Paranthaman, M. P. (2018). Additive manufacturing of anisotropic hybrid NdFeB-SmFeN nylon composite bonded magnets. *Journal of Magnetism and Magnetic Materials*, 467, 8–13. <https://doi.org/10.1016/j.jmmm.2018.07.021>
- [66] Song, H., Spencer, J., Jander, A., Nielsen, J., Stasiak, J., Kasperchik, V., & Dhagat, P. (2014). Inkjet printing of magnetic materials with aligned anisotropy. *Journal of Applied Physics*, 115(17). <https://doi.org/10.1063/1.4863168>
- [67] Geerts, W. J. (2020). *Magnetic materials and characterization forum (PHYS 5370)* [Illustration].
- [68] Chikazumi, S. (2009). *Physics of Ferromagnetism (International Series of Monographs on Physics, 94)* (2nd ed.). Oxford University Press.
- [69] Beleggia, M., de Graef, M., & Millev, Y. (2006). Demagnetization factors of the general ellipsoid: An alternative to the maxwell approach. *Philosophical Magazine*, 86(16), 2451–2466. <https://doi.org/10.1080/14786430600617161>

- [70] Omar, H. D. (2015). To investigation the structure and morphology of iron metallic by difference techniques. *Journal of Nanotechnology and Advanced Materials*, 3(2), 57–61. <https://doi.org/10.12785/jnam>
- [71] Gu, J., & Catchmark, J. M. (2013). Polylactic acid composites incorporating casein functionalized cellulose nanowhiskers. *Journal of Biological Engineering*, 7(1), 31. <https://doi.org/10.1186/1754-1611-7-31>
- [72] Sarangan, A. (2016). Nanofabrication. *Fundamentals and Applications of Nanophotonics*, 149–184. <https://doi.org/10.1016/b978-1-78242-464-2.00005-1>
- [73] Hojo, H., Fujita, K., Tanaka, K., & Hirao, K. (2004). Ferromagnetism in Fe-doped β -Ga₂O₃ prepared by a solid state reaction. *MRS Proceedings*, 853. <https://doi.org/10.1557/proc-853-i4.25>
- [74] QuantumDesign, Appl. Note 1500-010 Rev. A0, *Accuracy of the reported moment: axial and radial sample positioning error*.
- [75] QuantumDesign, Appl. Note 1500-020 Rev. B0, *Accuracy of reported sample moment: using the sample geometry simulator*.
- [76] QuantumDesign, VSM Appl. Note 1096-302, *Measuring temperature-dependent magnetization with the PPMS vibrating sample magnetometer (VSM)*.
- [77] Spaldin, N. A. (2010). *Magnetic materials: Fundamentals and applications* (2nd ed.). Cambridge University Press.
- [78] Ashcroft, N. W., & Mermin, D. N. (1976). *Solid state physics* (1st ed.). Cengage Learning.
- [79] Heider, F., Zitzelsberger, A., & Fabian, K. (1996). Magnetic susceptibility and remanent coercive force in grown magnetite crystals from 0.1 μ m to 6 mm. *Physics of the Earth and Planetary Interiors*, 93(3–4), 239–256. [https://doi.org/10.1016/0031-9201\(95\)03071-9](https://doi.org/10.1016/0031-9201(95)03071-9)
- [80] Zhang, X., Huang, H., Zhang, Y., Liu, D., Tong, N., Lin, J., Chen, L., Zhang, Z., & Wang, X. (2018). Phase transition of Two-Dimensional β -Ga₂O₃ nanosheets from ultrathin γ -Ga₂O₃ nanosheets and their photocatalytic hydrogen evolution activities. *ACS Omega*, 3(10), 14469–14476. <https://doi.org/10.1021/acsomega.8b01964>
- [81] Takano, Y., Hayashi, Y., Fukushima, J., & Takizawa, H. (2021). Room-temperature synthesis of γ -Ga₂O₃ nanoparticles from gallium metal via ultrasound irradiation. *Advanced Powder Technology*, 32(3), 860–865. <https://doi.org/10.1016/j.appt.2021.01.032>
- [82] Rock magnetism. (2000). *International Geophysics*, 31–77. [https://doi.org/10.1016/s0074-6142\(00\)80095-9](https://doi.org/10.1016/s0074-6142(00)80095-9)
- [83] Petrov, V. N., & Ustinov, A. B. (2010). Magnetic properties of Fe₃O₄ surface. *Journal of Surface Investigation. X-Ray, Synchrotron and Neutron Techniques*, 4(3), 395–400. <https://doi.org/10.1134/s1027451010030079>
- [84] Zhang, Z., & Satpathy, S. (1991). Electron states, magnetism, and the Verwey transition in magnetite. *Physical Review B*, 44(24), 13319–13331. <https://doi.org/10.1103/physrevb.44.13319>

- [85] Goss, C. (1988). Saturation magnetisation, coercivity and lattice parameter changes in the system Fe₃O₄-Fe₂O₃, and their relationship to structure. *Physics and Chemistry of Minerals*, 16(2). <https://doi.org/10.1007/bf00203200>
- [86] Hayashi, H., Huang, R., Ikeno, H., Oba, F., Yoshioka, S., Tanaka, I., & Sonoda, S. (2006). Room Temperature ferromagnetism in mn-doped γ -Ga₂O₃ with spinel structure. *Applied Physics Letters*, 89(18), 181903. <https://doi.org/10.1063/1.2369541>
- [87] Jamison, J. S., May, B. J., Deitz, J. I., Chien, S. C., McComb, D. W., Grassman, T. J., Windl, W., & Myers, R. C. (2019). Ferromagnetic epitaxial μ -Fe₂O₃ on β -Ga₂O₃: A new monoclinic form of fe₂o₃. *Crystal Growth & Design*, 19(8), 4205–4211. <https://doi.org/10.1021/acs.cgd.9b00029>
- [88] Cullity, B. D., & Graham, C. D. (2008a). Ferrimagnetism. In *Introduction to magnetic materials* (2nd ed., pp. 175–190). Wiley-IEEE Press.
- [89] Wu, C., Yu, Z., Sun, K., Nie, J., Guo, R., Liu, H., Jiang, X., & Lan, Z. (2016). Calculation of Exchange integrals and curie temperature for la-substituted barium hexaferrites. *Scientific Reports*, 6(1). <https://doi.org/10.1038/srep36200>